Portland State University
PDXScholar

Dissertations and Theses

Dissertations and Theses

Winter 1-5-2017

High-Quality Chemical Vapor Deposition Graphene-Based Spin Transport Channels

Lester Florian Lampert
Portland State University

Follow this and additional works at: https://pdxscholar.library.pdx.edu/open_access_etds

 Part of the Physics Commons
Let us know how access to this document benefits you.

Recommended Citation
Lampert, Lester Florian, "High-Quality Chemical Vapor Deposition Graphene-Based Spin Transport Channels" (2017). *Dissertations and Theses.* Paper 3327.
https://doi.org/10.15760/etd.3308

This Dissertation is brought to you for free and open access. It has been accepted for inclusion in Dissertations and Theses by an authorized administrator of PDXScholar. For more information, please contact pdxscholar@pdx.edu.

High-Quality Chemical Vapor Deposition Graphene-Based Spin Transport Channels

by

Lester Florian Lampert

A dissertation submitted in partial fulfillment of the
requirements for the degree of

Doctor of Philosophy
in
Applied Physics

Dissertation Committee:
Jun Jiao, Chair
Roman Caudillo
Erik Sánchez
Raj Solanki
Bin Jiang

Portland State University
2017

© 2016 Lester Florian Lampert

Abstract

Spintronics reaches beyond typical charge-based information storage technologies by utilizing an addressable degree of freedom for electron manipulation, the electron spin polarization. With mounting experimental data and improved theoretical understanding of spin manipulation, spintronics has become a potential alternative to charge-based technologies. However, for a long time, spintronics was not thought to be feasible without the ability to electrostatically control spin conductance at room temperature. Only recently, graphene, a 2D honeycomb crystalline allotrope of carbon only one atom thick, was identified because of its predicted, long spin coherence length and experimentally realized electrostatic gate tunability. However, there exist several challenges with graphene spintronics implementation including weak spin-orbit coupling that provides excellent spin transfer yet prevents charge to spin current conversion, and a conductivity mismatch due to the large difference in carrier density between graphene and a ferromagnet (FM) that must be mitigated by use of a tunnel barrier contact. Additionally, the usage of graphene produced via chemical vapor deposition (CVD) methods amenable to semiconductor industry in conjunction with graphene spin valve fabrication must be explored in order to promote implementation of graphene-based spintronics. Despite advances in the area of graphene-based spintronics, there is a lack of understanding regarding the coupling of industry-amenable techniques for both graphene synthesis and lateral spin valve fabrication. In order to make any impact on the application of graphene spintronics in industry, it is critical to demonstrate wafer-scale

graphene spin devices enabled by wafer-scale graphene synthesis, which utilizes thin film, wafer-supported CVD growth methods.

In this work, high-quality graphene was synthesized using a vertical cold-wall furnace and catalyst confinement on both SiO_2/Si and C-plane sapphire wafers and the implementation of the as-grown graphene for fabrication of graphene-based non-local spin valves was examined. Optimized CVD graphene was demonstrated to have $I_{D/G} \approx 0.04$ and $I_{2D/G} \approx 2.3$ across a 2" diameter graphene film with excellent continuity and uniformity. Since high-quality, large-area, and continuous CVD graphene was grown, it enabled the fabrication of large device arrays with 40 individually addressable non-local spin valves exhibiting 83% yield. Using these arrays, the effects of channel width and length, ferromagnetic-tunnel barrier width, tunnel barrier thickness, and level of oxidation for Ti-based tunnel barrier contacts were elucidated. Non-local, in-plane magnetic sweeps resulted in high signal-to-noise ratios with measured ΔR_{NL} across the as-fabricated arrays as high as 12 Ω with channel lengths up to 2 μm. In addition to in-plane magnetic field spin signal values, vertical magnetic field precession Hanle effect measurements were conducted. From this, spin transport properties were extracted including: spin polarization efficiency, coherence lifetime, and coherence distance.

The evaluation of industry-amenable production methods of both high-quality graphene and lateral graphene non-local spin valves are the first steps toward promoting the feasibility of graphene as a lateral spin transport interconnect material in future spintronics applications. By addressing issues using a holistic approach, from graphene

synthesis to spin transport implementation, it is possible to begin assessment of the challenges involved for graphene spintronics.

Acknowledgements

This work was largely produced due to opportunities provided by Prof. Jun Jiao through the forum of her laboratory. Therefore, I would like to thank Prof. Jiao for the advice and opportunities given, which allowed me to grow intellectually and enhanced my leadership skills. The number of opportunities offered to students by Prof. Jiao is unmatched in my experience within academia. Since my time within the Jiao group, I was able to lead many projects, mentor talented students, and develop three new research and development laboratories within a very collaborative environment. I would also like to thank many of the students I had to privilege to mentor for both enhancing my projects and providing inspiration for others.

I would also like to deeply thank Dr. Roman Caudillo. Dr. Caudillo advised from the Intel side of my thesis project and provided several years of deep insight, mentorship, technical expertise, and career and life guidance. His expertise has proven invaluable and ranges greatly from 2D materials to nearly all aspects of semiconductor technology and beyond. It was a privilege to work with Dr. Caudillo the past few years. *Estoy agradecido*!

To my thesis committee as a whole, I would like to thank each one of you for serving on my committee and helping me develop both academically and professionally. Thank you to Prof. Erik Sanchéz for assistance with navigating the PhD process and your willingness to provide advice (and equipment!) whenever asked. Prof. Sanchéz has a gift for developing scientific instrumentation that served as a constant inspiration for hands-

on experiences and frequently prompted me to go into the “deep end” of a project build. Thank you to Prof. Raj Solanki for providing insights with graphene and other 2D materials in addition to teaching a fantastic microfabrication course series at Portland State University. Thank you to Prof. Bin Jiang for your past collaborations of modeling and band structure calculations for graphene including your intense enthusiasm and positivity.

I would like to acknowledge the staff of the Center for Electron Microscopy and Nanofabrication (CEMN) where I spent a large portion of my time with both analysis and fabrication work.

Thanks to the staff of the Physics Department and the Maseeh College of Engineering and Computer Science for your support. During the laboratory move from Physics to Engineering, the staff at Engineering were very welcoming and helpful when establishing the new facilities and administrative processes.

This thesis is dedicated to Yongwen, my wonderfully supportive wife and physics PhD, and Chloe, my beautiful daughter. Yongwen has stood by my side throughout all of the ups and downs that accompany the PhD process, and life, in general. Her patience and love inspired me to continue pursuing research questions and her discipline and rigor kept me down-to-earth and pragmatic so I did not lose sight of my goals. I am a more complete person as a result and am forever grateful. 我非常爱你！

Lester Florian Lampert

Portland State University, 2016

Table of Contents

List of Figures

1. Introduction

Graphene is largely responsible for ushering in a new class of materials, the two-dimensional (2D) atomic crystal system. Along with its ideal 2D organization, graphene holds many superlatives such as: a large Young's modulus – stiffer than diamond[1], ~10^6 times the current density of Cu[2], 100 times the intrinsic mobility of Si[3], and the longest mean free path of electrons at room temperature (RT). Moreover, graphene is thin, only a single atom thick, and allows the surface interactions it has with its surroundings to dictate electronic behavior known as proximity effects[4,5,6,7]. These and other characteristics have made graphene a primary focus for many researchers within academia and industry.

Directly related to spintronics, graphene is ideal since sp^2 bonded carbon atoms have weak spin-orbit coupling (SOC)[8], theoretically allowing injected spin to traverse a graphene sheet practically undisturbed[9,10]. The arrangement of carbon atoms in the graphene lattice has high symmetry and long-range order. This, in conjunction with the relative lightness of carbon and the primary carbon isotope found in graphene, ^{12}C (equal number of protons and neutrons), allows for low-resistance conductance of injected electron spin current[11]. However, the weak SOC of graphene presents some disadvantages such as graphene may conduct electron spin current well yet it is not an intrinsic property for direct charge to spin current production. Thus substantial effort has been made in the field of graphene spintronics to improve the SOC of graphene-based devices by use of other 2D materials, namely transition metal dichalcogenides (TMDCs),

which have excellent, relative SOC[12,13,14]. Graphene takes advantage of the strong SOC associated with TMDCs through an established proximity effect whereby graphene, a single atom thick sheet, has behavior dictated by the material graphene has direct contact. Other efforts include functionalization of graphene using adatoms and admolecules and offer spatial tailoring of graphene devices using selective functionalization achieved with lithographic methods[15].

RT spin transport in graphene was first established in 2007, where an applied magnetic field along the long axis of the ferromagnetic electrodes used for polarized spin injection and spin current detection using a typical non-local spin valve (NLSV) geometry as depicted in Figure 1.1[16].

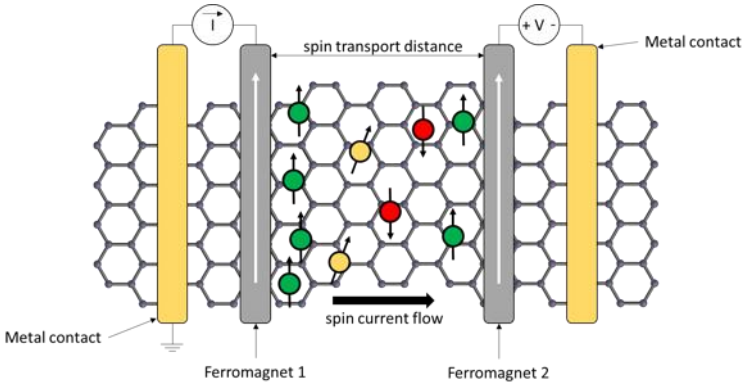

Figure 1.1. The typical non-local spin valve for testing spin injection and transport with graphene channels. Polarized spin is injected at FM 1 and then recombines to the left-most metal contact while pure spin current diffuses across the channel between FM 1 and 2. The diffused spin current is detected at FM 2. Out-of-plane magnetic fields are applied and swept for Hanle precession measurements and in-plane magnetic fields are applied and swept for ΔR_{NL} measurements.

The NLSV geometry is an experimental vehicle for investigation of polarized charge current and pure spin current since both are produced and detected using this device

layout. There are two main regions of an NLSV: the local and non-local sides. On the local side, current is injected through FM1, as depicted in Figure 1.1, and emerges as polarized current, which recombines at the local region metal contact and pure spin current that diffuses across the channel towards FM2 on the non-local side. The spin current accumulating under FM1 is majority spin current and therefore the minority spin current is simultaneously depleted at FM1. The resulting spin currents, majority and minority, traverse the channel in opposite directions obeying a diffusion relation and are called pure spin currents. This initial result achieved 10% spin injection efficiency. It was not until 2010 that a high spin injection efficiency was achieved of 30% by utilizing tunneling barriers of TiO_2/MgO[17]. This was the first time conductance mismatch between graphene and the ferromagnetic contacts was experimentally verified resulting in a large non-local signal (130 Ω). From this study, there was a major shift in the approach of graphene-based non-local spintronic devices. Subsequent studies focused on developing idealized interfaces between graphene and the spin injector and detector[18–21]. There are three major classes of graphene/injector-detector contacts: 1) transparent, 2) pinhole, and 3) tunneling[17]. Transparent contacts are where the FM is in direct contact with graphene and results in the greatest conductance mismatch, lending itself to the greatest potential for spin backflow since the graphene channel carrier density is much lower than the FM. Pinhole contacts refer to the physical nature of the contact where an insulating layer is deposited onto graphene and demonstrates poor adhesion resulting in physical pinholes, which allow for periodic direct contact between graphene and the FM. Tunneling contacts are the final, natural progression of the graphene/injector-detector interface

where an insulating layer is deposited between graphene and the FM with good adhesion and no pinholes. The resulting interface has a resistance larger than the graphene channel resistance, which prevents backflow of spin and this tunneling barrier (TB) has been deposited via atomic layer deposition (ALD)[22], transfer of h-BN[23,24], TiO_2-seeded MgO[17], and fluorinated graphene[25,26].

Upon the enrichment in knowledge of graphene-FM contacts, the next, logical path forward is to test the limitations of tunneling contacts as they proved to produce large non-local ΔR_{NL}. Yamaguchi et al. established spin injection into pristine, exfoliated graphene supported by exfoliated h-BN using exfoliated h-BN TBs and Py FMs with a spin relaxation time of 56 ps and spin diffusion length of 1.14 μm at RT[23]. Then, in 2014 Kamalakar et al. demonstrated improved spin injection using CVD h-BN TBs on pristine, exfoliated graphene with spin lifetimes of 0.46 ns[27]. Shortly after, Kamalakar et al. reported detectable spin transport lengths up to 16 μm with a spin lifetime of 1.2 ns and spin diffusion length of 6 μm[28]. This study established that with TBs of TiO_2 connected to Co FMs and CVD graphene, long spin transport can be achieved. Other work by Ingla-Aynés et al. was able to extend the transport of spin currents by using drift current to extend the relaxation distance to 90 μm[125]. Comparing these studies, there is obvious discrepancy in the resulting spin relaxation times and spin diffusion lengths if CVD graphene with an oxide TB is outperforming pristine, exfoliated graphene supported by exfoliated or CVD h-BN, predicted to have superior spin injection properties. A systematic approach to understanding the difference between pristine, exfoliated graphene and CVD graphene is required. Additionally, a materials study of the

interaction between the FM and tunneling barrier could lead to additional insight regarding the conductance mismatch between graphene and the injector-detector contacts. Lastly, the effect of residues between the graphene and injector-detector contacts could lead to development of improved graphene transfer protocols utilized for spintronic studies.

In this thesis, the following issues have been investigated relating to both graphene growth and implementation as a spin transport channel:

1. Efficient graphene growth using Cu thin films with SiO_2/Si wafers.
2. High-quality graphene growth with Cu thin films templated by C-plane sapphire wafers and associated electrochemical transfer for wafer-scale graphene sheets.
3. Implementation of wafer-scale graphene sheets for lateral spin valves with transition metal oxide tunnel barrier contacts.

1.1. Literature Survey

The following two sections provide a research literature survey for both graphene growth and long-distance spin transport using graphene. Since graphene growth using SiO_2/Si and C-plane sapphire wafers has substantial overlap, there will be only one review section for graphene growth in general and related to Cu thin films. Following this section is a review of graphene spin transport channels with long channel length and associated works.

1.1.1. Graphene Growth on Cu Thin Film Catalysts Supported by SiO_2/Si and C-Plane Sapphire Wafers

Graphene has attracted considerable attention since its first experimental isolation owing to its exceptional properties[29–33]. Initial isolation was achieved with mechanical exfoliation of natural graphite crystals but the method was not suitable for mass production[34]. Although various fabrication methods have been investigated, chemical vapor deposition (CVD) is recognized as an effective technique to achieve the goal of high-quality, large-area graphene sheets suitable for electronic device fabrication. For CVD growth of graphene, the catalyst is one of the most critical parameters. First attempts were made with nickel (Ni) and iron (Fe) catalyst materials resulting in in-homogeneous films dense in bilayer regions when attempting to tune towards monolayer graphene using carbon segregation[35]. Later, rapid thermal annealing (RTA) was introduced to produce monolayer graphene[36]. Copper (Cu) catalysts were first introduced by Li and co-workers[37] and were demonstrated to exhibit a self-limited growth characteristic, which was attributed to the relatively low carbon solubility in Cu as compared to Ni and Fe. Recent advancements in CVD graphene using Cu catalyst have greatly re-fined this process and even identified the parameters required to grow multi-layer graphene resulting from variations in the Cu surface morphology[38]. Other critical parameters were investigated such as hydrogen (H_2) concentration relative to carbon precursor and gas versus liquid phase precursors[39–41]. The vast majority of high-quality graphene to-date has been grown using Cu foils as both catalyst and substrate. Various supply chains provide Cu foils for this fabrication technique, which has resulted in a

handful of successful companies offering graphene to both industrial and academic customers.

Although CVD of Cu foil based graphene has come a long way and become ubiquitous in academic research, it is still not a viable process for the semiconductor industry. There remain many challenges for its consideration; for complementary metal-oxide-semiconductor (CMOS) backend applications, the most critical requirement is the need for a low-temperature direct deposition process, preferably on a dielectric, for an appropriate-quality graphene for the given, specific application. For a frontend application, or planar geometry application, a growth and mechanical transfer process may be feasible although many improvements are still needed for both the growth and transfer steps. For integration, growth temperature is generally not an issue. Reliability and repeatability of the transfer process and the challenges associated with the lack of rigidity of metal foils and variability of the Cu foils from different suppliers (related to quality, cleanliness, and morphology) are of critical importance. Using thin film Cu as the catalyst supported by a wafer presents a solution to many of these problems. For example, consider the following four benefits: 1) the Cu catalyst is supported by a rigid wafer substrate that prevents mechanical deformation of the graphene/Cu film, 2) Cu thin films can be deposited by several low-cost physical vapor deposition (PVD) methods such as sputtering, thermal evaporation, electron beam evaporation, and electroplating, 3) purity of the Cu thin film can be easily controlled by aforementioned PVD processes, and 4) wafer-based synthesis of graphene is most compatible with current semiconductor industry fabrication processes.

Despite the advantages offered by utilizing a Cu thin film catalyst on rigid substrates, other challenges have pre-vented widespread adoption from this technique as it has a larger sensitivity to process parameter variations due to the crystalline uniformity of Cu thin films ~1 μm or thinner compared to thick Cu foils ~25 μm thick. Additionally, Cu has an intrinsically poor adhesion to SiO_2, the most commonly employed catalyst support for Cu thin films, which results in pinholes, voids, and sometimes complete delamination of the Cu thin film from the SiO_2 wafer during a growth process. To prevent pinhole and void formation, one could increase thickness of the Cu layer, however, the growth temperature must be increased in compensation[42].

To improve mechanical stability, some have introduced caps to place over the growth substrate[43] where they used folded pockets of Cu foils to improve graphene growth characteristics and achieved graphene crystal do-mains up to 0.5 mm on a wafer substrate using a tube furnace CVD system. Following this development there has been effort to recreate the Cu foil pocket growth with other CVD reactor configurations such as a vertical cold-wall furnace resulting in reduced process time[44]. Although these improvements afforded by analogous pocket growth have resulted in better graphene with large single crystal domains, they still present issues with scalability, graphene handling and transfer, as well as the lacking of control for Cu source materials when using Cu foils as a graphene catalyst.

A large amount of experimental results comparing growth of graphene on various Cu crystalline orientations has indicated that Cu (111) results in the highest-quality graphene demonstrated by the reduced Raman D:G intensity ratio ($I_{D/G}$)[45–48]. Scanning

tunneling microscope (STM) studies comparing graphene grown on Cu (100) versus Cu (111) reveal that a uniform sheet of graphene is grown on Cu (111) surfaces with quality dictated by grain boundaries whereas graphene grown on Cu (100) results in incomplete graphene growth with nanoscale edges and enhanced $I_{D/G}$[49]. To further pursue the formation of large-scale Cu thin film with a Cu (111) orientation, many of the aforementioned studies have utilized C-plane sapphire to form epitaxial Cu films while specific Cu thickness and process conditions could result in a predominantly Cu (111) orientation of a recrystallized Cu on SiO_2/Si. Although these studies advanced the understanding of graphene growth on crystalline Cu thin film supports, the study for how to precisely control the Cu catalyst morphology in relation to the optimization of other growth parameters in a confined growth environment towards achieving high-quality and wafer-scale graphene is missing.

1.1.2. Graphene Spin Transport

Graphene has ushered in a new era for spintronics research owing to its weak SOC and negligible hyperfine interaction[11]. Initially, graphene spin transport was demonstrated with mechanically exfoliated graphene[16], but was limited due to small graphene flakes as a result of the exfoliation process. The next logical route for longer transport channels was pursued utilizing CVD graphene, which has been demonstrated using a myriad of reactor geometries, thermal and plasma processes, and metal catalyst systems as reviewed in the previous section. CVD graphene can be synthesized over very large areas with various metal foil catalyst techniques, however, foil graphene is less likely to be implemented in the semiconductor industry due to issues with handling and

purity control. Therefore, it is important to also develop graphene spintronics using CVD graphene derived from more semiconductor industry-amenable techniques such as using metal, thin films supported by rigid wafers. To-date, the majority of graphene spin valves have been tested with CVD graphene derived from Cu foil with excellent results yielding long spin transport up to 16 μm with spin lifetimes of 1.2 ns on SiO_2[28]. A suggested approach to enhance the spin lifetime is to improve the graphene mobility, although many studies demonstrate a weak dependence of ΔR_{NL} on carrier mobility[50,51]. CVD of polycrystalline graphene is relatively mature in academia with an average carrier mobility ~3,000 $cm^2/V.s$ and single crystal CVD graphene is a current topic for research although it has yet to be observed experimentally across an entire wafer[52–55]. Due to this limitation, others have attempted to screen charge-based scattering induced by the SiO_2 surface and encapsulated the graphene spin transport channel using hexagonal boron nitride (h-BN)[56]. Although this work resulted in a spin lifetime enhancement that is critical for driving future developments, it is not currently feasible for implementation in semiconductor industry due to the poor quality of commercially available CVD h-BN films[57,58].

Beyond injection of spin polarized current into graphene using a ferromagnet and tunnel barrier, new methods have been developed that enhance the SOC of graphene by introduction of adatoms and admolecules *via* functionalization routes using hydrogen[59,60], fluorine[15,61], and organic molecules[62,63] and by adatoms with outer-shell *p* orbitals[64]. Other routes for enhancement of SOC include intercalation of graphene on iridium substrates with islands of lead[30], and proximity coupling of graphene to Cu (111) surfaces[65] and topological insulators[66].

Besides implementation of industry amenable methods for combined graphene growth and spin transport, there has been some effort to promote wafer-scale graphene spin transport fabrication methods[20,67]. Due to the challenges facing the graphene spintronics field, the vast majority of studies, to-date, have been fundamental. Largely responsible for this is the lack of understanding available for spin scattering mechanisms in graphene. There have been three scattering mechanisms proposed: 1) Elliott-Yafet[68], 2) D'yakonov Perel'[69], and, more recently, 3) resonant scattering[70].

1.1.3. Spin Scattering Mechanisms

Elliott-Yafet Scattering

In the presence of SO interaction, Bloch states are not spin eigenstates within a real, crystalline material[71] and are instead, a mixture of two orthogonal spin states dependent upon the electron's momentum[72]. This means the spin flip probability depends on momentum relaxing collisions, or, in other words, the Elliot-Yafet (EY) scattering mechanism arises from crystal defects. These defects consequently cause the electron to interact with the electric field of the atomic nuclei present within the crystal. For this reason, EY scattering is results in a spin flip length that is linearly proportional to the mean free path of a conducting electron and can be expressed as,

$$\lambda_{sf} = \sqrt{D\tau_{sf}}\,, \tag{1.1}$$

where λ_{sf} is the spin flip length, D the diffusion constant, and τ_{sf} the spin flip time. We can define $1/\tau_{sf}$ as[73],

$$\frac{1}{\tau_{sf}} \approx \frac{b^2}{\tau_p}, \tag{1.2}$$

where τ_p is the momentum scattering time, and b the intrinsic SO coupling divided by the Fermi energy. For graphene, the EY spin scattering mechanism is thought to be dominant with defective graphene.

D'yakanov Perel' Scattering

Unlike the EY scattering mechanism, which is inversely proportional to electron mobility, the D'yakanov Perel' (DP) scattering mechanism is directly proportional to electron mobility and hence the electron velocity and is based upon motional narrowing, where spin relaxation reduces as the number of electron scattering events increases[74]. Crystals lacking inversion symmetry have a finite electric field that lifts spin degeneracy. DP scattering therefore occurs due to a momentum-dependent pseudo-magnetic field, which spin electrons shall precess around. This precession effect occurs with the lack of spatial inversion symmetry as a non-linear process. For DP scattering, we can define $1/\tau_{sf}$ as,

$$\frac{1}{\tau_{sf}} \approx \lambda_R^2 \tau_p, \tag{1.3}$$

where λ_R is the Rashba field magnitude. Equation 1.3 makes it apparent that DP scattering relaxation rate is inversely proportional to momentum scattering rate, opposite to the EY scattering mechanism. Therefore, one can make the prediction the DP scattering mechanism will be dominant in graphene with high mobility due to the

proportionality of the pseudo-magnetic field strength on electron velocity. This holds true for electrons driven with sufficiently low electric field[75].

Resonant Scattering

Unlike EY and DP scattering mechanisms, which are derived from semiconductor spintronics[76], resonant scattering was recently introduced as a possible mechanism for spin relaxation in graphene[70]. This concept was introduced to explain the small spin relaxation experimentally observed in graphene and incorrectly predicted by both the EY and DP mechanisms. The proposed, dominant cause of the resonant process is the existence of local magnetic moments that serve as spin hot spots at resonant conditions. This mechanism was modeled to dominate graphene spin relaxation rates with 1 ppm of local magnetic moments, a reasonable value based upon experimental results. The spin relaxation rate for resonant scattering can be defined as,

$$\frac{1}{\tau_{sf}} \approx n\frac{2\pi}{\hbar}v_0(E)f_{\sigma,\bar{\sigma}}\left[\frac{\alpha_l(E)}{1-\alpha_l G_0(E)}, \frac{\alpha_0(E)}{1-\alpha_0 G_0(E)}\right], \tag{1.4}$$

where $n = {N_H}/{N_C}$ is the concentration of magnetic moments, α_l the energy-dependent on-site coupling, G_o the graphene Green function, and v_0 the DOS per atom and spin. Using 1 ppm of magnetic impurities, a spin relaxation time of 100 ps was calculated by Kochan et al.[70]. This value corresponds well to the work in this thesis, where spin relaxation times of 135 ps were measured and suggests the relative magnetic moment concentration may be lower than 1 ppm for the graphene grown for this thesis. The resonant scattering mechanism is therefore the best attempt for prediction of spin

relaxation times in comparison to the EY and DP mechanisms, which both predict $\tau_{sf} \approx 1\,\mu s$ that has yet to be demonstrated experimentally. Although DP and EY scattering mechanisms have been introduced, they do not come close to predicting the experimentally observed behavior in both this and other works. Only EY- or DP-like behavior can be observed with spin lifetimes an order of magnitude different between theory and reality. Therefore, spin scattering mechanisms are most likely a combination of EY, DP, and resonant processes.

1.2. Problem Statement

During the past decade, tremendous progress has been made in the field of graphene spintronics elucidating the advantages of room-temperature spin transfer characteristics including spin signal intensity, lifetime, and diffusion length. Graphene spintronics was named as one of the fundamental topics of the Graphene Flagship[77] consortium in Europe and has become a central area of focus for several spintronics centers around the world. As one of the most promising candidates for enabling lateral spintronics, graphene has been established as one of the key, potential materials to unlock long-awaited spintronics platform technologies.

Currently, magnetic memory storage dominates the digital market place and as the push towards big data and cloud storage continues to increase, the demand for "greener" (i.e. more energy efficient and sustainable) and higher density information storage and processing will increase dramatically[78–80]. The goal of spintronics is to produce non-volatile memory and processing electronics to address these growing issues and graphene

may be one of the key materials for next-generation spintronics. Several challenges exist to realize the potential of graphene spintronics and it all begins with sourcing graphene for manufacturing processes. To-date, single crystal, wafer-scale graphene has yet to be realized and current, state-of-art wafer-scale graphene growth is polycrystalline where its strength is determined by the weakest link in the crystal[81]. Therefore, transporting, much less growing high-quality, wafer-scale graphene, without cracks and associated defects still remains a challenge. Seeking the application of graphene to the field of spintronics adds several layers of complexity where manufacturing of graphene spin devices assumes the growth and transfer challenges have been mostly solved. The primary goals of this dissertation are to first address some graphene growth and transfer challenges using wafer-scale methods and then implementing the transferred, as-grown graphene for large array fabrication of graphene spin valves. This work seeks to gain insight for key challenges preventing graphene from both manufacturing contexts and to measure spin transport properties of aforementioned spin valve arrays. As for the future of graphene spintronics, one can only wait and see what the next decade of research and development efforts shall bring.

1.3. Ferromagnetism

In order to develop an understanding of spintronics fundamentals, is necessary for the reader to understand ferromagnetism, spin transport models, and measurement techniques used for extraction of key spin transport parameters. These topics shall be addressed in the following sections in a comprehensive manner from the origins of ferromagnetism to the logical design of lateral spintronics.

The majority of materials with unpaired electrons exhibit magnetic properties. For ferromagnetic materials composed of transition metals, this property is a consequence of unfilled 3d electron orbitals, which rearrange according both the Pauli principle and Hund's rules. The 3d electrons will rearrange to form the lowest energy configuration between two different arrangements called the parallel and anti-parallel states. Parallel and anti-parallel states represent a triplet and singlet electron orbital configuration, respectively. The difference in energy between the parallel and anti-parallel state is called the exchange energy and materials with exchange energies much larger than competing dipole-dipole interactions are classified as magnetic. FM classification can be further refined by comparing the ratio of energy required for parallel state spin alignment in comparison to the change in kinetic energy, which results in a magnetized state at thermal equilibrium. The magnetized state can be described as the spin polarization stemming from a splitting in the density of states at the Fermi level and takes the form

$$P = \frac{N_{\uparrow} - N_{\downarrow}}{N_{\uparrow} + N_{\downarrow}}. \tag{1.5}$$

Spin polarization can then be utilized technologically through use of spin current. Electron spins, regardless of measurement direction, can be described as

$$s_z = \pm\frac{1}{2} \; and \; \hbar s_z \, . \tag{1.6}$$

When electrons with these states flow through a ferromagnetic material the spin up $\left(s_z = +\frac{1}{2}\right)$ electrons encounter less resistance than the spin down electrons resulting in a net spin current. The conductivity, σ, of the FM is defined as a sum of the spin up and

spin down conductivity ($\sigma = \sigma_{\uparrow} + \sigma_{\downarrow}$) within the two current model. The spin polarization current of the FM can then be defined as

$$P_{FM} = \frac{\sigma_{\uparrow} - \sigma_{\downarrow}}{\sigma_{\uparrow} + \sigma_{\downarrow}}. \tag{1.7}$$

The spin dependent conductivities are expressed by the Einstein equation

$$\sigma_{\uparrow\downarrow} = N_{\uparrow\downarrow} e^2 D_{\uparrow\downarrow}, where\ D_{\uparrow\downarrow} = \frac{1}{3} v_{F\uparrow\downarrow} L_{e\uparrow\downarrow}\,, \tag{1.8}$$

where $D_{\uparrow\downarrow}$ is the spin diffusion constant, e the electron charge, $v_{F\uparrow\downarrow}$ the spin Fermi velocity, and $L_{e\uparrow\downarrow}$ the mean free path of the spin electron.

1.4. Spin Injection and Transport

At minimum, spin-based devices generally comprise of a spin injector, transport channel, and detector. The injector and detector are both comprised of ferromagnetic materials whereas the spin transport channel is generally a non-magnetic material with a long spin coherence length. In order to better understand how the spin injection and transport are related, a resistor model that applies to both the injection and detection ferromagnetic electrodes is introduced based on the groundwork laid out in the previous section.

1.4.1. Spin Transport Two Channel Resistor Model

Both the FM injector and detector can be represented by two resistors in parallel with one resistor representing the spin up resistance, $R_{\uparrow}$, and the other the spin down resistance, $R_{\downarrow}$. This is depicted schematically in Figure 1.3.

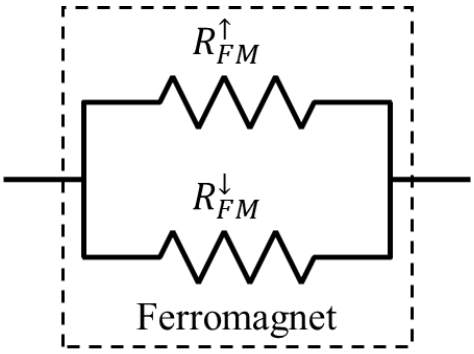

Figure 1.2. Two channel resistor model for a FM electrode. a) The ferromagnetic spin injector and detector may be represented schematically by two resistors in parallel where the spin up and spin down resistance are separate resistors and during polarization of the FM, $R_{FM}^{\downarrow} > R_{FM}^{\uparrow}$.

The total FM current resistance, R_{FM}, is calculated by simple analysis of two resistors in parallel to get

$$R_{FM} = \frac{R_{FM}^{\uparrow} R_{FM}^{\downarrow}}{R_{FM}^{\uparrow} + R_{FM}^{\downarrow}}. \tag{1.9}$$

Recalling the spin current polarization, P_{FM}, defined in the previous section, one can now write the FM resistances in terms of P_{FM} and the ferromagnetic spin majority/minority resistance term, $R_{FM}^{\uparrow\downarrow}$. This takes the form

$$R_{FM}^{\uparrow} = \frac{2R_{FM}}{1 + P_{FM}} \; and \; R_{FM}^{\downarrow} = \frac{2R_{FM}}{1 - P_{FM}}, \tag{1.10}$$

and for each ferromagnetic material P_{FM} has been typically accepted as a constant value with Co having a spin polarization of 42%. However, there has been recent work, which

has demonstrated there exists a temperature dependence on spin polarization[82]. In this work a spin-wave Doppler technique was used to measure the temperature dependence of magnetization drift velocity and the current polarization in $Ni_{80}Fe_{20}$ (similar to permalloy). It was found the spin polarization dropped nearly 23% from 80 to 340 K.

$$\frac{1}{R_{FM}^{\uparrow}} = \frac{1}{R_{FM}^{\downarrow}} \frac{1 + P_{FM}}{1 - P_{FM}}, \tag{1.11}$$

Now, if $\frac{1}{R_{FM}^{\uparrow\downarrow}}$ is substituted for $\sigma_{\uparrow\downarrow}$ in Equation 1.3, one can arrive at

which allows us to express the majority spin resistance in the FM in terms of the minority spin resistance and spin polarization.

Relationships are now derived for the FM, it is necessary to add the other components of basic spin device such as the transport channel and the ferromagnetic detector, which is assumed to be identical to the injector for the purposes of this discussion. Let's now complete the resistor model to include both the transport channel and the detector FM as depicted in Figure 1.4.

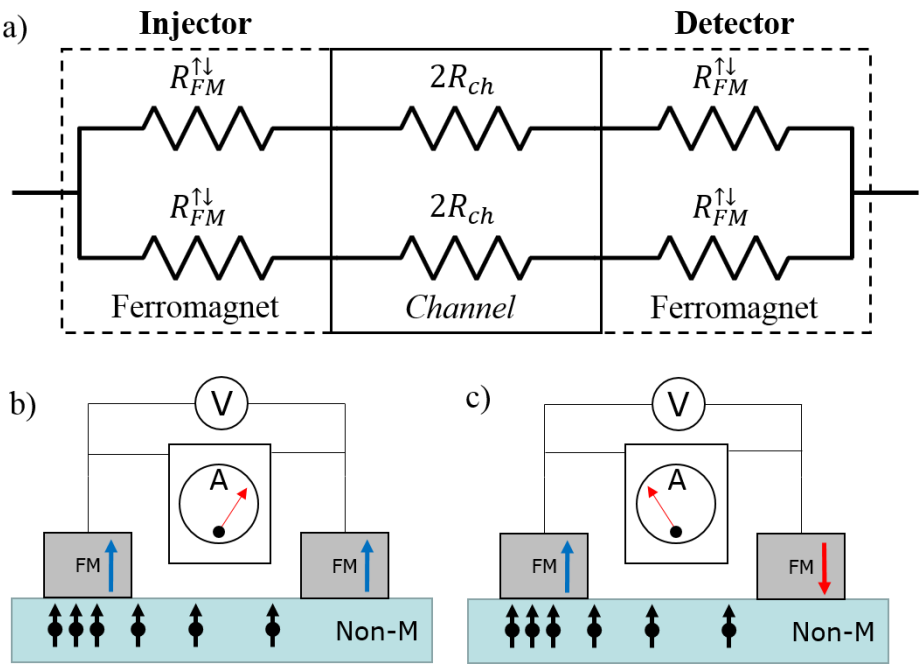

Figure 1.3. Two channel resistor model applied to a basic spin valve. a) A resistor schematic representation of basic building blocks for spin injection and detection. The injector and detector FMs are assumed identical for this treatment. b) When the injector and detector are in the parallel arrangement, both FMs have aligned magnetic domains and the largest current may flow through the channel. And when the FMs are anti-parallel the lowest current may flow.

The transport channel resistance is R_{ch} and each spin current channel will experience $2R_{ch}$ as shown by the schematic in Figure 1.4a. During parallel operation of the circuit, both ferromagnetic electrodes are polarized in the same direction and the maximum current will flow as depicted in Figure 1.4b. The opposite occurs in the anti-parallel state when the ferromagnetic electrodes have opposite polarization as illustrated in Figure 1.4c. Regarding the schematic view in Figure 1.4a, the parallel and anti-parallel states can be represented the same way using blue resistors for low resistance and orange resistors for high resistance as seen below in Figure 1.5.

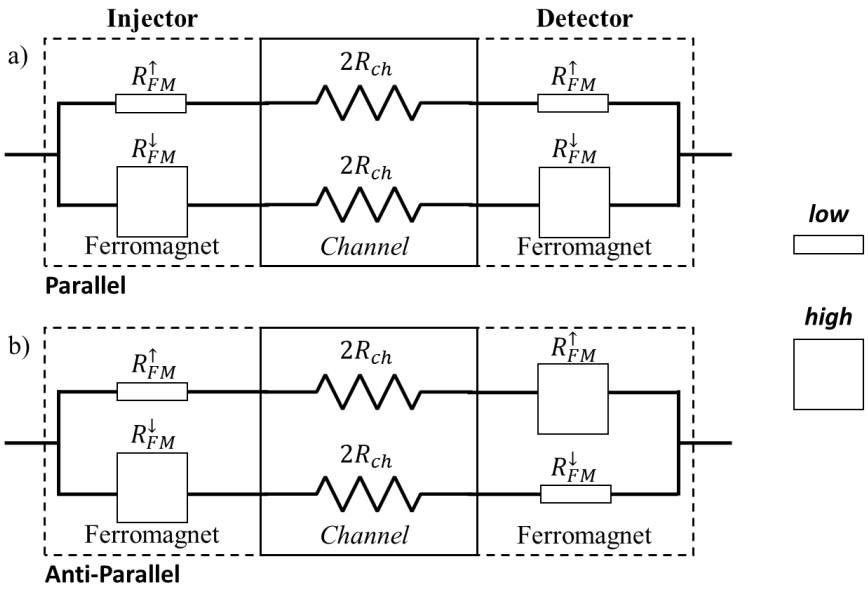

Figure 1.4. Schematic of two channel model for spin valve in parallel and anti-parallel mode. a) The parallel state is when the majority spin channel has low resistance and the minority spin channel has high resistance. b) The anti-parallel state occurs after the ferromagnetic electrodes have opposite polarization and both the majority and minority spin channel will have a high resistance. When this state occurs, the minimum current flows through the transport channel.

The spin polarization current in the channel for the parallel state, which looks very similar to Equation 1.3 and is defined as

$$P_{ch} = \frac{j_{\uparrow} - j_{\downarrow}}{j_{\uparrow} + j_{\downarrow}}, \tag{1.12}$$

where $j_{\uparrow}$ and $j_{\downarrow}$ are the majority and minority spin current, respectively. Therefore, upon inspection of the resistor network in Figure 1.5a, for the parallel state, one can develop the relationship for both the majority and minority spin current channels that take the form

$$j_{\uparrow} = \frac{V_{\uparrow}}{2(R_{FM}^{\uparrow} + R_{ch})} \; and \; j_{\downarrow} = \frac{V_{\downarrow}}{2(R_{FM}^{\downarrow} + R_{ch})}, \tag{1.13}$$

where $V_{\uparrow} = V_{\downarrow}$ because the two spin current channels are in parallel. Then one can substitute the relationships in Equation 1.9 into Equation 1.8 and arrive at

$$P_{ch} = \frac{2P_{FM}R_{FM}}{2R_{FM} + R_{ch}(1 - P_{FM}^2)}. \tag{1.14}$$

To better understand the relationship between P_{ch} and P_{FM}, P_{FM} is factored out to arrive at the final expression of

$$P_{ch} = P_{FM}\left(\frac{R_{FM}}{R_{ch}}\right)\left(\frac{2}{2\left(\frac{R_{FM}}{R_{ch}}\right) + (1 - P_{FM}^2)}\right). \tag{1.15}$$

This expression lends impressive insight into the basic operation of spin transport for our basic model with the most obvious consequence that P_{ch} and P_{FM} are directly proportional. Therefore, with increasing FM spin polarization, the spin transport channel polarization is expected to increase. However, there exists another issue that arises due to the dependence of P_{ch} on the ratio of the ferromagnetic electrode and the spin transport channel, $\left(\frac{R_{FM}}{R_{ch}}\right)$. Generally, we expect $R_{FM} \ll R_{ch}$, which results in a large reduction for

the spin transport channel polarization. The relationship between P_{ch} and P_{FM} is plotted in Figure 1.6 with three different values for $\left(\frac{R_{FM}}{R_{ch}}\right)$.

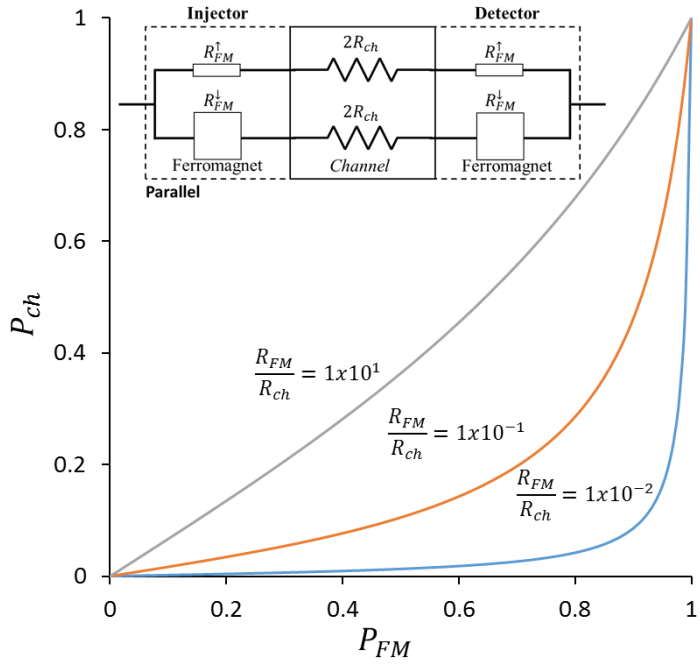

Figure 1.5. Plot of P_{ch} vs. P_{FM} with different FM-transport channel resistance ratios, $\frac{R_{FM}}{R_{ch}}$. The term, R_{FM}, is typically much smaller than R_{ch}, therefore the spin transport channel polarization is expected to be low. A conductivity mismatch exists and should be mitigated to achieve improved spin transport channel polarization, P_{ch}.

From this plot, it is apparent that more realistic resistance ratios will lead to a very low spin transport channel polarization and hence a small, polarized spin current. To mitigate this conductivity mismatch, we increase the FM-spin transport interface resistance by adding a tunnel barrier. Yet another issue arises due to the inability of the introduced resistor model to incorporate interaction between the two spin channels. In the spin transport channel, the conductivities for the up- and down-spins are identical whereas the

FM has greater conductivity for up-spins. Therefore, spin accumulation will occur at the interface yet the spins will tend to backflow into the ferromagnet. In the next section we incorporate the chemical potential difference formed at the interface to fix our two channel resistor model.

1.4.2. Interacting Spin Channels in the Resistor Model

To incorporate the chemical potential difference formed at the FM/transport channel interface, we first define the chemical potential as

$$\mu = \frac{n}{N}, \tag{1.16}$$

where n is the excess particle density and N is the number available states at the Fermi level. This basic definition applies to both $\mu_\uparrow$ and $\mu_\downarrow$. We can then insert the chemical potentials into a PDE diffusion relationship by incorporation of Equation 1.4 to arrive at

$$\frac{\mu_\uparrow - \mu_\downarrow}{\tau_s} = D_{\uparrow\downarrow}\frac{\partial^2(\mu_\uparrow - \mu_\downarrow)}{\partial x^2}, \tag{1.17}$$

where D is the spin diffusion constant and τ_s is the time required for a spin flip scattering event to occur. To arrive at a solution for Equation 1.13 in terms of spin transport length, we define the spin transport distance as

$$\lambda_s = \sqrt{D_{\uparrow\downarrow}\tau_s}\,. \tag{1.18}$$

Now we have a simple, 1D PDE describing the spin diffusion at the interface of the FM and the transport channel. We first establish the 1D coordinate system relating to the injector ferromagnetic electrode and the spin transport channel as our interest lies with only the interface. Besides, both FM/transport channel interfaces are assumed to be identical. Figure 1.7 lays out a schematic establishing the coordinate system and allows the reader to understand the chemical potential difference occurring due to the aforementioned spin accumulation.

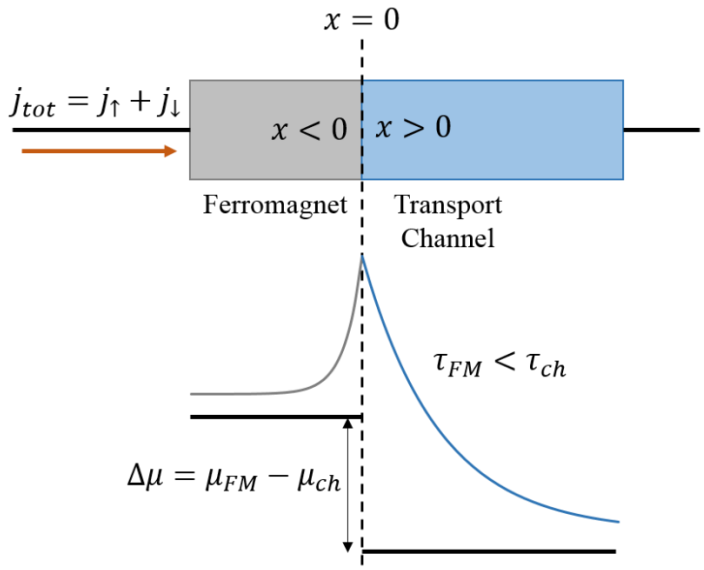

Figure 1.6. FM-Transport channel interface position dependence of chemical potential differences. The FM has a larger chemical potential than the transport channel at equilibrium thereby shown as a splitting or $\Delta\mu$. Relative spin lifetimes are illustrated by different diffusion-based curves for both the FM and transport channel. This model is more accurate than the previous two channel model due to inclusion of the interaction of the FM and transport channel using the definition of chemical potential.

Now that we have established the groundwork for an improved model over the two channel resistor model shown in the previous section, one can solve the PDE in Equation 1.13 and arrive at the general, steady-state spin diffusion relation

$$\mu_{\uparrow\downarrow} = a + bx \pm \frac{c}{\sigma_{\uparrow\downarrow}} e^{x/\lambda_s} \mp \frac{d}{\sigma_{\uparrow\downarrow}} e^{-x/\lambda_s} . \tag{1.19}$$

To define the constants, a, b, c, d, one can use the chemical potential behavior for the up- and down-spins at $\pm\infty$, which is expected to approach $k + \frac{j}{\sigma}x$, where k is a constant. This is the bulk behavior of both the FM and the transport channel. To finally arrive at the solution, one must consider the interface of the FM and transport channel. The boundary conditions require there be continuity of chemical potential across the interface. Van Son et al. discussed that if defining $\mu_0 = \mu_\uparrow - \mu_\downarrow$, and recalling Equation 1.1, we can define the equilibrium chemical potential far from the interface as[83]

$$\mu_0 = \mu_\uparrow P + \mu_\downarrow (1 - P) . \tag{1.20}$$

Both $\mu_\uparrow$ and $\mu_\downarrow$ are continuous at the FM/transport channel interface, however, μ_0 is not due to spin accumulation occurring at the interface creating a voltage offset. Subsequently, the chemical potential difference at the interface can be derived and takes the form

$$\Delta\mu = \mu_{FM} - \mu_{ch} = \frac{P_{FM}^2 \lambda_{ch} j}{\sigma_{ch} + (1 - P_{FM}^2)\frac{\sigma_{FM}\sigma_{ch}\lambda_{ch}}{\lambda_{FM}}} \,. \tag{1.21}$$

This can be rearranged algebraically to help with interpretation as

$$\Delta\mu = \mu_{FM} - \mu_{ch} = \frac{\left(\frac{\lambda_{FM}}{\sigma_{ch}}\right)\left(\frac{\lambda_{ch}}{\sigma_{ch}}\right) P_{FM}^2 j}{\frac{\lambda_{FM}}{\sigma_{ch}} + (1 - P_{FM}^2)\frac{\lambda_{ch}}{\sigma_{ch}}} \,. \tag{1.22}$$

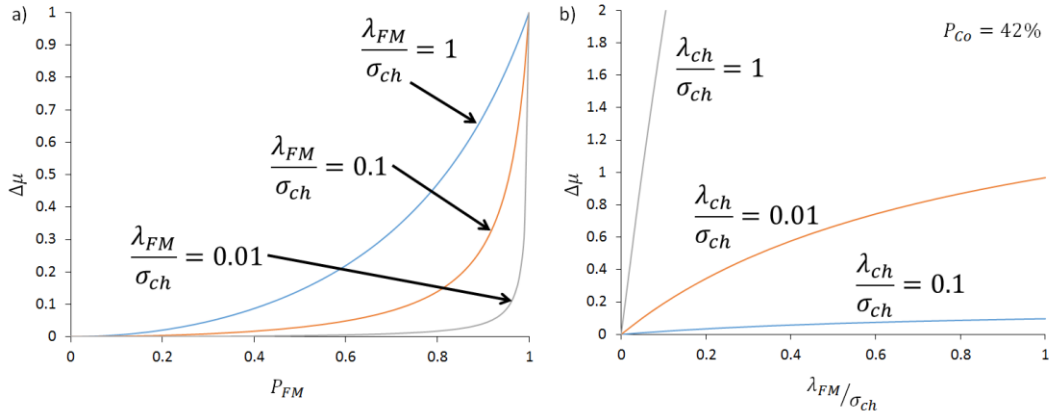

Figure 1.7. Plot of the electrochemical splitting potential, $\Delta\mu$, demonstrating dependence on the spin flip lengths of the FM and channel, λ_{FM} and λ_{ch}, respectively. a) A plot of $\Delta\mu$ vs. P_{FM} for different FM coherence lengths while holding the channel conductivity, σ_{ch}, constant depicts the importance of some finite spin flip length in the FM. In reality, λ_{FM} is typically small with Co having spin flip lengths ~40 nm. b) Using a P_{FM} of 42%, corresponding to Co, $\Delta\mu$ is plotted vs. λ_{FM}/σ_{ch} for different values of λ_{ch}. Holding σ_{ch} constant, it can be seen that a spin transport channel with a relatively long spin flip length has a large effect on the electrochemical splitting potential.

This relationship then defines the spin-based resistance developed at the FM/channel interface by dividing Equation 1.18 by the total current density, j. By doing this, we have derived the interface resistance coupled to spin transport by only using the discontinuity formed at the FM/channel interface.

1.5. Tunnel Barriers: Solving the Conductivity Mismatch Problem

Until this point, we have described the basic principles of a FM/channel interface and the consequences for the electrochemical potential discontinuity. One of the major takeaways is that there exists a conductivity mismatch at the FM/channel interface, which will allow injected spins to flow back into the FM. The associated spin information is then mostly lost. To circumvent this issue, a tunnel barrier can be placed between the FM and channel to facilitate more efficient spin injection[84]. Tunneling conductance is proportional to the product of the density of states (DOS) on either side of the tunneling barrier. Since the DOS for the two spin subbands in the FM (majority and minority spins) is different, a non-equilibrium spin accumulation shall occur within the channel. Essentially, the tunnel barrier acts as a one-way valve that transports a non-equilibrium spin population to the channel while providing an insulating barrier so the spin information does not flow back into the FM and become lost.

Implementation of efficient tunnel barriers offers a host of technical challenges. Efficient tunneling has been demonstrated for spin injection and spin filtering using 2D materials such as fluorinated graphene[26] and hexagonal boron nitride (h-BN)[23] and various materials epitaxially grown using molecular beam epitaxy (MBE)[17,85]. Although

these research efforts have advanced the field of spintronics, they do not offer a cost-effective solution. Therefore, work has been completed by others, which utilizes physical vapor deposition (PVD) to first deposit a metal film onto graphene with subsequent oxidation[28]. Some drawbacks for PVD-based tunnel barriers are weak adhesion to graphene and development of pinholes. Work in this thesis uses similar tunnel barriers with a PVD process that seeks to mitigate the aforementioned issues. Adhesion of the metal to the graphene with resulting oxidation shall be discussed in later sections.

1.6. Spin Valve Implementation

Determination of spin transport parameters intrinsic to channel materials and related to device structures is typically done with basic spin valves patterned with standard lithographic techniques such as photolithography or electron beam lithography (EBL). In this thesis, EBL is used exclusively. Although the basic spin valve has little to do with final application, it is used as vehicle for developing a fundamental understanding of potential spintronics materials. As an emerging electronics field and one of the few, promising targets for beyond-CMOS technologies, it is critical to approach spin polarization, injection, and transport materials from a simplified perspective so that a fundamental understanding of each material can be obtained. In the following sections, two measurement techniques for the spin valve are presented: local and non-local measurements. In this work, both measurements are accomplished using the same device layout known as the non-local spin valve (NLSV).

1.6.1. Non-Local Measurements

Ever since Silsbee et al. first demonstrated non-local spin injection in 1985, the NLSV became widely adopted and a particularly useful configuration for measuring spin transport due to the initial separation of charge and spin current at the injector side of the NSLV[86]. Remaining spin current is then transported across the transport channel *via* diffusion. Upon transport, the detector FM will allow for the measurement of the resulting non-equilibrium spin accumulation. The non-local resistance, ΔR_{NL}, is then extracted as the difference between the non-equilibrium potential probed by the detector FM and the equilibrium potential measured by the Au/Pd/Ti (the metallic contact layered structure used in this work) contact. Au is used to increase robustness of the contact pads, Pd for reducing contact resistance between the metal and graphene, and Ti is utilized as an adhesion layer. The NLSV is frequently used as an experimental device geometry for investigation of spin current transport properties, however, actual implementation of such a spin valve is not practical and a realized graphene spintronics device layout has yet to be demonstrated. A simple NLSV schematic is presented in Figure 1.9. Picking up from Equation 1.15 and 1.16, we can define the spin chemical potential as a function of distance from the FM_{inj} as

$$\mu_{\uparrow\downarrow} = \pm\big(\mu_{\uparrow}P - \mu_{\downarrow}(1-P)\big)e^{-x/\lambda_{ch}} = \pm\mu_0 e^{-x/\lambda_{ch}}, x \geq 0. \tag{1.23}$$

With this relationship we can see the electrochemical potential drops off exponentially when moving away from the injector FM and towards the detector FM. This measurement configuration and relationship is demonstrated below in Figure 1.9.

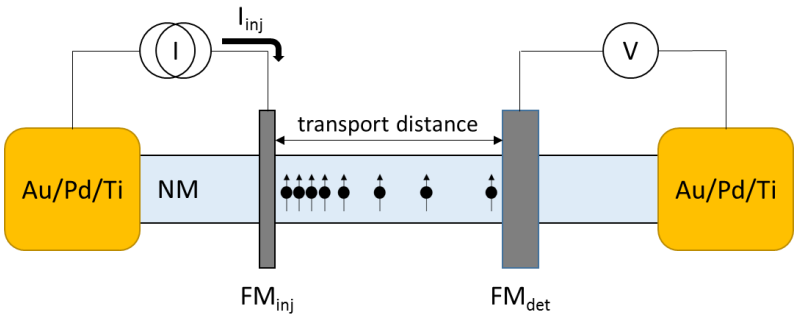

Figure 1.8. A schematic of a non-local spin valve using two FM and metal contacts. Polarized electrons created by injecting current into the FM_{inj} contact. Charge current is then passed to the metal Au/Pd/Ti contact to the left, while the spin current is diffused across the transport distance. Once across the channel, the spin current accumulation under the FM_{det} contact is detected as a voltage with reference to the right Au/Pd/Ti metal contact, which is divided by the injection current, I_{inj}, to arrive at a ΔR_{NL} value.

In a NLSV, there are two major measurement types enabled, which allow for extraction of useful spin transport parameters.

In-Plane Magnetic Sweep

The in-plane magnetic sweep technique utilizes a probe station with variable magnetic field intensity yet uniform field in the region of the device under test (DUT). This is typically achieved with an electromagnetic equipped with a large iron core at each pole. The sample chuck is then situated between the two poles in ambient or within a vacuum chamber. During testing, probes are landed for powering the DUT and measurement while the magnetic field is varied in intensity and sign. For the tests completed within this work, a Lakeshore EMPX-H2 electromagnet-based horizontal field cryogenic probe station was used.

To achieve the non-local voltage (and calculated non-local resistance, ΔR_{NL}), the NLSV must be strategically fabricated to yield a measureable value. This is accomplished by using different widths of injector and detector FM contacts thereby ensuring their magnetic, coercive field strengths, H_c, are different. In this work, the injector magnet was consistently maintained at a smaller value than the detector magnet. In practice, this means the wider FM contact will demagnetize and reverse direction prior to the narrow FM as the wider magnet has a lower H_c. It is also important the difference in FM widths is large enough to yield a wide enough switch during both fast and slow magnetic field scans speeds to ensure repeatable ΔR_{NL} values. In this work, the detector FM contacts were always twice as wide as the injector FM contacts and proved to be repeatable and practical for all measurements performed.

Out-of-Plane Magnetic Sweep (Hanle Effect Sweep)

Out-of-plane magnetic sweeps utilize similar probe stations as described for the in-plane magnetic sweep with a key difference: the magnetic field is oriented vertically or out-of-plane to the DUT. Although the field is oriented vertically, an in-plane magnetic field is still required to switch the DUT into either parallel or antiparallel mode. This effect is attributed to Wilhelm Hanle as the Hanle effect, first described in *Zeitschrift für Physik* in 1924[87]. The same DUTs used for in-plane magnetic sweeps can also be used to observe the Hanle effect as they are intended to extract spin transport parameters directly and indirectly by fitting to experimental data with a Hanle precession model. For this work, a two-pole planar electromagnet was installed into an atmospheric probe station to enable both vertical and horizontal, variable magnetic field with both intensity and sign.

Prior to a Hanle sweep, the DUT was placed into the horizontal magnetic field area while the magnetic field strength was increased until the DUT was in either the parallel or antiparallel state. Next, the DUT was placed into the calibrated vertical field area for a precession measurement.

The Hanle sweep probes the spin transport parameters by dephasing the polarized spins sourced from the injector FM contact through a process known as precession. After both a parallel and antiparallel sweep have been recorded, they are fit using a spin precession relationship for extraction of spin parameters such as

$$R_{NL} \propto \pm \int_0^\infty \frac{1}{\sqrt{4\pi D t}} e^{\left[-L^2/4Dt\right]} \cos(\omega_L t)\, e^{\left[-t/\tau_s\right]} dt. \tag{1.24}$$

The ± sign indicates both parallel (+) and antiparallel (-) sweeps. D is the diffusion constant, L is the spin transport channel length, ω_L is the Larmor frequency ($\omega_L = g\mu_B H_\perp/\hbar$), and τ_s is the spin lifetime. For fitting of Equation 1.20 to experimental data, Matlab, Mathematic, Python, or a similar programming environment can be used to generate best fits. A Python script developed elsewhere[88] was used in this work. A comparison between the in-plane and out-of-plane measurement configurations is depicted below in Figure 1.9a and 1.9b for an in-plane and out-of-plane sweep, respectively.

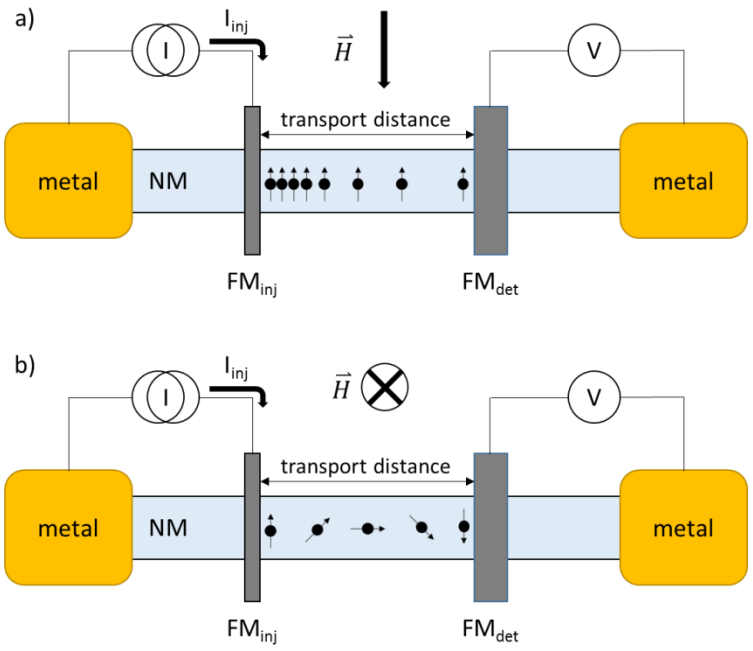

Figure 1.9. A comparison between in-plane and out-of-plane magnetic sweep configurations for NLSV measurement. a) For an in-plane magnetic field sweep, the FM contacts are switched at different field intensities due to distinct coercive forces between a relatively wide and narrow FM contact. b) An out-of-plane magnetic sweep dephases the spin electrons traversing the transport channel when the FM contact configurations are placed in a parallel or antiparallel state.

2. Materials for Graphene Spintronics

Materials development for spintronics is key to technological implementation and recent and future advances are required in order to effectively harness the predicted, spin transport properties of graphene. In the following sections, each material type used in this work shall be described in sufficient detail for the reader to conceptually grasp each component. Each section can act as an independent and brief review for the material described.

2.1. Graphene

Graphene is a 2D crystalline lattice sp^2 allotrope with carbon atoms arranged in a honeycomb pattern. It serves as the basic building block of other sp^2 carbon allotropes as it can be rolled into carbon nanotubes with varying chirality, wrapped into fullerenes, or layered to from graphite where the layer cutoff when multilayer graphene and graphite is still unclear in literature and industry. For a long time, graphene was thought to be unstable by the Mermin-Wagner theorem, which states 2D crystals lose their long-range order and subsequently melt[89]. It was not until 2004 that Novoselov and Geim isolated graphene and proved its stability that 2D crystalline systems were made a reality[34]. It is amazing that a roll of Scotch® tape and a chunk of graphite could usher in such a massive field of research and forever change materials classifications where now the dimensions are defined from zero dimensions (0D, such as fullerenes) to three dimensions (3D, such as graphite and diamond) with the recently discovered graphene establishing the two dimensional (2D) class of materials.

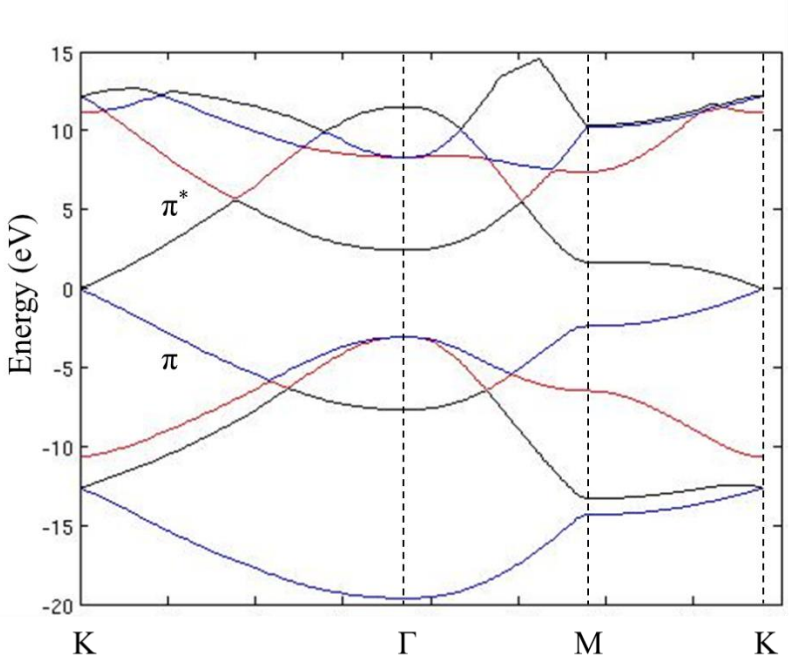

Figure 2.1. Electronic band structure of graphene using a tight-binding model computed with VASP. The K, M, and Γ points in k space are labeled with dashed lines in addition to the bonding (π) and antibonding (π^*) orbital dispersions. Credit to Prof. Bin Jiang at Portland State University for computation of the undoped graphene band structure.

The unique nature of graphene is partly derived from the fact it is one atom thick, hence all surfaces are exposed to the environment, and that the band structure is similar to the Dirac spectrum for massless fermions[90]. This band structure, depicted in Figure 2.1, has resulted in many exciting experimental observations including the quantum Hall effect and Berry's phase[91], nonadiabatic Kohn anomaly[92], and the Klein paradox[93]. In regards to graphene having all atoms exposed to its environment, the proximity effect was discovered, which implies that graphene partially takes on the properties of materials it comes in contact with[4,5,7,13].

Characterization of graphene is primarily accomplished with Raman spectroscopy with knowledge carried over from Raman spectroscopy of graphite. This technique is

non-invasive, has high-throughput capability, and provides several key figures of merit and detailed crystal information that is used for determination of graphene quality. In high-quality graphene, there are only four, primary bands of interest in order of frequency, from lowest to highest: D (~1350 cm^{-1}), G (~1580 cm^{-1} for neutral graphene), D' (~1620 cm^{-1}), and 2D (G') (~2700 cm^{-1})[94]. The D and 2D bands arise from a second-order intervalley process near the K point where one and two transverse optical (iTO) phonons are involved for the D and 2D band, respectively. The D' band, on the other hand, results from an intravalley double resonance process. This only leaves the G band, which is derived from a first-order process with E_{2g} symmetry and a doubly degenerate iTO and longitudinal optical (LO) phonon mode[95]. Generally, the band intensity ratios, $I_{D/G}$ and $I_{2D/G}$, are used to describe graphene quality. $I_{D/G}$ is used to determine the presence of defects and can be used to estimate the defect spacing or defect density[96]. Since the 2D band is derived from a double resonance process only allowed in pristine graphene, $I_{2D/G}$ is used as a relative comparison of graphene quality, which characteristically varies with laser excitation energy[97]. Therefore, it is often misleading to compare $I_{2D/G}$ values if acquired with different laser excitation energy. A more informative approach for incorporation of the 2D band into analysis of graphene is by comparing both $I_{2D/G}$ and the full-width half-maximum (FWHM) of the 2D band. Generally, $FWHM_{2D} < 30$ cm^{-1} with a single Lorentzian fit suggests the presence of monolayer graphene[98]. Presence of the D' band occurs with intravalley scattering and a non-zero phonon wave vector[95].

Besides Raman spectroscopy of as-grown and transferred graphene, other methods for characterization of the thermal CVD (t-CVD) environment must be employed to understand the relationship between the recrystallization of the metal catalyst during the growth process and the resulting graphene. Electron backscatter diffraction (EBSD) has been widely employed for post-growth analysis of as-grown CVD graphene metal catalysts[99–104]. Regarding Cu catalysts, graphene has less than 4% lattice mismatch with graphene compared to the Cu (111) crystal orientation. Graphene primarily registers to the Cu (111) and Cu (100) crystal lattices with high-quality graphene possible with the Cu (111) orientation relative the Cu (100)[49]. Therefore, EBSD is a critical technique for high-resolution analysis of the graphene catalyst surface.

2.2. Ferromagnet Materials: Cobalt

Of all spintronics materials, the most familiar are the normal ferromagnetic materials, which primarily consist of metals where the most commonly used elements are nickel, iron, and cobalt (all transition metals). These three metals have high Curie temperatures that have enabled them to become commonplace in spintronics and mostly used as sources of spin polarized electrons. Other less commonly used materials as spin polarized electron sources, which are actively being investigated in academia are: half-metallic ferromagnets, covalent half-metals, $C1_b$ and $L2_1$ compounds, ionic half-metals, ferromagnetic semiconductors, perovskite manganites, and many more[105]. In this thesis, cobalt (Co) ferromagnetic contacts are used primarily.

2.3. Transition Metal Oxide Tunnel Barriers

Tunnel barriers are necessary to mitigate the conductance mismatch that occurs between a ferromagnet and graphene interface. The carrier density in a conducting ferromagnet is much higher than that of graphene due to the much higher carrier mobility in graphene. This carrier density mismatch is the main cause of the conductivity mismatch. Spin resistance is also much lower in the conducting ferromagnet resulting in a net backflow of spin current when attempting to inject spin polarized current into the graphene transport channel without use of a tunnel barrier contact. This can also be demonstrated by referencing Equation 1.11, where the conductivity of the channel and the ferromagnet are accounted for and the much larger conductivity of the ferromagnet in the denominator drives the polarization to zero.

Experimentally, applying a tunnel barrier to graphene is a non-trivial matter due to adhesion issues of typical transition metal oxides (TMOs) onto graphene. As mentioned in previous sections, other materials have been transferred to graphene to serve as a tunnel barrier, such as h-BN, however, the CVD of h-BN and subsequent transfer are much less mature than for graphene. The alternatives when seeking to apply a TMO onto graphene are atomic layer deposition (ALD) and molecular beam epitaxy (MBE). ALD is typically less successful due to lack of nucleation points available within the basal plane of high-quality graphene and results in a tunnel barrier with pinholes. MBE is very expensive, yet has been demonstrated as a viable research technique when seeding MgO with TiO_2. The least expensive and successful method for tunnel barrier growth is to use physical vapor deposition (PVD). Graphene is sensitive to plasma generated by sputtering and thermal evaporation is difficult to control for very low

deposition rates to achieve the thickness required for use as a tunnel barrier. Therefore, low-energy electron beam evaporation is a key when utilizing PVD. In order to partially mitigate the adhesion issue to the graphene basal plane, a metal is deposited first, which is known to bond to graphene, with a subsequent *in situ* oxidation without breaking vacuum. Titanium is one of the desirable metals to use because of the surface induced *p-d* orbital hybridization that occurs at the titanium-graphene interface[106].

To determine the best tunnel barrier material, two metals were chosen for electron beam evaporation: aluminum and titanium. Aluminum is a good comparison material because alumina is a commonly used for tunnel barriers and aluminum does not exhibit *p-d* surface induced orbital hybridization with graphene. To compare the two barrier materials, 4 Å of each Al_2O_3 and TiO_2 were grown onto graphene transferred to SiO_2/Si wafers with a subsequent electron beam evaporation of 25 nm permalloy (Py, 80% Ni, 20% Fe) as the ferromagnet. The graphene wafers were purchased already transferred by Graphene Square and further processed by a collaborator at Intel Corp prior to FM and oxide deposition. These samples were then analyzed in a scanning electron microscope (SEM) and it was demonstrated the samples with Al_2O_3 tunnel barriers exhibited very large cracks, pinholes, and a large particle size distribution of the ferromagnetic material, Py (Figure 2.2a). However, it was found that the TiO_2-based samples did not exhibit the same cracks and micro-scale pinholes and generally, the particle size distribution of the Py film was much narrower (Figure 2.2b). These two stacks (graphene/tunnel barrier/Py) were then implemented in NLSVs and monitored for DC noise on the injector contacts. Relatively large noise and fluctuations in injection current were observed for Al_2O_3

tunnel barriers while the TiO_2 tunnel barriers exhibited little to no fluctuations and relatively low injection current noise as seen in Figure 2.2c and 2.2d, respectively.

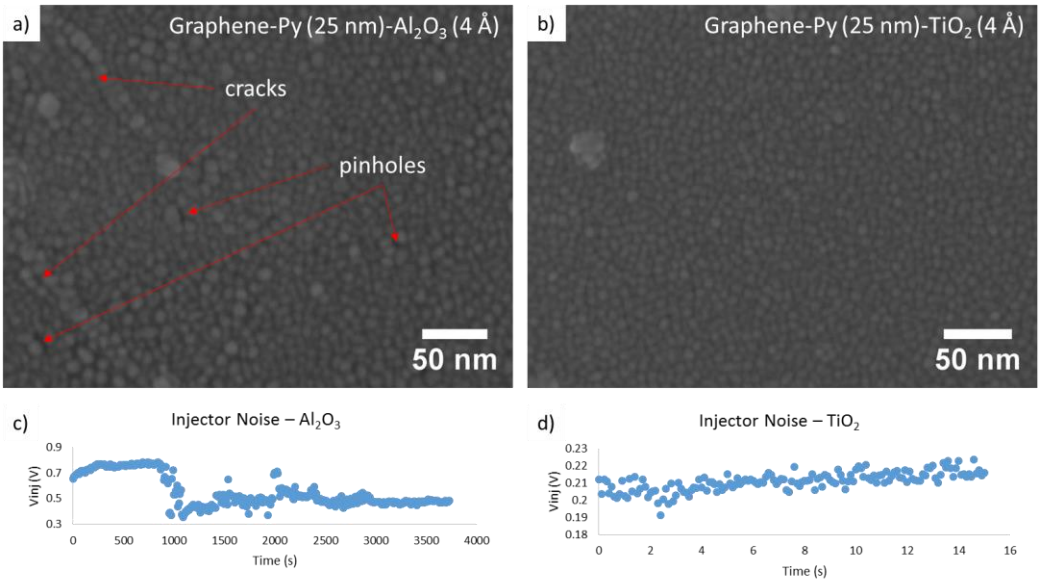

Figure 2.2. A comparison between Al_2O_3 and TiO_2 tunnel barriers grown from electron beam evaporated metal films of Al and Ti. a,b) SEM electron micrographs of graphene/tunnel barrier/Py blanket film stacks using Al_2O_3 and TiO_2, respectively. c,d) Injector noise extracted from monitoring of the injector voltage, V_{inj}, over time, for Al_2O_3 and TiO_2, respectively. The graphene used in this study was purchased from Graphene Square and processed by a collaborator at Intel Corp. After processing, the samples were handed off for deposition of FM and oxide materials for analysis.

3. Wafer-Scale Chemical Vapor Deposition of Graphene

3.1. Si/SiO_2 Support Wafer

Scalable techniques for fabrication of high-quality graphene are critical for adoption of graphene in industry. To date, several techniques have been developed to synthesize wafer-scale, polycrystalline graphene using chemical vapor deposition (CVD), albeit several challenges still remain. CVD of graphene on Cu thin film catalysts supported by SiO_2 represent the greatest challenge for thermal CVD due to the weak adhesion of Cu to SiO_2. Here, we present CVD graphene on Cu thin film catalysts supported by SiO_2/Si wafers using a vertical, cold-wall furnace and catalyst confinement (CC) and analyze the trade-off between high-quality, polycrystalline CVD graphene and reduction of uniformity caused by large wedge-like boundaries formed between Cu grains during the thermal CVD process. It was found that suspended and bilayer graphene was grown across the wedge-like Cu grain boundaries indicating the wedge-like boundaries form during the cooling phase of the CVD process. Raman spectroscopy and scanning electron microscopy (SEM) of the as-grown graphene films reveal the presence of bilayer graphene grown across the wedge-like Cu grain boundaries. Electron backscatter diffraction (EBSD) is used to relate the graphene quality to the Cu crystallinity pre- and post-ambient exposure of the underlying Cu thin film catalyst.

3.1.1. Introduction

In this study, we examine graphene grown *via* t-CVD with a vertical cold-wall furnace and catalyst confinement (CC) using a Cu thin film catalyst supported by SiO_2/Si

wafers. The resulting growths are highly textured due to the amorphous SiO_2 support layer and weak adhesion of the Cu thin film to SiO_2. We study the graphene that spans across wedge-like Cu grain boundaries to understand the relationship between the Cu thin film recrystallized state and resulting grain boundary graphene. This study will help elucidate limitations in t-CVD of graphene due to weakly adhering metal catalysts and provide direction for subsequent process improvement.

3.1.2. Results and Discussion

Although much progress has been made in regards to high-quality, monolayer graphene growth with copper (Cu) foils, Cu thin film-based graphene growth has seen little improvement largely due to the weak adhesion of Cu with the typical underlying substrate, SiO_2, and related evaporative losses of Cu. Therefore, the best route to high-quality copper thin film-based graphene growth is to optimize with an SiO_2 support and either drive the growth process to low temperature with a plasma process or optimize with a thermal growth system bearing in mind high temperature delamination and dewetting issues commonly experience with copper thin films. Here, we report the enhancement of graphene Raman signal intensity due to suspended graphene and bilayer formation at Cu grain boundaries.

After growth of graphene, Cu films formed into grains with a high density of twin boundaries. Largely due to a lack of a crystalline support wafer, the Cu film will form into a polycrystalline surface with an exception occurring for Cu thin films 500 nm thick and with specific growth conditions. Additionally, large separations between Cu grains of

0.5-1.0 µm formed (Fig. 3.1c). Within these separations bilayer graphene forms and stitches together the monolayer graphene highlighted in Fig. 3.1b. Post-transfer, graphene films crack only at the bilayer formed between Cu grain boundaries as indicated by optical inspection in Fig. 3.2d. Using Cu thin films with a thickness of 1.0 µm results in a Cu crystal orientation approaching a random distribution as seen in Figure 3.1c. Even though the Cu crystal orientation is vastly different between a Cu thin film thickness of 0.5 and 1.0 µm, $I_{D/G}$ is less than 0.1 in both cases, with the 1.0 µm thickness having $I_{D/G} \approx$ 0.05. However, the 2D band FWHM of the 0.5 and 1.0 µm samples is 28 cm^{-1} and 35 cm^{-1}, respectively, indicating the 1.0 µm thick Cu sample likely has multilayer graphene when also considering the $I_{2D/G}$ for this sample is 1.05.

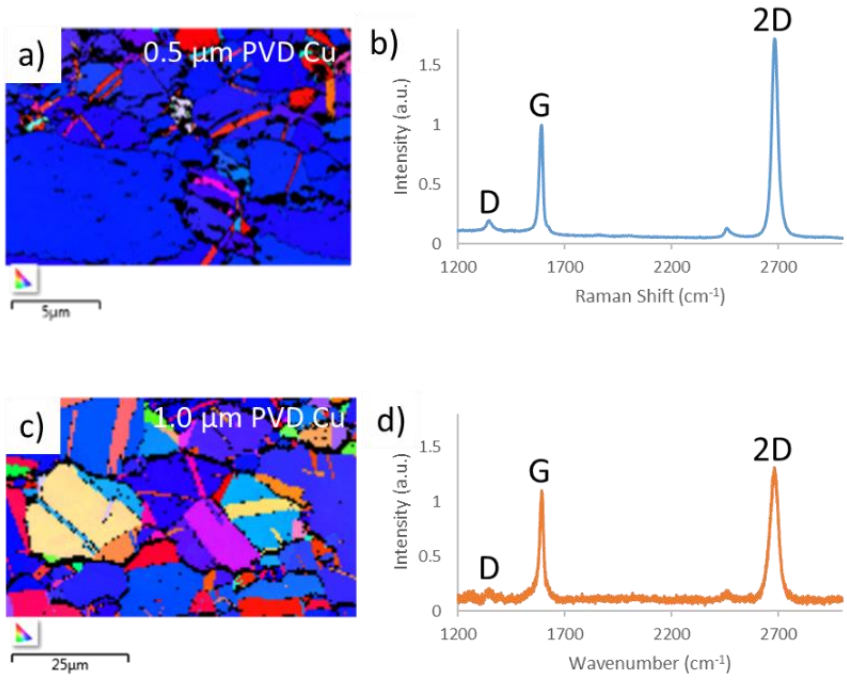

Figure 3.1. Comparison of the recrystallized Cu thin film and resulting graphene quality for 0.5 and 1.0 µm thick Cu films supported by SiO_2/Si. EBSD maps and Raman spectra for CVD graphene grown on 0.5 µm (a,b) and 1.0 µm (c,d) Cu films. Interestingly, the

primary Cu crystal orientation for 0.5 μm thick films is Cu (111) with an amorphous SiO_2 support layer. With a 1.0 μm film thickness, the Cu grain orientation approaches a random distribution with a similar $I_{D/G}$. However, the 2D band broadens with a correspondingly lower $I_{2D/G}$ indicating the graphene is not monolayer.

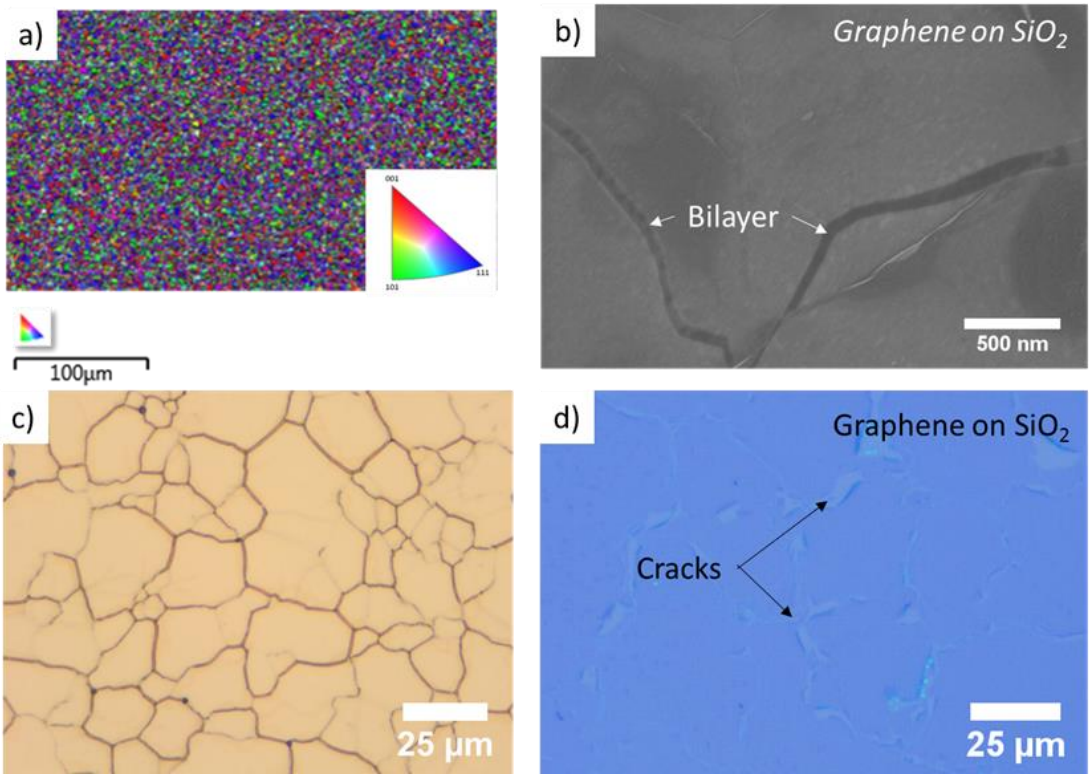

Figure 3.2. EBSD, SEM, and optical analysis of large-grain Cu CVD graphene growth. a) SEM EBSD inverse pole figure for Cu cubic orientation out of the sample plane (z), b) SEM image of the graphene transferred to SiO_2 demonstrating bilayer formation at Cu grain boundaries, c) optical brightfield image of as-grown graphene supported by $Cu/SiO_2/Si$, d) optical brightfield image of graphene transferred to SiO_2 with cracks forming at weak bilayer grain boundaries.

Graphene nucleation density enhancement has been previously identified by Han et al. in accordance with Cu surface morphology[38]. In order to validate the growth of bilayer graphene between Cu grain boundaries, Raman mapping was performed across several Cu grain boundaries in Fig. 3.3a. Interestingly, suspended graphene was

identified occasionally at Cu grain boundaries (Fig. 3.3b) with $I_{2D/G} > 9$ (Fig. 3.3e,h) due to reduced doping, resulting in lowered electron-electron scattering. $I_{D/G}$ did not vary with significant spatial dependence as in Fig. 3.3c. Relative G peak intensity, I_G, is localized to Cu grain boundaries (Fig. 3.3d) where $I_{2D/G} < 1$ (Fig. 3.3b) further indicating bilayer graphene formation at Cu grain boundaries. The 2D peak FWHM was larger at Cu grain boundaries indicated by a large relative shift to monolayer graphene as depicted in Fig. 3.3e. Suspended graphene demonstrated Raman spectra with near-neutral G peak positions having a slight red shift possibly indicating tensile stress present at the bilayer graphene grain boundaries (Fig 3.3g).

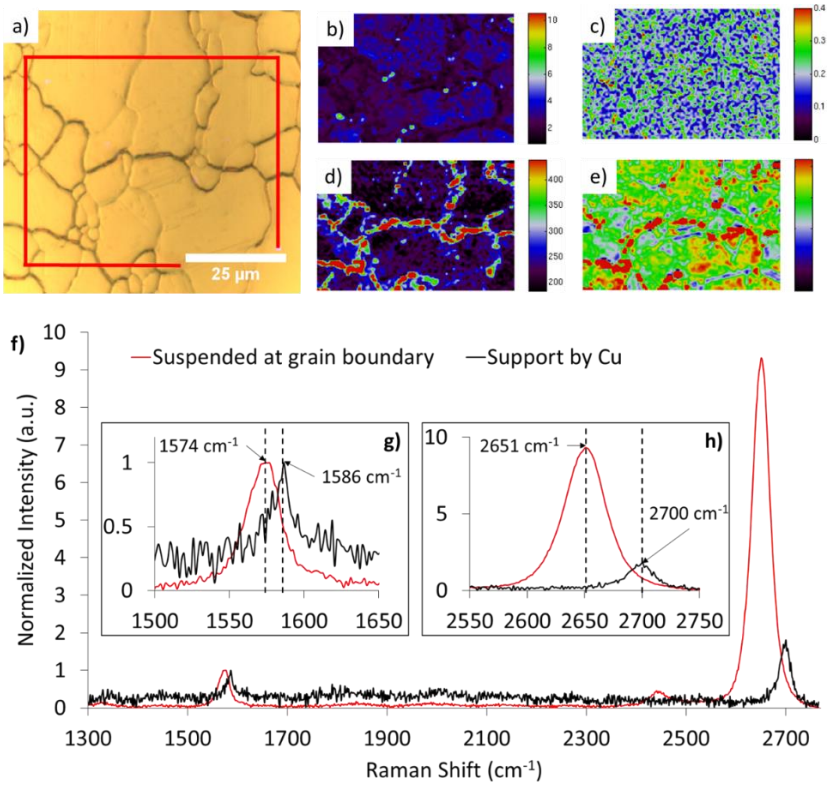

Figure 3.3. Raman study of CVD graphene spanning Cu grain boundaries. a) Optical brightfield image with region of interest marked for Raman maps, b-e) Raman maps for $I_{2D/G}$, $I_{D/G}$, I_G, and 2D relative FWHM, respectively, f) Raman spectra for suspended and

Cu-supported graphene, g) G peak inset depicting relative shift, h) 2D peak inset depicting relative shift and enhancement of suspended graphene.

Since the Raman maps in Figure 3.3 reveal suspended and bilayer graphene across the Cu grain boundaries, it is important to determine the relationship between graphene spanning Cu grain boundaries and graphene intimately attached to the Cu substrate. Therefore, the Cu thin film of the as-grown graphene sample investigated in Figure 3.3 was oxidized in an enriched O_2 environment. Post-ambient exposure, it is apparent that not the entire Cu surface became oxidized, which indicates there is a relationship between the underlying Cu grain and the quality of the graphene. It is known that within a single grain of graphene, it will serve as an excellent passivation layer preventing oxidation[107]. The lightest regions in Figure 3.4a are regions of Cu that have not oxidized during exposure to an enriched O_2 environment. Varying levels of contrast coincide with the relative concentration of oxidized Cu. A high resolution Raman map in Figure 3.4b of the area defined in Figure 3.4a demonstrates the spatial dependence of multilayer and monolayer graphene. The color red and green represent the model spectra extracted in Figure 3.4c and Figure 3.4d, respectively. The Raman spectrum in Figure 3.4d has a broadened 2D peak compared to the spectrum in Figure 3.4c. Additionally, the broadened 2D model is localized to the Cu grain boundaries of the sample even post oxidation. Therefore, this implies the bilayer graphene growth, which was observed to occur across the Cu grain boundaries in Figure 3.3e, is not affected by the Cu-graphene interface post-growth.

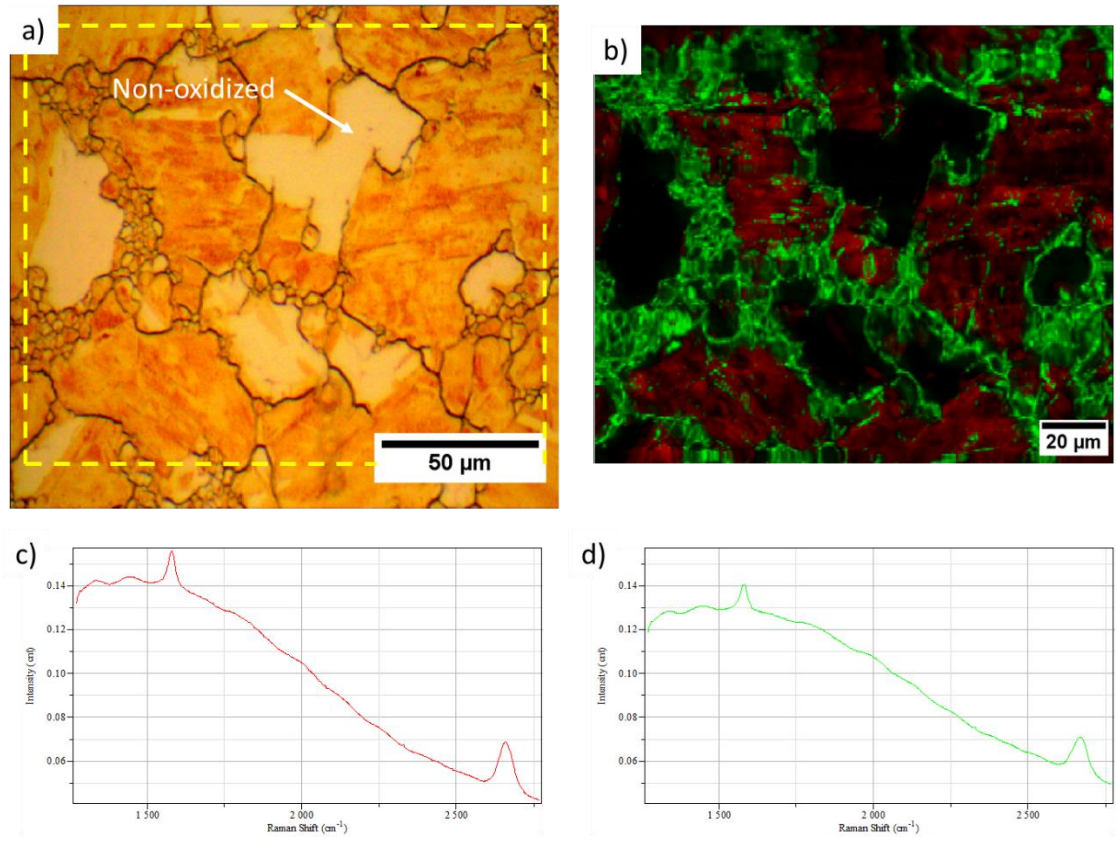

Figure 3.4. High-resolution Raman mapping of oxidized, as-grown graphene wafer using a Cu thin film catalyst supported by SiO_2/Si. a) Brightfield optical micrograph of Raman ROI. The darker, high-contrast areas are oxidized copper while the lighter areas remain free of oxidation. b) Raman map with 500 nm step size depicting two major, extracted spectral components represented by red and green. c,d) The spectra of the corresponding Raman component extracted from the raw Raman map. The Raman spectrum in (c) represents monolayer with a narrowed 2D band and relatively large $I_{2D/G}$ while the Raman spectrum in (d) represents multilayer graphene lacking crystal registration depicting a broadened 2D peak demonstrating turbostratic stacking of graphene layers.

Beyond micro-scale quality inspection with optical microscopy and Raman spectroscopy, it is critical to determine uniformity of as-transferred graphene across an entire wafer. In the semiconductor industry, device yield is a critical component when determining implementation of future technologies. For monolayer graphene, it is especially important to improve yield and uniformity of quality across a wafer since it is

only one atom thick and prone to disorder with an improperly optimized CVD system. In this study, it was found that graphene growth on $Cu/SiO_2/Si$ was largely affected by growth temperature over a small range of temperatures (750°C-850°C). As depicted in Figure 3.5a, $I_{D/G}$ and $I_{2D/G}$ vary significantly from 760°C-780°C. Interestingly, $I_{D/G}$ begins at a lower value at 760°C, and then peaks at a local maximum value at 780°C. This may indicate the carbon layer has transformed to more graphene-like material at 780°C, because generally, amorphous carbon has a $I_{D/G} \leq 1$[108,109]. Additionally, there is a simultaneous reduction in the half-width half-maximum of each Raman band at 780°C indicating tightened selection rules, as seen in Figure 3.5c, which may demonstrate the carbon film is becoming more crystalline. Therefore, it is proposed that when using 1 μm thick Cu as a catalyst, the carbon film transitions into a graphene-like material at 780°C and is the minimum temperature for graphene growth on $Cu/SiO_2/Si$.

When comparing the center growth Raman parameters to the edge, it is apparent the uniformity of the as-grown graphene sample is impacted by thermal uniformity. In this work, a low-mass carbon Joule heating element is used to heat the graphene growth wafers to the desired growth temperature. However, an issue with this method lies in engineering a uniformly heated surface.

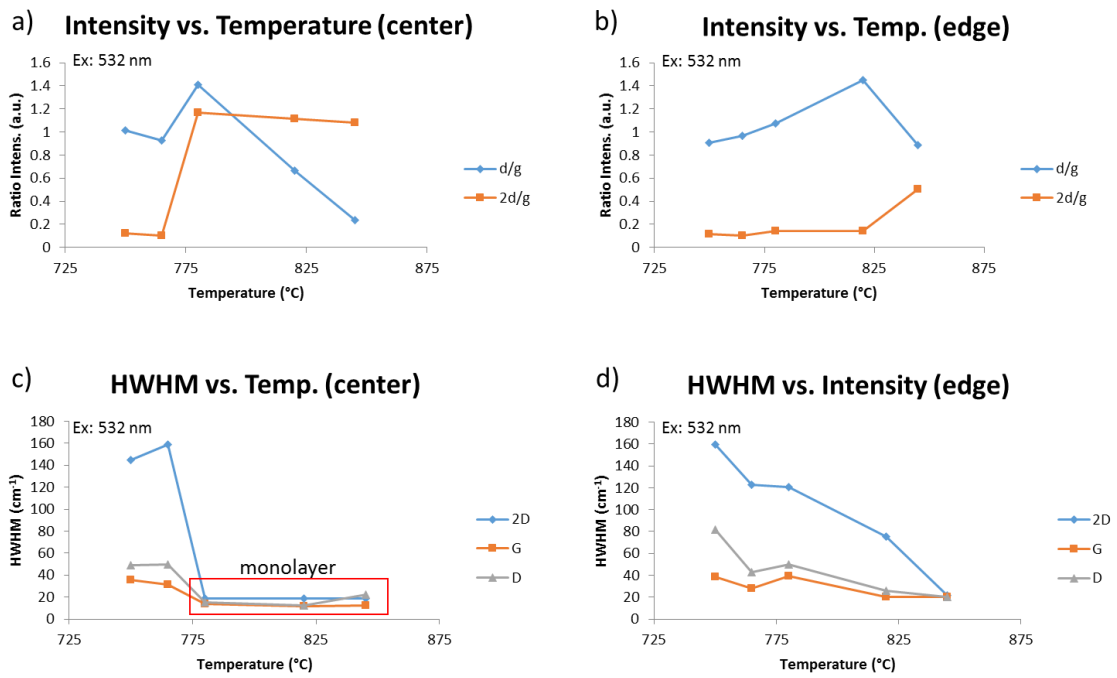

Figure 3.5. Raman analysis of graphene uniformity across a 2" as-grown graphene wafer. a,b) $I_{2D/G}$ and $I_{D/G}$ as a function of temperature for the center and edge, respectively. c,d) Half-width half-maximum (HWHM) of each Raman band (D, G, and 2D) for the center and edge, respectively.

As seen in Figure 3.5b, the characteristic graphene transition point does not occur until 820°C, indicating a -40°C temperature difference from the center to the edge of the graphene growth wafer. This is supported by the HWHMs of the graphene Raman bands in Figure 3.5d, that depict a similar temperature difference with a gradual decline in values converging to a more crystalline state. This data clearly demonstrates the need for highly uniform heating surfaces where even contact is made between the growth wafer and platen.

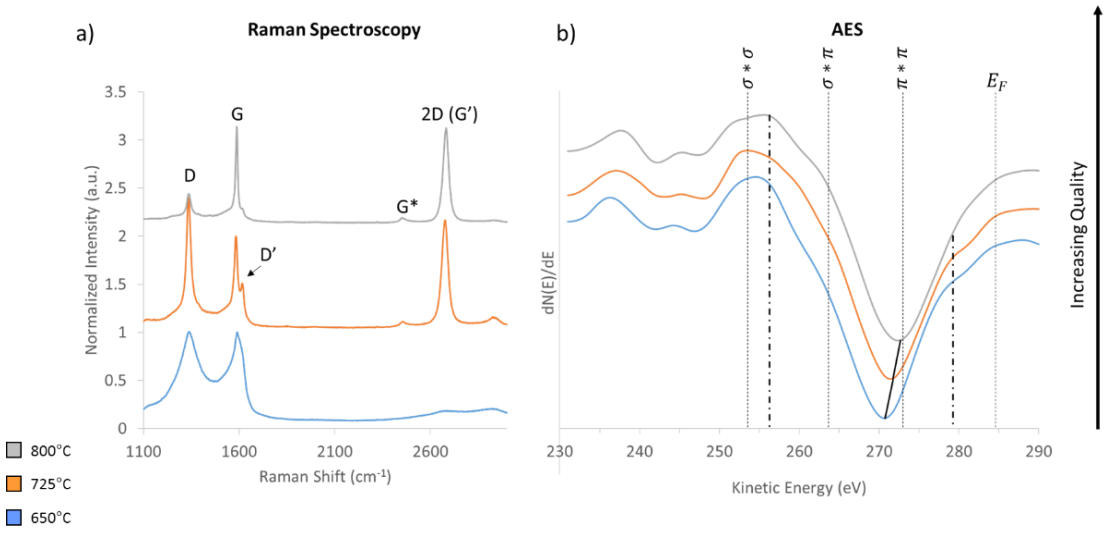

Figure 3.6. Correlated CVD graphene quality data using Raman spectroscopy and Auger electron spectroscopy (AES) as a function of growth temperature. a) Raman spectra of each as-grown graphene sample transferred to an SiO_2/Si wafer. b) First derivative AES C KVV spectra of each graphene sample transferred to an SiO_2/Si wafer. The bonding states involved in the self-folded DOS represented by the total spectrum of each sample is marked in reference to the vacuum Fermi energy level. AES energies associated with damage to graphite layers are marked with thick, dashed lines[110].

To further elucidate the differences between the as-grown graphene samples, the Raman and Auger electron spectroscopy (AES) spectra for select growths is presented in Figure 3.6. It is important to note the temperatures in Figure 3.6 were measured at a position further away from the growth wafer and are therefore lower than stated in Figure 3.5. It was determined experimentally the temperature difference is ≈50°C, coinciding well with the data in Figure 2.5. In Figure 3.6a, it is obvious the graphene grown at 650°C is amorphous-like due to the broad D and G band distribution and the greatly suppressed 2D peak. At 725°C, the 2D peak becomes apparent including G*, D', and overall, significant narrowing of each band. However, the disorder band, D, has sharply increased as we observed in Figure 3.5 once the carbon film transitions from an

amorphous to crystalline state. Increasing the temperature to 800°C results in a significantly lowered D and D' band intensity indicating the as-grown graphene increased in quality and crystallite size. We can estimate the relative crystallite size with the following relationship[96]

$$n_D(cm^{-2}) = \frac{(1.8 \pm 0.5) \times 10^{22}}{\lambda_L^4}\left(\frac{I_D}{I_G}\right), \quad (3.1)$$

where n_D is the defect density (#/cm^2), λ_L is the laser wavelength in nm (532 nm for this work), and I_D/I_G is the same as the $I_{D/G}$. Using this relationship, one can estimate the defect density of each of the two graphene samples represented by Raman spectra in Figure 3.6 as 3.45x10^{11} cm^{-2} ± 9.57x10^{10} cm^{-2} and 4.49x10^{10} cm^{-2} ± 1.25x10^{10} cm^{-2} for the 725°C and 800°C samples, respectively. By increasing the growth temperature by 75°C, the defect density drops nearly one order of magnitude. The trend exhibited with the Raman spectra in Figure 3.6 is confirmed with differentiated C KVV AES spectra as illustrated in Figure 3.6b. The C KVV spectra is useful for characterizing graphene as it represents the self-folded partial DOS (pDOS) for the carbon-containing material probed. For quick reference, the self-folded states of σ*σ, σ*π, and π*π are labeled with dashed lines having equally spaced dashes in Figure 3.6b. It can be observed the σ*σ energy has little change whereas the σ*π energy shows a gradual increase in intensity with growth temperature and the π*π energy is gradually converged upon by the C KVV spectra minima with increasing growth temperature.

Increasing the graphene growth temperature too much results in loss of Cu, which can expose the underlying SiO_2 substrate. Interestingly, as the Cu recedes, low-quality few-layer graphene is left behind as depicted in Figure 3.7a. The Raman spectrum of the as-grown, direct transferred CVD graphene is presented in Figure 3.7b and has $I_{D/G} > 1$ and a broad 2D band. This phenomena has been reported elsewhere[111].

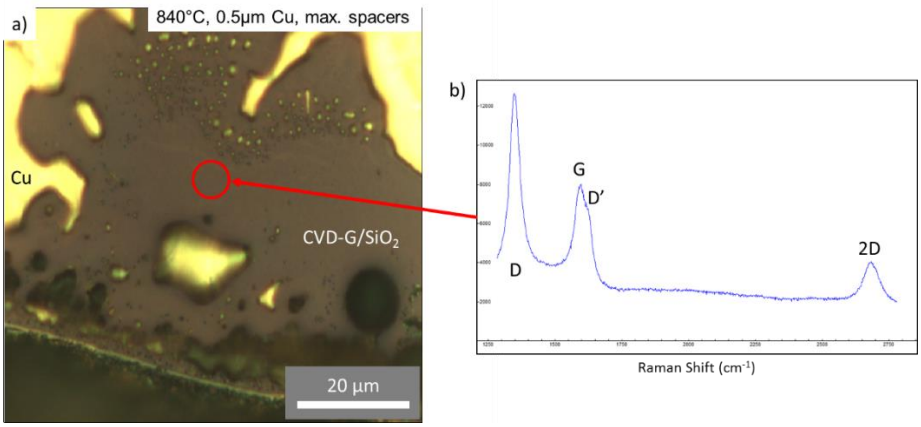

Figure 3.7. CVD graphene is left behind on the SiO_2/Si support wafer after Cu recedes from evaporation during the growth process. a) A brightfield optical micrograph from the edge of an as-grown wafer with substantial Cu evaporation during the CVD growth process. Multilayer graphene is left behind on the SiO_2 from where Cu previously resided. It is possible the graphene was grown on the surface and under layer of the Cu thin film resulting in a multilayer graphene film. b) Raman spectrum taken from spot highlighted in (a) demonstrating a disordered, multilayer graphene film with a relatively large $I_{D/G}$, small $I_{2D/G}$, and broad 2D band.

Low-Temperature Growth of Graphene Using a Remote Plasma CVD System

Up until this point, we have focused upon thermal CVD of graphene with an SiO_2/Si catalyst support wafer. In this section, a low-temperature remote plasma technique for growing graphene is described in addition to the introduction of a purpose-built inductively coupled plasma CVD (ICPCVD) graphene growth reactor. Low-

temperature growth of graphene is especially interesting for direct growth of graphene onto insulators for CMOS backend applications and to improve stability and reduce waste of metal catalysts. Additionally, substrates besides CMOS technologies such as high-temperature polymers can conceivably have direct growth of graphene-like films opening up new, potential applications.

Remote plasma CVD is where the plasma source is located away from the deposition zone so that undesired plasma effects are mitigated at the substrate. If using a localized capacitively coupled plasma (CCP), the deposited graphene has the potential to align the polarizable basal plane of graphene to the electric field and can produce vertically aligned sheets of CVD graphene[112,113]. Conversely, if using a localized inductively coupled plasma (ICP), the as-grown graphene shall be highly defective unless the growth zone is shielded from direct exposure to plasma. There is effort in industry[114] and academia to harness both forms of plasma for growth of graphene with both adjustable morphology and reduced temperature. In this work, the goal was to design and implement a complete ICPCVD growth reactor and optimize the growth conditions down to 400°C, the temperature limit for post-processing CMOS technologies.

In order to achieve the goal of CVD graphene growth down to 400°C, a complete system was designed and constructed with a schematic of the ICPCVD system depicted in Figure 3.8. Gases are first injected into the top of the ICP chamber, with a vertical coil configuration, where a high density plasma discharge is initiated and maintained with an RF source and matching network purpose-built for the ICP coil. When introducing the carbon-based precursor gas (methane, CH_4, or acetylene, C_2H_2), the plasma is

simultaneously diluted with Ar and/or H_2 gases. After passing through the remote ICP chamber, the gases are fed through an aperture that produces a pressure differential between the ICP chamber and the primary chamber. As an optional accessory, a stainless steel showerhead is able to be attached for further improving gas delivery uniformity at the wafer platen/chuck. Baffles are able to be installed near the aperture to prevent direct cross-contamination with accessories installed on either accessory ports.

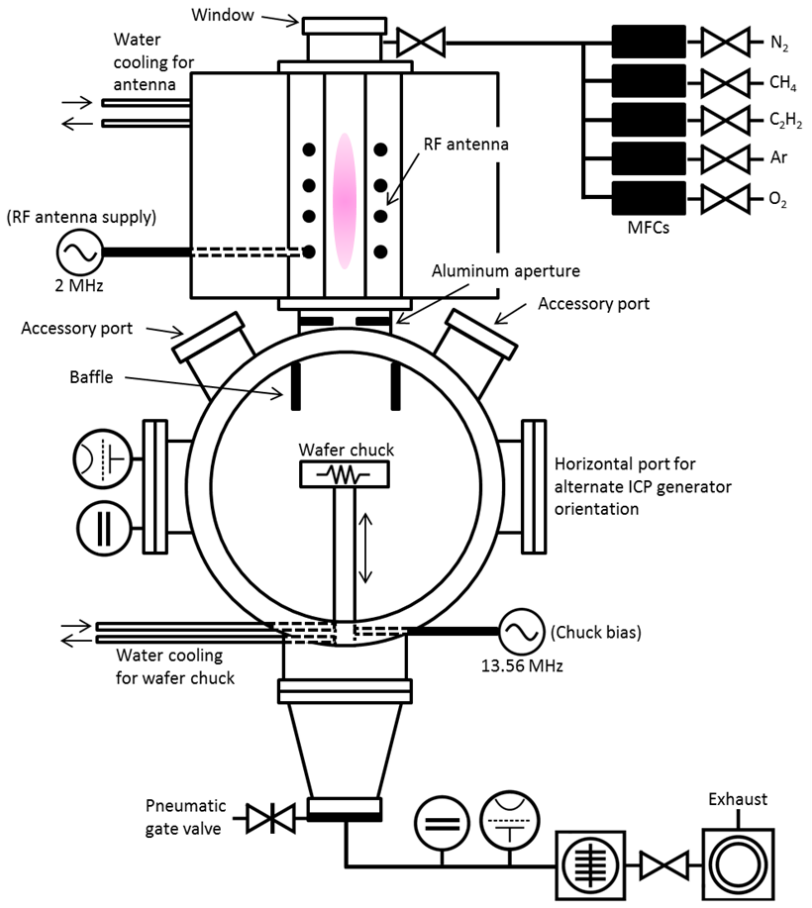

Figure 3.8. Representative schematic of purpose-built ICPCVD system for low-temperature growth of graphene.

The wafer with or without metal catalyst is loaded onto the wafer platen/chuck with high precision radiative heating, variable rotation and vertical displacement, and is isolated for DC and RF biasing for remote plasma modulation and localized CCP generation. Vacuum is modulated and maintained with a variable turbo molecular pump suited for corrosive gases that is backed by a dry scroll roughing pump.

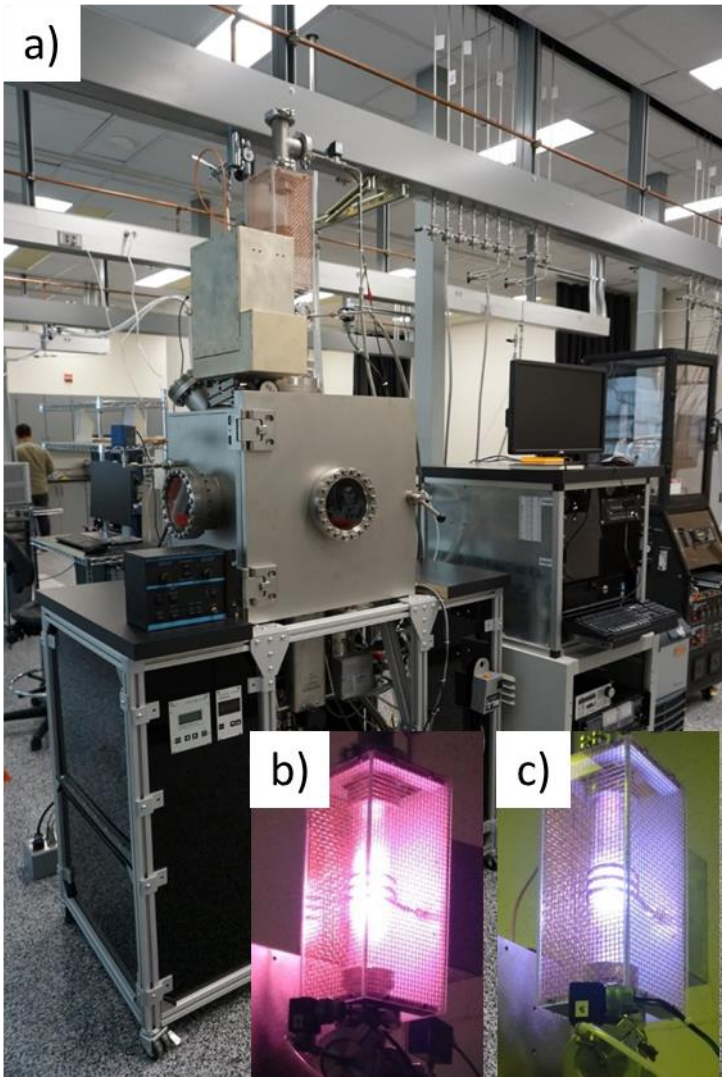

Figure 3.9. Photos of purpose-built ICPCVD system for low-temperature graphene synthesis using a remote plasma. a) Overview photo of the purpose-built ICPCVD system installed within laboratory. b,c) Remote, inductive plasma of Ar and Ar + H_2 + CH_4 at 150 W forward power (13.56 MHz).

The actual ICPCVD system developed with plasma discharge insets is pictured in Figure 3.9.

Graphene growth was then optimized for 1 μm thick Cu thin films supported by SiO_2/Si wafers at 400°C platen temperature. SEM images of the as-grown graphene samples are pictured in Figure 3.10a for thermal CVD of graphene at 750°C and in Figure 3.10b for ICPCVD of graphene at 400°C. It is apparent the Cu grains are much smaller using low-temperature growth of graphene where the catalyst temperature does not exceed 400°C.

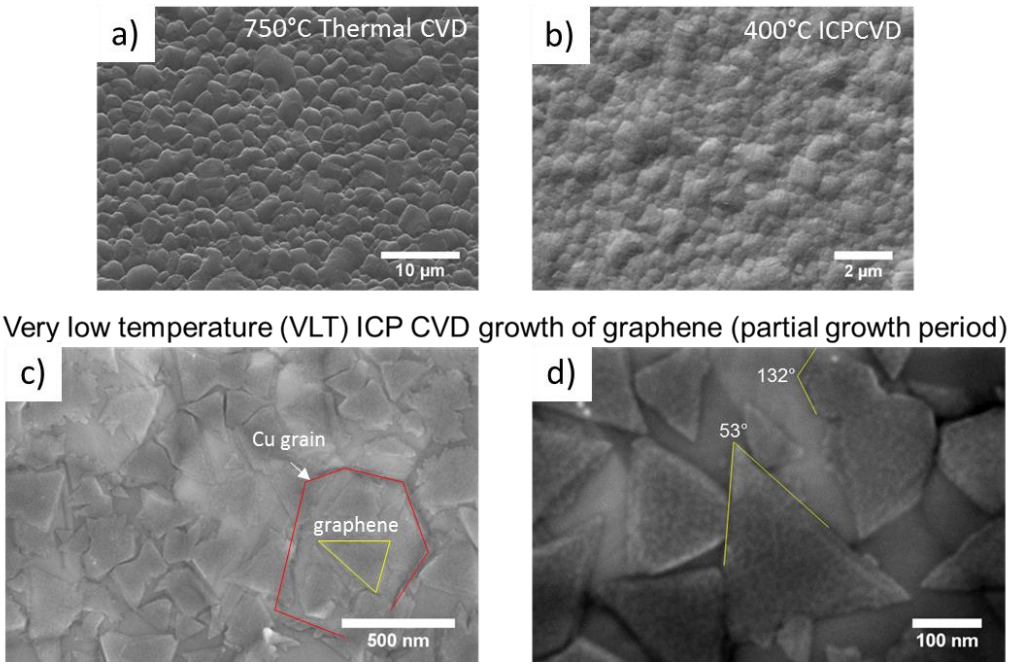

Figure 3.10. Comparative SEM images of Cu grains between thermal CVD and ICPCVD of graphene and SEM images of as-grown graphene at 400°C. a,b) SEM images of thermal CVD (750°C) and ICPCVD (400°C) as-grown graphene at 20 keV. The ICPCVD Cu film surface has notably smaller Cu grains. c) SEM image of as-grown ICPCVD graphene surface depicting a discontinuous film of geometrically shaped graphene

platelets. d) High-magnification SEM image of geometric graphene platelets demonstrating both triangular and hexagonal morphologies.

In addition, the graphene film produced is unlike thermal CVD results where, upon high magnification, low-voltage SEM inspection, it is revealed the film is composed of partially discontinuous, geometric graphene platelets. These results can be seen in Figure 3.10c and 3.10d. A study by Zhang et al. using toluene as the carbon precursor and a growth temperature of 300°C also revealed discontinuous films of geometric graphene platelets with varying morphology as the growth temperature is increased[115]. However, their study involved annealing of the growth substrate at 980°C prior to reducing the growth temperature, which makes the procedure inapplicable to direct growth for CMOS technologies. Although it is posited the discontinuous film was a function of growth time, the film did not form a continuous monolayer up to 30 mins. It is possible the H_2 present in the growth reaction is selectively etching the edges of the graphene platelets causing their growth to be crystalline, however, there may not be enough energy present to overcome the barrier for stitching the graphene grains together, forming a polycrystalline film. The relative crystallinity of the as-grown, low-temperature graphene is extracted from the Raman spectrum depicted in Figure 3.11.

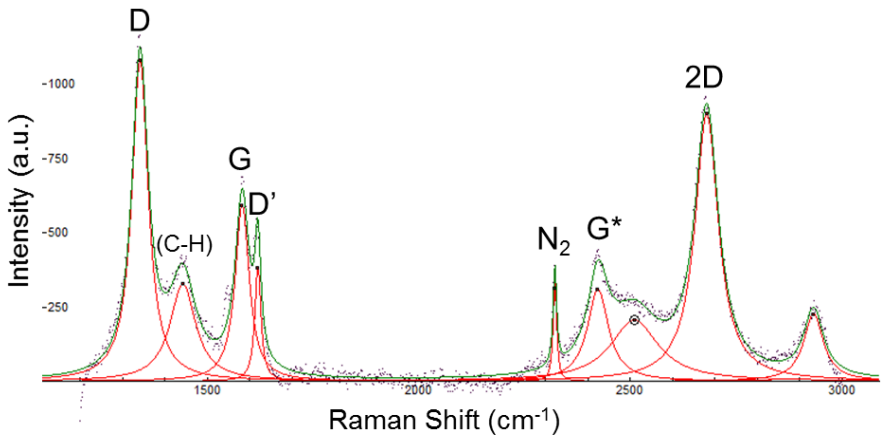

Figure 3.11. Raman spectrum of discontinuous graphene film grown at 400°C using ICPCVD.

The Raman spectrum demonstrates $I_{2D/G} \approx 1.25$, $I_{D/G} \approx 1.70$, $2D_{FWHM} > 30$ cm^{-1}, and the presence of extra Raman bands related to the C-H bond and an unknown peak between the G* and 2D bands. The broad 2D band suggests the platelets may be composed of multilayer graphene and the large $I_{D/G}$ is attributed to the edges of the graphene platelets, which may be dominated by the armchair configuration for low-temperature growth of CVD graphene due to the D band intensity dependence on the concentration of edge chirality[116].

3.1.3. Conclusions

In conclusion, we have demonstrated the key parameters needed for control of graphene quality when using Cu/SiO_2/Si growth wafers with both t-CVD and low-temperature growth using ICPCVD, utilizing a remote plasma source.

3.1.4. Experimental Methods

Materials

Cu thin films were deposited onto 2" SiO_2/Si wafers with 300 nm of thermal oxide first pretreated with 25 seconds of O_2 plasma at 100 W with subsequent DC magnetron sputtering of pure Cu (99.99%) until 1 μm thick at an operating pressure of $5x10^{-3}$ Torr and base pressure of $3x10^{-8}$ Torr.

Thermal CVD of Graphene

The as-deposited Cu thin film sample was then placed directly into either a customized Aixtron BM Pro cold-wall growth reactor optimized for graphene growth. CVD growth of graphene was achieved with a mixture of H_2, CH_4, and Ar at a growth pressure of 19 mbar. The overall t-CVD process time was approximately 15 minutes.

ICPCVD of Graphene (Low-Temperature Growth)

The ICPVD process was completed at a growth pressure of 50 mTorr using Ar to control the background pressure, and a 1:40 mix of H_2:CH_4. Upon growth completion, all gases were removed by the vacuum system with subsequent injection of only Ar at 150 sccm until the platen temperature was < 150°C. The heater and platen temperatures were monitored with a thermocouple and calibrated pyrometer, respectively.

Characterization

Optical inspection and Raman spectroscopy/mapping were performed with a Horiba HR800 Raman spectrometer using an excitation energy of 2.33 eV (532 nm) from a Laser

Quantum Torus narrow line width laser. Raman spectra were captured with a Horiba Synapse CCD camera.

Electron backscatter diffraction (EBSD) mapping and scanning electron microscope (SEM) imaging were both performed with a Zeiss Sigma VP SEM equipped with a Nordlys EBSD camera. EBSD maps and pole figures were generated and analyzed using Oxford Aztec software.

3.2. C-Plane Sapphire Support Wafer

Herein we report a systematic study of elucidating the role of H_2 in graphene synthesis coupled with confined growth with a vertical, cold-wall reactor for achieving high quality and wafer-scale graphene on a Cu thin film using catalyst confinement (CC) and a C-plane sapphire substrate. Our process results in extremely flat and wrinkle free graphene when coupled the growth with a dry transfer process. The role of H_2 was investigated by variation of the H_2:CH_4 flow ratio, led to the identification of an optimum value enabling the mitigation of Cu catalyst roughening. This allows the Cu catalyst to maintain largely monocrystalline extending several centimeters across growth wafers and in the Cu (111) orientation. The ultimate results are high-quality, continuous, and large area graphene sheets. A comparison of graphene formation using the CC process with C-plane sapphire substrate and SiO_2/Si wafers was conducted. The results highlight the benefits of using C-plane sapphire as a substrate in contrast to the SiO_2/Si wafers on which highly roughened catalyst surfaces were usually formed. This not only causes a

high density of wrinkles in the graphene sheets but also induces bilayer growth between monolayer graphene regions at the Cu grain boundaries. Throughout the investigation, graphene quality was evaluated by Raman spectroscopy while Cu catalyst orientation was determined by electron backscatter diffraction (EBSD). Graphene field effect transistors (GFETs) were also fabricated to examine the electronic properties by transferring the graphene from the Cu/C-plane sapphire wafers and from $Cu/SiO_2/Si$ wafers to SiO_2 substrates using an in-house developed dry transfer process. The GEFTs exhibit a consistently-high charge carrier mobility of 3,781 $cm^2/V.s$ from the CC and Cu/C-plane sapphire-based graphene.

3.2.1. Introduction

In this study, we demonstrate, for the first time that high quality and large areas of graphene can be achieved using the combination of C-plane sapphire supported Cu thin films and a cold wall reactor system equipped with catalyst confinement (CC) capability. This growth process was able to achieve thin film Cu grains spanning from hundreds of microns to several centimeters. The largest Cu grains result in the flattest graphene with fewest wrinkles and bilayer islands. Also, high stability of the Cu catalyst was attained due to improved adhesion of the Cu catalyst to the C-plane sapphire in comparison to Cu catalyst on SiO_2. A comparative study presented in this report reveals the advantages of using Cu/C-plane sapphire for graphene fabrication versus using $Cu/SiO_2/Si$, with both being studied in a CC environment. It was also found that H_2 plays three important roles in a CC growth environment by modulating the roughness of the Cu catalyst, controlling

the crystallization of Cu, and catalyzing the generation of re-active $(C_xH_y)_s$ radicals for nucleation of graphene growth.

A photo of the reactor used for this study is depicted in Figure 3.12a. For the graphene growths presented in this study, a typical thermal profile illustrating the recipe used is presented in Figure 3.12b. The cooling phase is achieved by removing power from the resistive heater upon completion of the growth time.

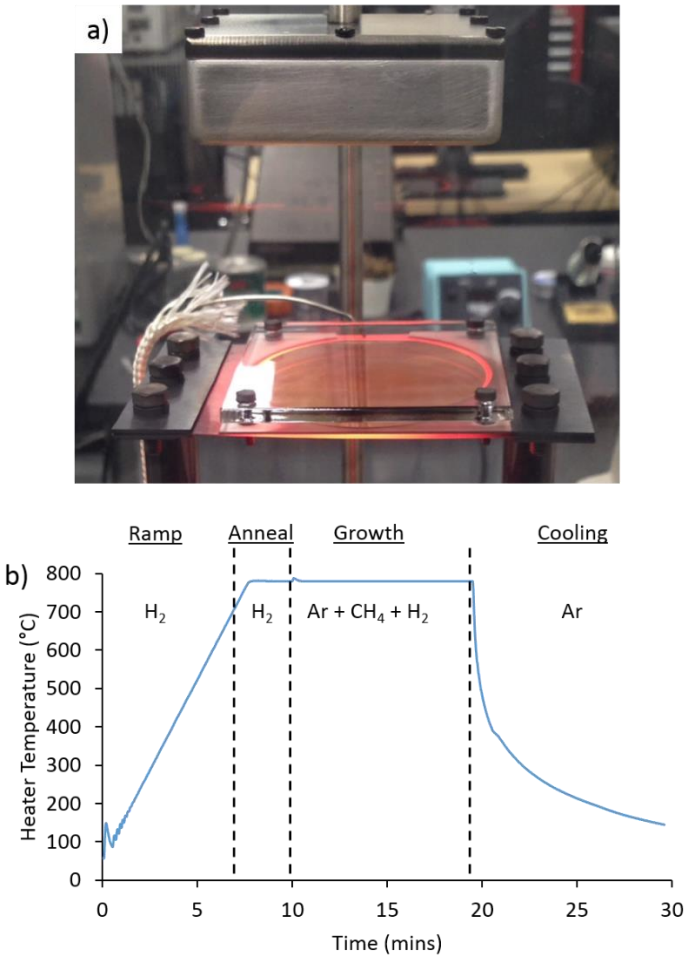

Figure 3.12. Image of thermal CVD graphene reactor and a typical thermal recipe profile. a) Photo of graphene growth reactor used in this study, in-process. Note the quartz plate

fixed above the C-plane sapphire/Cu wafer to enable the catalyst confinement environment. b) Measured heater temperature versus process time demonstrating the different stages of the graphene growth process used in this study.

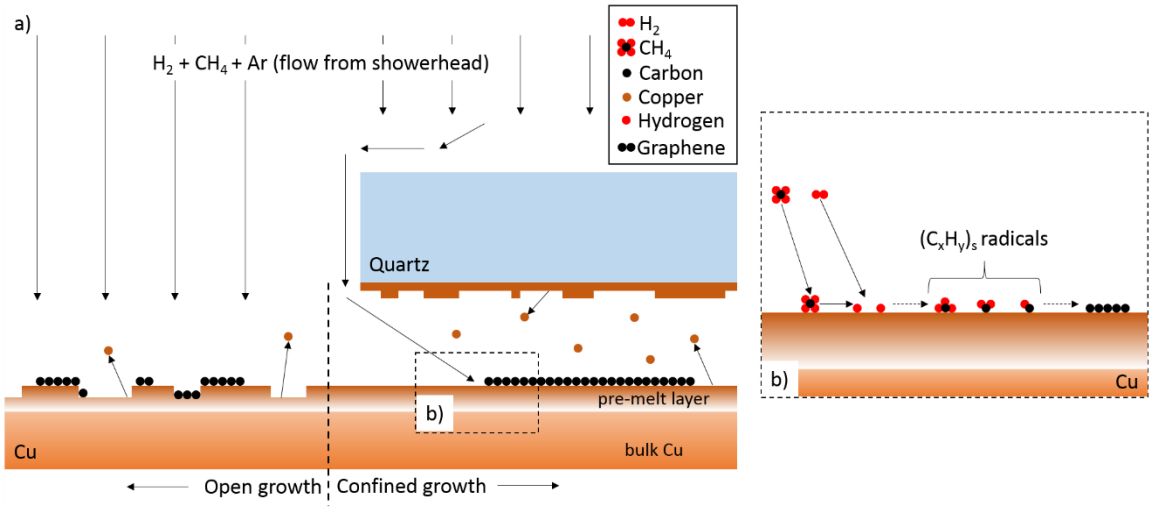

Figure 3.13. A generalized schematic comparing open versus confined graphene growth. a) A schematic comparison between open and confined graphene growth. Open growth allows direct flow of gases from the showerhead and the largest vacuum gradient between the evaporating Cu from the pre-melted layer and the chamber. In contrast, the confined growth method blocks the direct flow of gases to the Cu surface and localizes the evaporated Cu catalyst thereby increasing the surface-bound lifetime of Cu and C surface species during graphene growth thereby enhancing graphene stability during growth. b) An expanded view of the chemical reactions occurring on the surface is depicted to the right.

3.2.2. Results and Discussions

C-Plane Sapphire-Supported Cu Graphene Growth

The particular orientation of C-plane sapphire was chosen due to the crystalline symmetry and low lattice mismatch compared to Cu (111), which subsequently provides the ideal Cu substrate for epitaxial graphene growth. Due to the improved stability, the

Cu/C-plane sapphire wafers are able to maintain uniformity without production of Cu film voids while varying the level of H_2 and keeping the CH_4 flow constant at the lowest attainable level with our current setup (10 sccm). The flow rate of CH_4 was kept low to further reduce nucleation density of graphene thereby increasing the average graphene grain size. The growth series for C-plane sapphire-supported Cu was defined as varying the flow of H_2 from 690 sccm (maximum of mass flow controller on current setup) to 100 sccm and defined the H_2:CH_4 values of 69:1, 50:1, 30:1, 20:1, and 10:1. H_2 serves a critical role in both the production of graphene and the crystallization of Cu. H_2 present on the surface of the Cu catalyst allows for both dehydrogenation of methane resulting in highly reactive and surface bound $(C_yH_x)_s$ molecules that are able to serve as a seed for graphene growth and allows etching of relatively weak carbon bonds resulting in varying graphene growth morphology dependent upon the partial pressure of H_2 during growth[117]. In addition, H_2 serves a third purpose that is more obvious in thin film-based graphene growth, which is to control the crystallization of Cu. H_2 is known to increase the mobility of surface Cu atoms during thermal processing as the H_2 partial pressure increases and at certain concentrations, will produce wedge-like grain boundaries where Cu atoms are highly mobile during the thermal process dominated by surface diffusion of Cu[118]. In contrast to SiO_2-supported growth where an abundance of twinning and wedge-like morphology is observed, C-plane-supported Cu is dominant in Cu (111) crystallographic orientation due to the underlying sapphire acting as a template during thermal processing. However, we do observe the formation of wedge-like grain boundaries only at high H_2 partial pressures. These defects were most likely accompanied by combination of screw

and edge dislocations known to exist between nearby Cu(111) crystal grains[119]. This effect is clearly demonstrated in Figure 3.14 (a,d,g,j,m) as H_2 partial pressure is decreased, the apparent roughening of the as-grown graphene surface decreases. The roughest graphene surface (as shown in Figure 3.14 a,b) appeared when a high H_2:CH_4 ratio of 69:1 was applied.

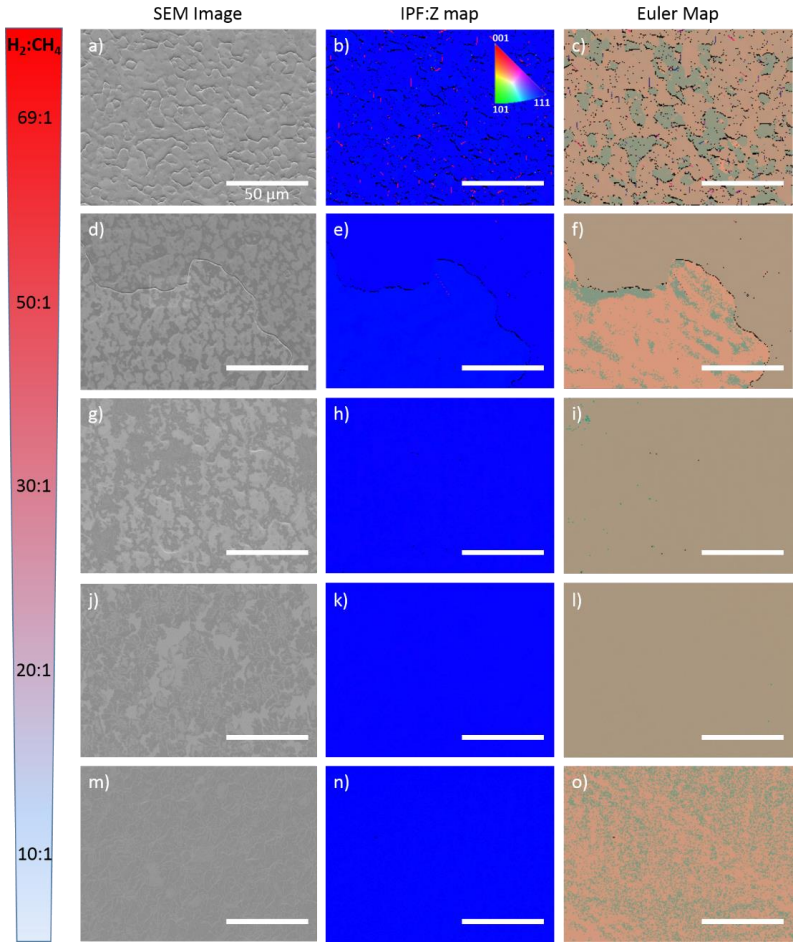

Figure 3.14. SEM images with corresponding electron backscatter diffraction (EBSD) inverse pole figure-z (IPF:Z) maps, Euler maps, and IPF:Z plots. H_2:CH_4 flows of 69:1 (a-d), 50:1 (e-h), 30:1 (i-l), 20:1 (m-p), and 10:1 (q-t).

For every H_2:CH_4 flow ratio used, the Cu catalyst demonstrated a majority Cu (111) orientation as depicted in the inverse pole figure-z (IPF:Z) maps in Figure 3.14 (b,e,h,k,n). However, the relative orientation and grain boundaries varied for each H_2:CH_4 flow ratio and relative Cu grain orientation was monitored with Euler maps as seen in Figure 3.14 (c,f,i,l,o). The Cu crystal orientation of the Cu catalyst thin film coalesces to a single orientation (i.e. single crystal) at H_2:CH_4 of 30:1 and 20:1 as indicated by both IPF:Z plots (Figure 3.14 (h,k)) and Euler maps (Figure 3.14 (i,l)). These samples were mapped over a millimeter scale, as seen in Figure 3.15, and exhibited the same crystallographic characteristics as depicted in Figure 3.14. At the lowest H_2:CH_4 tested, 10:1, the Cu film still maintains the orientation of Cu (111) (Figure 2n), however, the Euler map (Figure 3.14o) demonstrates a lack of a single Cu crystal orientation. This effect demonstrates one of the major roles that H_2 plays with Cu thin film graphene growth: H_2 controls the mobility of the Cu during thermal processing. As H_2 flow is increased, it is likely the Cu mobility (i.e. surface Cu diffusion rate) increases proportionally. At a H_2:CH_4 of 10:1, which the H_2 is much reduced, the smoothness of the graphene surface is much improved. However, the overall orientation is not allowed to approach a single crystal due to lack of H_2. An increase to 20:1 decreases in-plane orientation mismatch (Figure 3.14l) while still maintaining Cu(111) orientation (Figure 3.14k). Hemispherical plots for each IPF:Z EBSD map were generated to further illustrate the large-area crystallinity of each Cu thin film. These hemispherical plots are depicted in Figure 3.17.

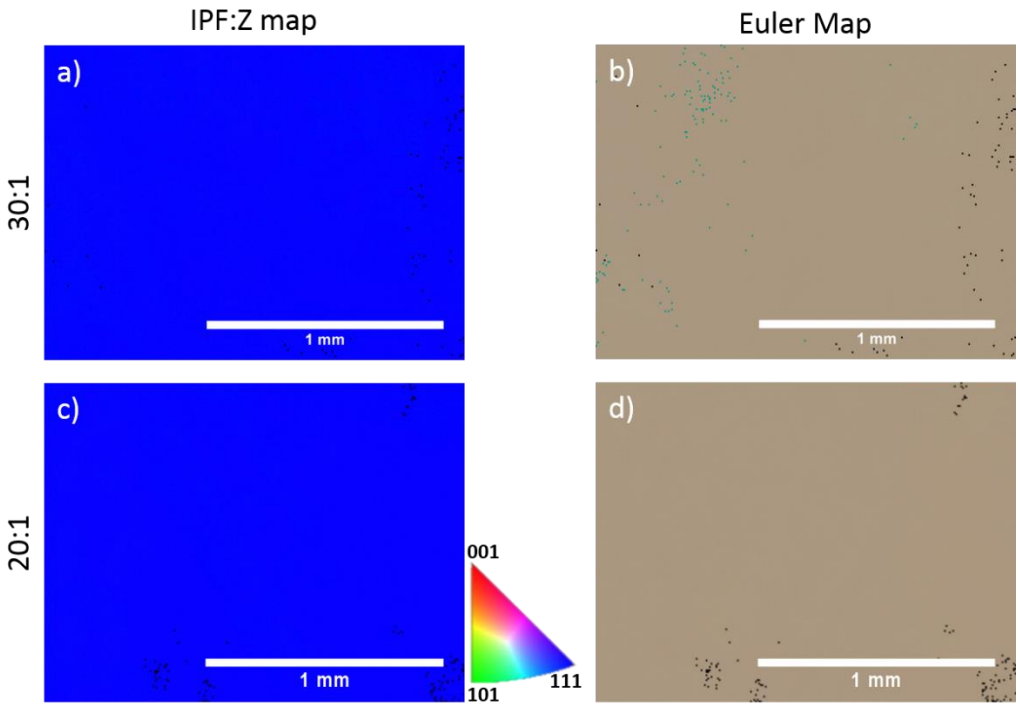

Figure 3.15. Inverse pole figure – Z (IPF:Z) electron backscatter diffraction (EBSD) maps and Euler maps over the millimeter scale of both H_2:CH_4 flow ratios of 30:1 and 20:1, respectively. a,b) Aforementioned maps for 30:1 and 20:1 (c,d).

Secondly, H_2 is also utilized for control of the graphene morphology and growth dynamics[43]. It absorbs onto the Cu catalyst surface and dehydrogenates a CH_4 molecule thereby creating a reactive $(C_xH_y)_s$ species capable of nucleating graphene growth. At the same time, H_2 etches weak C-C bonds favoring the hexagonal structure of graphene[41]. These effects are demonstrated in Figure 4 where SEM characterization was performed for samples made at different H_2:CH_4 ratios. Firstly, the graphene nucleation density can be inferred from the bilayer density present of the surface of the as-grown graphene monolayer. At a H_2:CH_4 of 69:1, the bilayer density is the highest (Figure 3.16a) with bilayer density gradually decreasing as the H_2 flow was decreased (Figure 3.16

(a,c,e,g,i)). The bilayer island density versus H_2:CH_4 flow was extracted using image analysis over several regions of each sample and is presented in Figure 3.16k. The bilayer island density follows an exponential relationship (blue, dashed line represents exponential fit) and demonstrates the importance of H_2 in graphene growth dynamics.

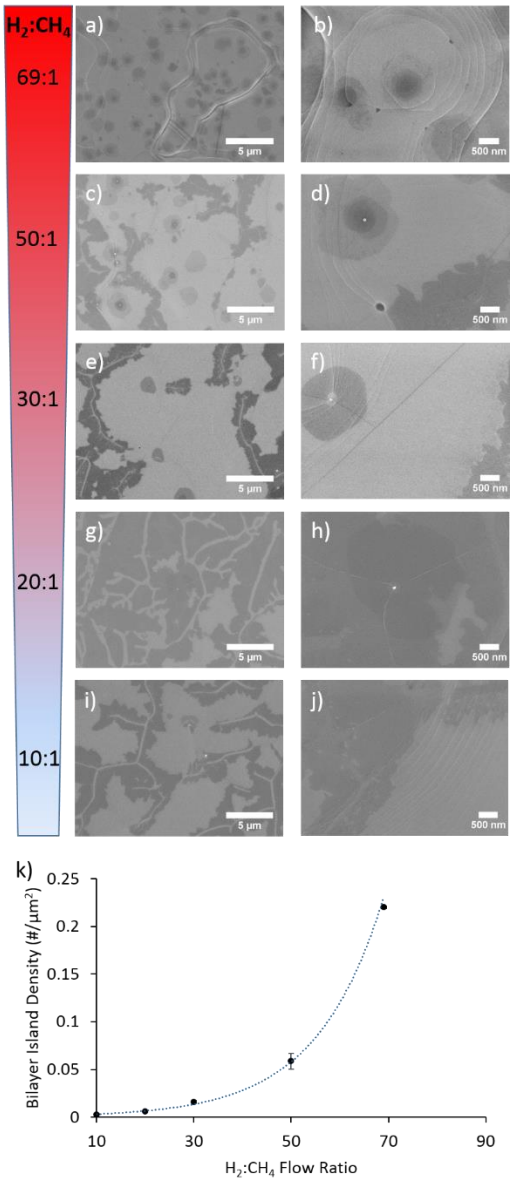

Figure 3.16. Analysis of as-grown graphene morphology for varying H_2:CH_4 ratios with bilayer density dependence. SEM images of the graphene growth series varying the flow

rate of H_2 while holding the CH_4 flow rate constant for H_2:CH_4 values of 69:1 (a,b), 50:1 (c,d), 30:1 (e,f), 20:1 (g,h), and 10:1 (I,j). k) Bilayer island density versus H_2:CH_4 flow ratios for the entire graphene growth series. The bilayer density was extracted with SEM image analysis over several sites on each as-grown graphene wafer. Bilayer density as a function of H_2:CH_4 flow rates follows an exponential trend with increasing H_2. Low magnification SEM images are supplied to demonstrate the differences in graphene bilayer island density while high magnification SEM images supply detailed graphene morphology on the Cu thin film catalyst.

Thirdly, the effect of H_2 can be seen with the shape of the graphene bilayer islands. As the H_2:CH_4 flow ratio is decreased, the bilayer islands go from a hexagonal shape (Figure 3.16b) to a gradually more amorphous structure as seen in Figure 3.16j. Presumably, the reduction of H_2 will reduce the number of weak C-C bonds, which results in a continuum of graphene morphology from symmetric circular shapes to highly dendritic. The onset of dendritic-like growths appear at a H_2:CH_4 of 50:1 as seen in Figure 3.16c (dark veins with lobed edges) and continue to increase in dendritic form from 50:1 to 10:1.

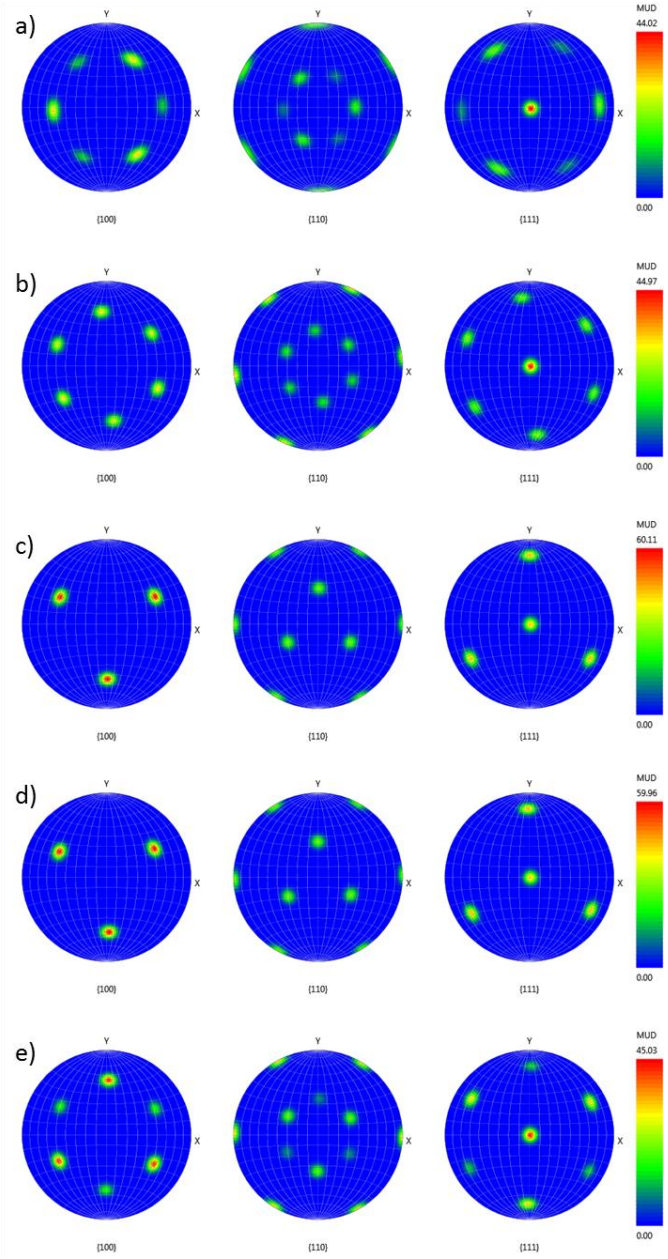

Figure 3.17. Hemispherical pole figures for recrystallized Cu thin films supported by C-plane sapphire wafers. a-e) Cu (100), (110), and (111) hemispherical pole figures for H_2:CH_4 flow ratios of 69:1, 50:1, 30:1, 20:1, and 10:1, respectively. All pole figures are sampled over an area of 2.43 mm^2 (1.80 x 1.35 mm). Only the as-grown graphene wafers which utilized H_2:CH_4 flow ratios of 30:1 and 20:1 demonstrated single orientation, recrystallized Cu thin films.

In order to relate the morphology of the as-grown graphene to its quality, all samples were transferred to SiO_2/Si wafers with 300 nm of thermal oxide. During this study, a unique transfer method was developed that was inspired by work from Lee et al.[120]. To assess graphene quality, Raman spectroscopy of each transferred graphene wafer was performed by recording spectra from the top, bottom, left, right, and center of each transferred graphene wafer. The five spectra for each wafer were then averaged and plotted in Figure 3.18a for each H_2:CH_4. Each of the five spectra was analyzed individually to create a plot exhibiting the trend of $I_{D/G}$ and $I_{2D/G}$ with H_2:CH_4 as seen in Figure 3.18b. The G-peak position for each average Raman spectrum is presented in Figure 3.18a. All but the sample with a H_2:CH_4 of 20:1 have G-peak positions between 1580-1590 cm^{-1} indicating low doping levels. Interestingly, the sample with the lowest G-peak position (H_2:CH_4 of 69:1) also possesses the most promising values of $I_{D/G}$ = 0.040 and $I_{2D/G}$ = 2.29. The next, most promising samples have a H_2:CH_4 of 20:1 ($I_{D/G}$ = 0.059, $I_{2D/G}$ = 2.06) and 10:1 ($I_{D/G}$ = 0.060, $I_{2D/G}$ = 2.11) as demonstrated in Figure 3.18b. Increasing H_2 from 20:1 both increases $I_{D/G}$ and decreases $I_{2D/G}$ until 69:1.

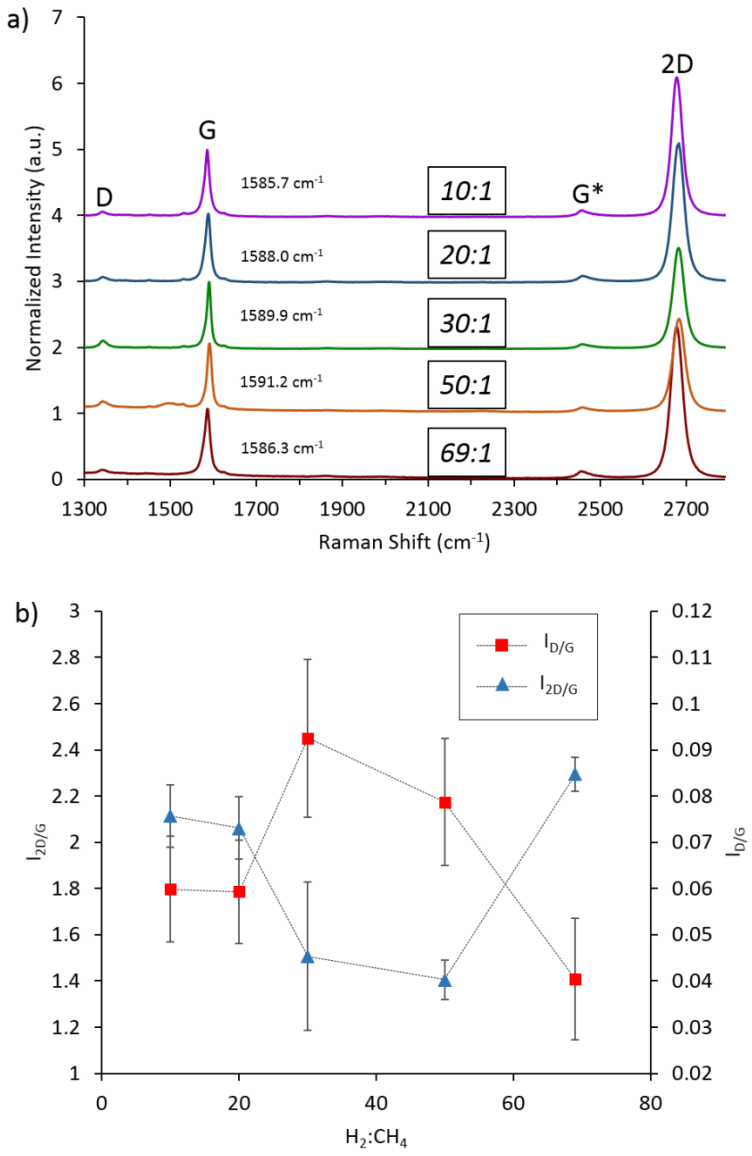

Figure 3.18. Raman spectra for the C-plane sapphire as-grown graphene wafer series. a) Stacked Raman spectra plot (all normalized to G peak intensity) for each H_2:CH_4 with 69:1 (purple), 50:1 (blue), 30:1 (green), 20:1 (orange), and 10:1 (red). All spectra were averaged from five positions on the transferred graphene wafer (bottom, left, right, center, top). G-peak positions are labeled for each spectrum. b) $I_{D/G}$ and $I_{2D/G}$ plotted versus all H_2:CH_4 growth conditions. Average values and error bars derived from five different sampling locations as in (a).

Both H_2:CH_4 flow ratios of 10:1 and 69:1 result in the best graphene quality suggested by Raman spectroscopy results. Contrary to other graphene growth studies using thin film Cu, a high flow ratio of H_2:CH_4 is necessary to attain the best quality graphene as determined by Raman spectroscopy, however, graphene bilayer density increases exponentially from H_2:CH_4 flow ratios of 10:1 to 69:1[121]. In addition to the samples with H_2:CH_4 of 10:1, and 69:1 producing the best graphene, they were the only samples to exhibit a 2D peak FWHM < 30 cm^{-1} of 29.7 cm^{-1} and 28.8 cm^{-1}, respectively, further indicating the majority presence of monolayer graphene. The CC growth regime allows H_2, with a higher diffusivity than that of CH_4, to have an even higher H_2:CH_4 partial pressure ratio inside the CC chamber compared to the remainder of the growth chamber. Then, it is likely the H_2 will etch the graphene anisotropically and Zhang et al. established 800°C is the optimal temperature for etching graphene anisotropically with an angle of 120° and dominated by the zig-zag edge[41]. This can explain both the reduced $I_{D/G}$ (Figure 3.18a) and hexagonal shape of the graphene bilayer islands (Figure 3.16b) for growths with a H_2:CH_4 flow ratio of 69:1. The graphene growths with a H_2:CH_4 flow ratio of 10:1 has nearly 7 times less H_2 and results in less anisotropic etching as evidenced with a larger $I_{D/G}$ (Figure 3.18a). However, this doesn't account for the increased $I_{D/G}$ for every other H_2:CH_4 flow ratio used. We believe the graphene growths with H_2:CH_4 flow ratios of 50:1, 30:1, and 20:1 have a mix of zig-zag and non-zig zag terminations forming during the growth process as evidenced by the shift from hexagonal graphene bilayer islands to circular bilayer islands as depicted in Figure 3.16 (b,d,f,h) going from H_2:CH_4 flow ratios of 69:1 to 20:1. A typical growth and transfer of graphene

using 69:1 is demonstrated in Figure 6. The as-grown graphene sample is quite flat in appearance due to the Cu (111) orientation provided by the C-plane sapphire template and optimized growth conditions (Figure 3.19a). After implementing our dry transfer technique, the graphene demonstrates little to no tears and no visible graphene wrinkles by optical inspection (Figure 3.19b).

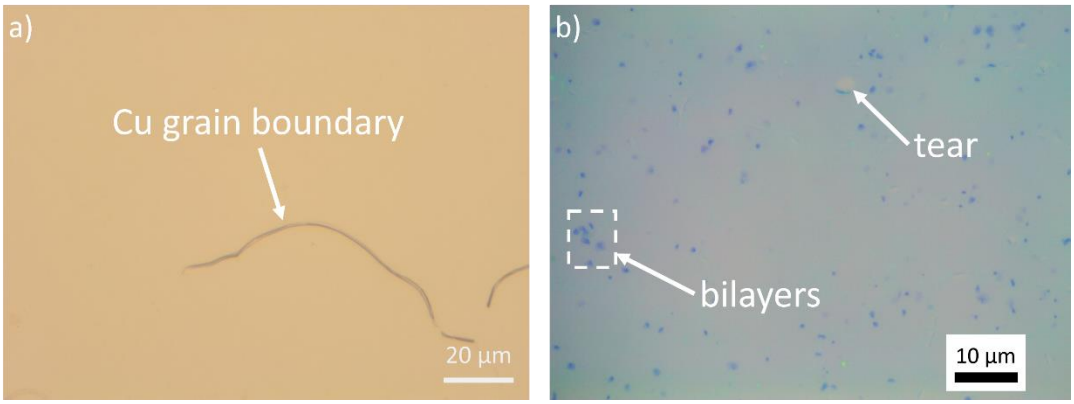

Figure 3.19. Optical brightfield micrographs of as-grown and transferred graphene films with C-plane sapphire wafer supports. a) Optical brightfield image of as-grown graphene on Cu thin film on C-plane sapphire substrate and b) graphene transferred to a SiO_2/Si wafer with 300 nm of thermal oxide.

The best sample as indicated by Raman spectroscopy, H_2:CH_4 of 69:1, was then transferred to a SiO_2/Si wafer with degenerately doped Si for fabrication of graphene field effect transistors (GFETs). Each GFET was fabricated with six, non-invasive contacts and relatively large graphene ribbon dimensions with a channel length of 9 µm and width of 3.5 µm for the purpose of extracting the most accurate intrinsic graphene carrier mobility. An optical brightfield image of an as-fabricated GFET is pictured in Figure 3.20a. The hole and electron mobility were extracted by utilizing a global

backgate and the resulting curve is presented in Figure 3.20b. The electron and hole mobility were extracted using a widely accepted method[47]. Peak electron and hole mobility was measured to be 3,437 cm^2/V.s and 3,781 cm^2/V.s, respectively. A Raman map was acquired for the device pictured in Figure 3.20a. The $I_{2D/G}$ map in Figure 3.20c along with the histogram in Figure 3.20d, generated from the $I_{2D/G}$ map, demonstrate the graphene is predominantly monolayer with an average $I_{2D/G}$ = 2.3 and the mode $I_{2D/G}$ = 2.6. The $I_{D/G}$ map and histogram (Figure 3.20 (e,f)) indicate the graphene channel has a low $I_{D/G}$ ~ 0.05 with some areas shown $I_{D/G}$ < 0.1 likely due to the effect of electron beam lithography processing.

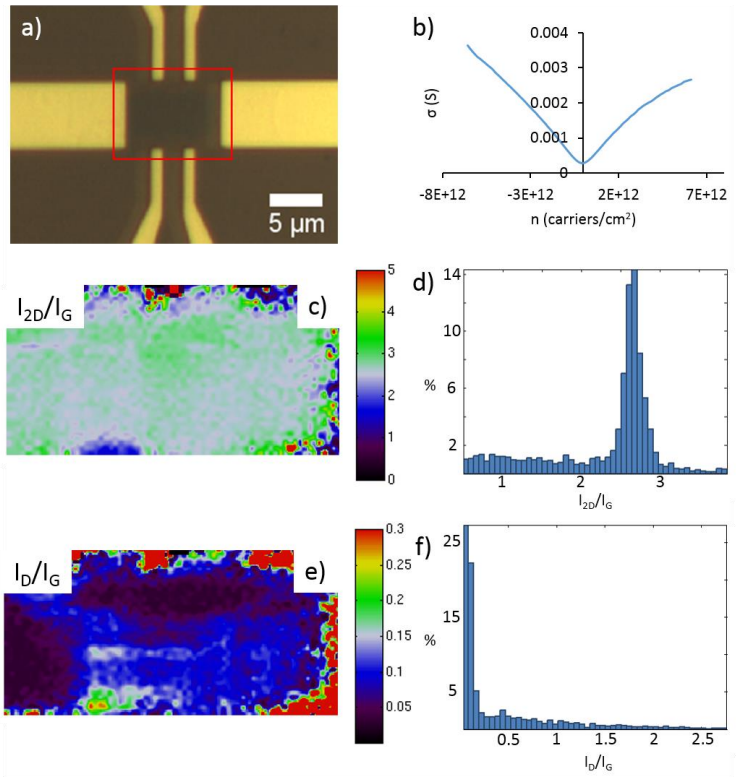

Figure 3.20. Optical and electrical characterization of six-terminal GFETs using C-plane sapphire CVD graphene. a) Optical brightfield image of a 6 terminal GFET fabricated from L3 (H_2:CH_4 = 30:1). b) Dirac curve of the GFET pictured in (a) demonstrated μ_{max} =

3,781 cm^2/V.s. $I_{2D/G}$ (c) and $I_{D/G}$ (e) Raman map of the GFET channel with corresponding histograms (d,f).

SiO_2-Supported Cu Graphene Growth

To compare the quality of graphene growing on Cu supported by C-plane sapphire with that of Cu supported by SiO_2, we conducted a series graphene growth experiments. Our results suggest that Cu supported by SiO_2 is difficult to optimize for thermal graphene growth due to weak adhesion of Cu to SiO_2. Without using CC, the Cu film destabilizes from the SiO_2 forming voids, pinholes, and sometimes complete delamination during the ramp phase of the growth recipe. The distance between the quartz plate and the Cu/SiO_2/Si wafer was varied between 9 mm and 3 mm and will hereafter be referred to as the offset. At an offset setting of 9 mm, the Cu film loses stability and large voids result from the growth process in addition to large amounts of Cu evaporation onto the quartz plate (Figure 3.21a).

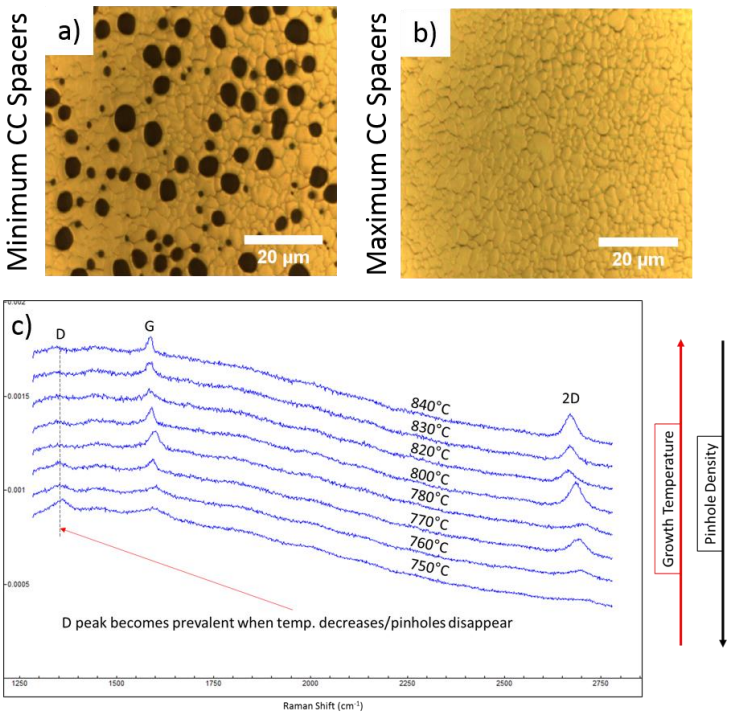

Figure 3.21. Comparison of different offset heights for catalyst confinement, thermal CVD growth process and thermal dependence of $I_{D/G}$. a,b) As-grown graphene on $Cu/SiO_2/Si$ wafer using 9 mm and 3 mm spacer offset, respectively. Note the pinholes and voids present in the Cu catalyst due to enhanced Cu evaporation in (a) when using 9 mm spacer offset. c) Raman spectra of graphene on Cu, using a 3 mm spacer offset, for a thermal growth series demonstrating the reduction of the D peak. However, at 780°C the Cu film loses stability and resulted in pinholes, voids, and sometimes delamination during the growth process.

Low-quality graphene is found within the voids and is presumably left behind after the Cu has evaporated during the growth phase. By reducing the number of alumina spacers to achieve an offset distance of 3 mm, the voids are mitigated and the resultant growth was uniform across the entire wafer (Figure 3.21b). This result was obtained using the same growth conditions when using a 9 mm offset and allowed for uniform graphene growth at elevated growth temperatures. Raman spectroscopy was used to monitor the graphene on Cu to monitor the reduction of $I_{D/G}$ with increasing growth temperature

(Figure 3.21c). It was found that although $I_{D/G}$ reduced with increasing temperature, the Cu film would develop voids above 780°C. Therefore 780°C was chosen as the optimized growth temperature as a compromise between Cu film stability and graphene quality. To achieve both low defect density and improve the grain size of the Cu film, our results suggest that the quartz plate must be cleaned of evaporated Cu from a previous growth, also known as "seasoning", so that Cu grains could increase in size with increasing growth temperature (Figure 3.22 (a-c)). Contrary to results in Figure 3.21, which used a seasoned quartz plate, the growth temperature could be increased while maintaining Cu film stability with a cleaned, quartz plate. Any growth processes performed > 790°C resulted in pinholes and voids forming within the Cu thin film therefore disrupting continuity. After transfer, however, the optimized, 790°C growth on SiO_2/Si demonstrated cracking likely derived from large gaps formed between Cu grains.

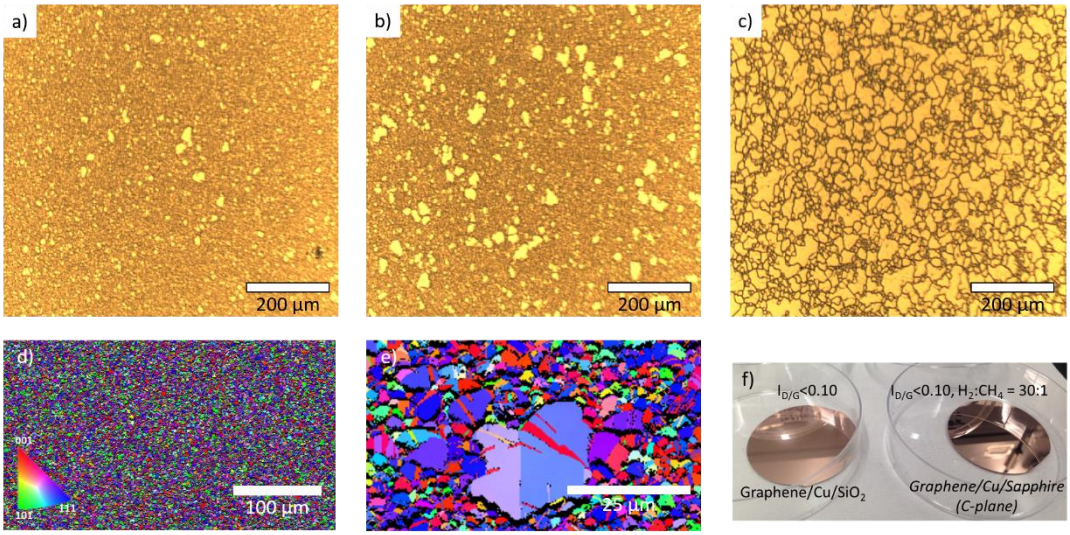

Figure 3.22. Relationship between Cu grain size and growth temperature using catalyst confinement and SiO_2/Si support wafers. (a-c) Optical brightfield microscope images of as-grown graphene of 770ºC, 780ºC, and 790ºC, respectively. The average Cu grain size enlarges as temperature is increased only by using catalyst confinement. Beyond 790ºC the Cu film destabilizes and results in delamination and pinhole formation thereby disrupting continuous graphene sheet growth. d) SEM EBSD map of the 790ºC sample over a large area. e) Enlarged section of map in (d) demonstrating large amounts of Cu grain twinning and heterogeneity of crystal lattice projected out of plane. f) Photos of as-grown graphene wafers supported by SiO_2 (left) and C-plane sapphire (right). The inherent smoothness of the sapphire supported sample is demonstrated with less diffuse reflection.

Without cleaning of the quartz plate, the residual Cu layer from "seasoning" would prevent the Cu grains from increasing in size regardless of growth temperature. The onset of Cu crystal grain growth was observed at a heater temperature of 770°C (Figure 3.22a), increasing gradually at 780°C (Figure 3.22b) and reached a maximum size at a heater temperature of 790°C (Figure 3.22c). The largest Cu crystal grains observed were up to ~80 µm in length, which are some of the largest observed using similar methods, yet the offset used in this study is much larger at 3 mm and the total growth process is 35 minutes. In stark comparison to the C-plane sapphire supported Cu

graphene growths, the resulting Cu crystalline orientation was more random as demonstrated in Figure 3.22d and the inset in Figure 3.22e. A macro view of the 2" diameter as-grown graphene wafers comparing SiO_2 and C-plane supported Cu thin film catalyst is depicted in Figure 3.22f. The C-plane supported Cu is shinier due to the larger Cu grains, and in the case of Figure 3.22f, which depicts the as-grown graphene wafer with a H_2:CH_4 flow ratio of 30:1, the Cu grains extend over several millimeters.

To compare the difference in graphene quality between the different Cu grain sizes developed with the as-grown graphene wafers depicted in Figure 3.22 (a-c), the graphene was transferred to SiO_2/Si wafers with 300 nm thermal oxide. It was found there exists a compromise between graphene quality as determined by Raman spectroscopy and the resulting morphology post-transfer. The as-grown graphene wafers with the smallest Cu grains was grown at a heater temperature of 770°C and has a resulting transfer with excellent uniformity and lacks any visible cracks or wrinkles (Figure 3.23a). However, $I_{D/G}$ for this sample is ~0.15, which is generally low-quality graphene (Figure 3.23c). In contrast, the as-grown graphene wafer with emergence of large Cu grains with a heater temperature of 780°C results in $I_{D/G} \approx 0.11$. The compromise is then observed in Figure 3.23b where cracks form in the graphene post-transfer following the Cu grain boundary morphology. This graphene has improved quality as determined by Raman spectroscopy, however, it is unusable for device array fabrication with such a high crack density.

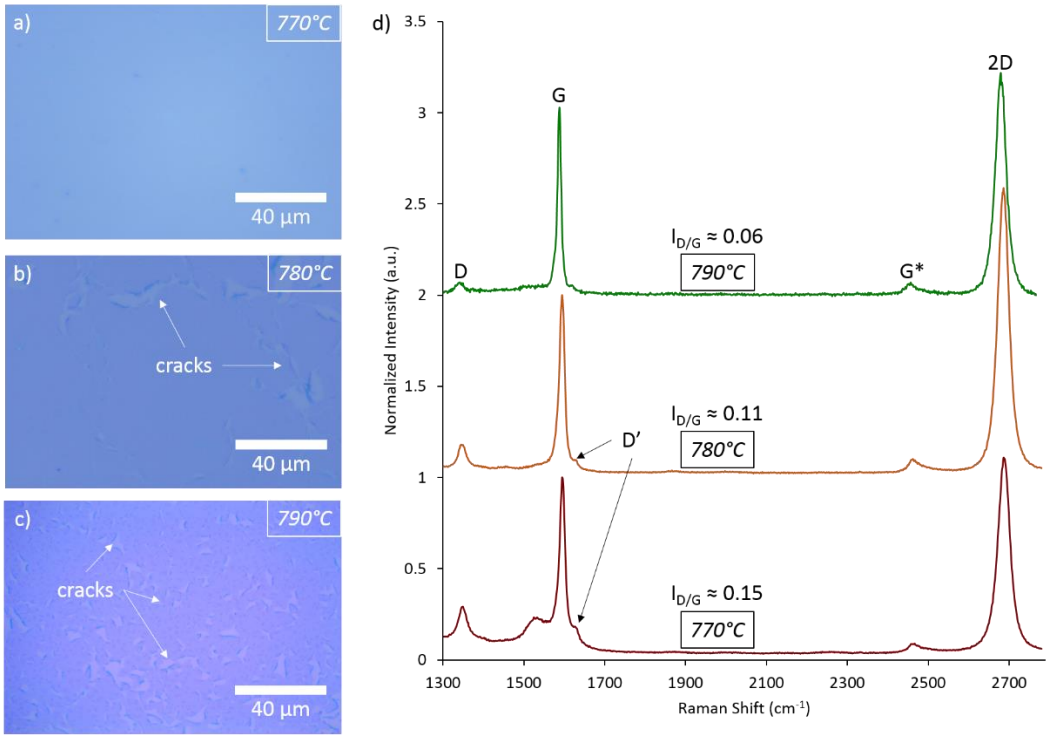

Figure 3.23. Optical brightfield micrograph and Raman spectra investigation for transferred graphene derived from large grain Cu growths on SiO_2/Si support wafers. a,b) Optical micrograph of graphene transferred to SiO_2/Si substrate with 300 nm thermal oxide of unseasoned quartz cap CC growths at 770°C and 790°C, respectively. The as-grown graphene samples corresponding to these transfers are featured in Figure 9 (a,c). Note the cracks derived from the large gaps between Cu grains that are formed after transfer. c) Raman spectra of each graphene sample transferred to SiO2/Si wafers with 300 nm thermal oxide for 770°C, 780°C, and 790°C using an unseasoned quartz cap or CC. The $I_{D/G}$ decreases with increasing growth temperature and Cu grain size, however, the large gaps between Cu grains causes cracks to occur post-transfer.

As demonstrated with first, Cu/C-plane sapphire, and then Cu/SiO_2/Si support wafers, graphene growth by a cold-wall reactor equipped with CC empowers a unique fabrication system amenable to semiconductor industry owing to utilization of rigid wafer supports with a relatively short process time. Especially, the resistive graphite heater offers rapid heating and cooling capability while the use of thin film Cu derived from a

high purity PVD sputter process allows for control of film quality, thickness, and as-deposited purity in contrast to extruded Cu foils. Without CC, the direct gas flow from the showerhead will impinge upon the Cu catalyst film resulting in turbulent flow (Figure 3.12, 'open" growth). This direct gas precursor bombardment not only results in a larger evaporated Cu pressure gradient but also causes the Cu losses to increase thereby decreasing the surface-bound lifetime of each absorbed carbon atom. Also, the graphene seed nucleation density is high due to direct flow from the showerhead. The result is a graphene film with relatively small graphene crystalline domains. After the addition of a quartz enclosure or CC, direct flow of gases from the showerhead is blocked and the gases must diffuse inwards from the sides (Figure 3.12, confined growth). H_2 has a higher diffusivity than CH_4 in a blocked growth regime and results in suppressed convection and slow transport of CH_4 to the Cu surface[44] and therefore further reduces the amount of available carbon precursor species relative to H_2, which results in an overall reduction in graphene seed nucleation density. This effect coupled with the confinement of evaporated Cu allows for the Cu evaporation rate to decrease as the relative concentration of Cu within the enclosure and local to the Cu thin film surface is increased. In the meantime, the graphene nucleation density is under control by optimizing the CH_4 and H_2 flow ratios. This allows the graphene domains to continue growth outwards resulting in larger graphene domains. The cooling phase is achieved by removing power from the resistive heater upon completion of the growth time.

The evaporated Cu during the growth of graphene will coat the inner walls of the reactor chamber thereby presenting an undesirable process for the semiconductor

industry. This issue is further exacerbated with the usage of SiO_2 as a Cu catalyst support due to sometimes unpredictable stability during thermal graphene growth. Therefore, C-plane sapphire and CC allows for these issues to be mitigated as Cu thin films have excellent adhesion to C-plane sapphire and the CC setup prevents coating of Cu onto the walls of the reactor chamber. CC also lessens the loss of Cu during processing allowing for lengthened growth periods when driving nucleation density lower as well as modulating very low carbon precursor flow. We have established a baseline understanding of the growth process and the role of H_2 in this study. This work will aid in advancement of wafer-scale graphene using Cu thin films most amenable for the semiconductor industry using a thermal-CVD process.

3.2.3. Conclusions

In this study, we systematically optimized the growth conditions required for epitaxial formation of high quality and large areas of monolayer graphene onto Cu (111) catalyst supported by C-plane sapphire using the catalytic confinement (CC) method. Specific growth conditions were demonstrated by the growth temperature of 780°C with varying H_2:CH_4 flow ratios. For comparison, graphene was grown using CC and a SiO_2/Si support wafer in addition to C-plane sapphire supported Cu thin films. For graphene grown on Cu (111) templated by C-plane sapphire, the effect of H_2 was investigated. H_2 plays several important roles in determining the growth outcome such as: (1) as H_2 flow is increased, bilayer island density increases exponentially, (2) increased H_2 is associated with roughening of the Cu thin film catalyst due to increased Cu atom mobility during thermal processing, which can also lead to higher graphene nucleation

seed density, and (3) a H_2:CH_4 of 69:1 produces graphene with both the lowest $I_{D/G}$ = 0.04 (as-grown, transferred to SiO_2/Si) and the highest $I_{2D/G}$ = 2.3 within this study. GFETs were fabricated with this optimized graphene and achieved μ_{max} = 3,781 cm^2/V.s at a carrier density of $4x10^{12}$ carriers/cm^2. In contrast to C-plane sapphire supported Cu thin film graphene growth and due to weak adhesion between Cu thin films and SiO_2, optimization of graphene growth on SiO_2/Si support wafers was presented to be difficult and the resulting growth matrix of parameters is shrunk due to Cu thin film instabilities if wishing to attain $I_{D/G} < 0.1$ using this CC method. Additionally, once this is attained, the gaps between the Cu induce cracks once transferred with the method used in this work. The outcomes of this study will aid in improving the quality of graphene derived from Cu thin films using C-plane sapphire wafer supports. CC coupled with graphene growth on Cu (1 μm)/C-plane sapphire enables high-quality, wafer-scale graphene with consistent and predictable Cu (111) crystalline orientation and catalyst morphology.

3.2.4. Experimental Methods

We performed graphene growths on both SiO_2 and C-plane sapphire supports for comparison. We found one optimal growth recipe for SiO_2 supported Cu to both reduce $I_{D/G} < 0.1$ and maintain graphene uniformity as the growth conditions were limited by the stability of the Cu film due to the poor adhesion of Cu to SiO_2. For C-plane sapphire supported Cu, the array of growth conditions is much larger owing to the excellent adhesion of Cu to the C-plane sapphire. We first found the optimal growth temperature then varied the H_2:CH_4 flow ratios. Growth pressures ranged from 14.9 mbar to 19.4

mbar and growth temperature was held constant at 780°C. H_2 flow was varied from 690 sccm to 100 sccm while holding CH_4 flow constant at 10 sccm (lowest flow setting for MFC used on reactor). For all growths, the recipe profile was held constant (Figure 1). Catalyst confinement was achieved by a custom-fabricated quartz plate with alumina alignment pins and alumina spacers for adjusting the offset from the Cu thin film during the graphene growth process. All graphene growths use a 1.0 μm DC sputtered Cu film achieved with a base pressure of ~$6x10^{-9}$ Torr in a physical vapor deposition system.

Graphene Growth

A custom cold-wall reactor based upon the Aixtron BM Pro with capability of holding wafers up to a diameter of 50.8 mm was used for all graphene growths in this study. Supporting substrates were either SiO_2/Si wafers with 300nm of thermal oxide (NOVA Electronic Materials) or C-plane sapphire (Precision Micro-Optics). Supporting substrates were coated with 1 μm of Cu using a Kurt J. Lesker Axxis PVD system and DC magnetron sputtering. An as-deposited Cu thin film on supporting wafer (growth wafer) was then placed directly into the growth chamber and subsequently a quartz plate with alignment pins and alumina spacers was placed on top of the growth wafer. The growth chamber was then pumped down to base pressure (~10^{-3} mbar) with an automated growth recipe occurring directly afterwards with growth pressures ranging from 16.7-20.1 mbar. During a typical growth, ultra-high purity H_2 (99.999%) was injected into the growth chamber at the desired setpoint until a linear thermal ramp of the low-mass, carbon Joule heater had reached 780°C, then holding at this temperature for 3 mins. Next, ultra-high purity Ar and CH_4 were injected at 650 sccm and 10 sccm, respectively,

holding at growth temperature for 9.5 mins. Subsequently, all gas flows were closed and the heater was turned off and al-lowed to cool under vacuum. After sufficient cooling and pumping back to base pressure, the sample was further cooled under a 650 sccm flow of Ar. As-grown graphene wafers were then removed after at a heater temperature < 150°C.

Graphene Transfer

As-grown graphene wafers were first coated with two layers of PMMA solution (6% 995 kDa PMMA in anisole) by spin coating. The PMMA was then cured on purpose-built hotplates at 135°C for 3 mins. Next, thermal release tape was applied by hand with a thermal release transition at 150°C (Nitto REVALPHA). The thermal tape/PMMA/graphene stack was then separated by H_2 bubbling transfer similar to work by others[122]. This stack was rinsed and dried then placed onto the target wafer and placed between two ground aluminum plates compressed with a linear screw clamp. The clamp assembly was then placed into a vacuum oven pumped to base pressure (~10^{-2} mbar) and heated to 140°C for 1 hour. Afterwards the thermal tape/PMMA/graphene stack was bonded well to the target wafer. The wafer was then moved onto a pre-heated purpose-built hotplate and linearly ramped to 165°C. Once the hotplate reached the thermal release tape temperature, the tape was removed and the wafer was allowed to reach 165°C, then removed and allowed to cool to room temperature (RT). The remaining PMMA was removed with a RT bath of acetone for 3 hours.

Sample Characterization

As-grown graphene films on Cu and transferred graphene films were analyzed for quality and relative doping levels with a brightfield optical microscope and a Horiba HR800 Raman spectrometer equipped with a mapping stage. As-grown graphene films and the Cu film crystallographic orientation were analyzed with a Zeiss Sigma VP scanning electron equipped with an Oxford Nordlys electron backscatter diffraction (EBSD) detector. EBSD mapping was per-formed at 20 kV while graphene SEM imaging was per-formed at 5 kV.

Graphene Field Effect Transistor Fabrication

GFETS were fabricated using a Nanometer Pattern Generation System (NPGS) electron beam lithography (EBL) system installed onto a Zeiss Sigma VP SEM. Prior to patterning of graphene channels, the as-grown graphene was transferred onto degenerately doped Si wafers with 300 nm of thermal oxide. Metallization was achieved with a Kurt J. Lesker Axxis PVD system equipped with electron beam evaporation. Electrodes were fabricated with a serial deposition of 2.5 Å Ti, 20 nm Pd, and a 15 nm Au cap. Upon final lift-off, patterned devices wafers were placed into a Lakeshore vacuum probe station for measurement.

4. Spin Injection and Transport of Polarized Electrons in Graphene

Graphene has tremendous potential to unlock future spintronics applications due to its ability to transport spin current across long distances. However, the theorized spin coherence length has yet to be realized. This presents a major challenge for graphene spintronics as much of the field is not well understood. Additionally, the majority of studies, to-date, have focused on relatively wide channels and fundamental investigation of spin current scattering mechanisms. Another restriction of current graphene spin transport studies is the lack of statistics relating to device performance towards understanding device variations across a wafer, which are critical for implementation in industry. Here, we report a large array of graphene non-local spin valves (NLSVs) with widths varying from 3.0 μm down to 200 nm and lengths of 0.5 – 1.5 μm.

3.1. Introduction

In this study we address the fabrication of graphene spin transport channels using the traditional NLSV geometry both varying the channel width and length. Unlike previous studies, we fabricated and measured graphene NLSVs with channel widths as low as 200 nm with large change in non-local resistance (ΔR_{NL}) and a large signal-to-noise ratio (SNR). Additionally, we address spin transport measurements across a large array of devices with an unprecedented yield of 83% and provide spin transport statistics before and after an atmospheric oxidation treatment. Post-ambient exposure, we observe ΔR_{NL}% changes as high as 8800%. We also investigate the spin transport properties as a function of spin injection current with low noise down to 15 nA and up to 50 μA. The

spin signals at 300 K are then compared to those recorded at 4.2 K. This study utilizes NLSV spin device layouts with non-encapsulated graphene channels and in application, it is ideal if the spin transport channel can be encapsulated without degradation of spin properties. Since this study aims to determine fundamental spin properties for narrow GNRs, it is necessary to leave the graphene un-encapsulated. To demonstrate feasibility of application, encapsulation shall be needed as one of the addressable topics for graphene spintronics implementation.

4.2. Results and Discussion

The graphene NLSV array compromised of 40 devices, which exhibited connection between the source, drain, and two FM/TB contacts with 83% observed to be spin transport active. Therefore, there were 33 graphene NLSVs with observable ΔR_{NL} values using an in-plane magnetic sweep. All of the NLSVs can be divided into two groups, with one group as the narrow graphene nanoribbon (GNR) devices and the other group, wide GNR devices. Narrow NLSVs are defined as having W_{ch} = 200 and 400 nm, while the wide NLSVs include W_{ch} = 1.0, 2.0, and 3.0 μm. Among both the narrow and wide GNR NLSVs, the spin transport channel width, as defined by the center-to-center distance between the injector and detector FM/TB contacts, was varied with L_{ch} = 0.5, 1.0, and 1.5 μm. In the results that follow, we shall discuss the NLSV array performance of the graphene NLSVs prior to additional O_2 exposure (pre-ambient exposure), and discuss and evaluate the effect of the additional O_2 exposure (post-ambient exposure).

In this study, we opted to use Co FMs without an anti-oxidation cap and TiO_2 TBs, which are both deposited using electron beam evaporation (EBE). EBE was primarily selected for the deposition of the seed, Ti layer, which is eventually formed into TiO_2 using *in situ* O_2 post-deposition treatment. Metal Ti has a much larger affinity to graphene than TiO_2 due to the d-orbital mixing with the π bonds of graphene. This allows for the Ti layer to be deposited lacking large pinholes and with uniform thickness. In comparison to EBE, atomic layer deposition (ALD) currently lacks the ability for pinhole-free TiO_2 deposition and pure metal ALD is still in its infancy with few metals able to form high quality films. Several works have cited the importance of the interface between the FM/TB and graphene; therefore it is critical to use methods that result in the cleanest metal films. An alternative method would be to use molecular beam epitaxy (MBE), however, the process is presently cost-prohibitive to be considered for use within the semiconductor industry. Although costly, MBE is useful for fundamental studies as the films and crystals formed have far fewer defects than either EBE or ALD. Lastly, the FMs were left without a cap so that the effect of additional O_2 exposure could be observed. This is an important measurement because the TB is initially formed with a pure Ti seed layer. The oxidation of this seed layer determines the tunneling-like behavior of the interface, hence, it is critical to determine the relationship between unpolarized and polarized spin transport. One drawback is the Co may oxidize along with the Ti layer making it difficult to decouple the two effects and some forms of Co oxide are antiferromagnetic at room temperature. However, all measureable NSLVs post-

ambient exposure exhibited an increase in ΔR_{NL} therefore any effect of room temperature antiferromagnentism is most likely minimal.

The distribution of ΔR_{NL} values post-ambient exposure is depicted in Figure 4.1. Narrow GNRs occupied a much larger range of values than their wide GNR counterparts. Additionally, the peak ΔR_{NL} values for narrow GNRs are up to ~3 times larger than the wide GNR NLSVs.

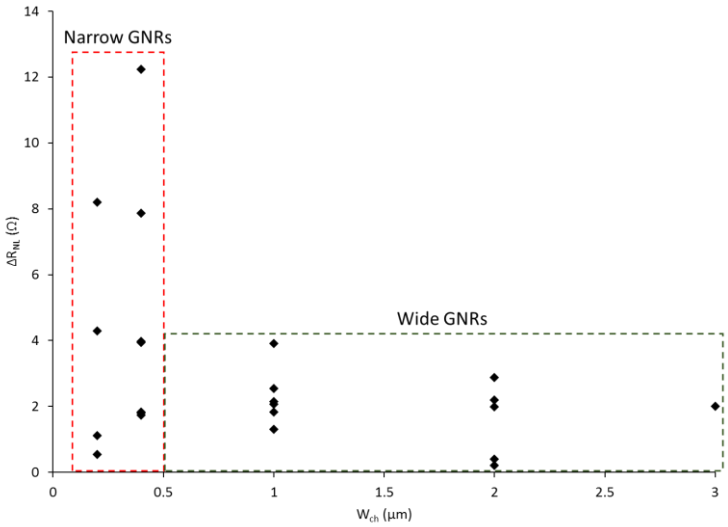

Figure 4.1. ΔR_{NL} vs. W_{ch} for an array of graphene non-local spin valves (NLSVs). Narrow NLSVs (200 and 400 nm widths) demonstrate larger ΔR_{NL} values than their wider counterparts.

There are a number of reasons that the narrow GNRs resulted in larger R_{NL} values including the much smaller contact area between the oxide TB layer and the GNR surface. It is possible that pinholes exist within the TiO_2 TB films and as the portion of the film responsible for tunneling becomes smaller, the likelihood of pinhole tunneling behavior decreases. To account for the larger range of ΔR_{NL} values, one can imagine that

besides a distribution of pinholes, the graphene surface may have some occasional residue left behind from the transfer and lithography processes. For the 200 nm and 400 nm wide GNRs used in the NLSVs, the area of overlap between the TBs and GNRs is $4x10^{-14}$ – $8x10^{-14}$ m^2 and $8x10^{-14}$ – $1.6x10^{-13}$ m^2, respectively. This very small area dominates the behavior of the injection and detection sides, which can be strongly influenced by any impurities and/or non-idealities present in the TB, GNR, or even overlaying Co FM.

Just as the smaller GNR NLSVs demonstrated a larger range of ΔR_{NL} values and ultimately the largest ΔR_{NL} values of the distribution, these same devices also presented the smallest change in ΔR_{NL} post-ambient exposure. Pre-ambient exposure, the narrow GNR NLSVs had larger R_{NL} values than the wide GNRs and, post-ambient exposure, ΔR_{NL} increased with a similar % change across the wide GNRs. The value of percent change increases dramatically for the wide GNRs with an average of 3564% ± 4927%, with a smaller average for the narrow GNRs of 1277% ± 2588%. In order to understand the distribution of the percent change in R_{NL} and correlate the magnitude of each to wide and narrow GNRs, it is important to revisit the TB/GNR overlap region. The wide GNRs range from 1 – 3 μm wide, which corresponds to overlap areas of $2x10^{-13}$ – $1.2x10^{-12}$ m^2. These overlap areas are 1-2 orders of magnitude larger than the narrow GNRs used. When comparing these overlap areas pre- and post-ambient exposure, it follows that with a larger contact area, the tunneling behavior will be influenced greater with an oxidation treatment since there is much more oxide in contact between the GNR and TB. The pre-

and post-ambient exposure ΔR_{NL} values in addition to the percent change can be seen in Figure 4.2, below. Devices 1-11 and 12-20 are wide and narrow GNRs, respectively.

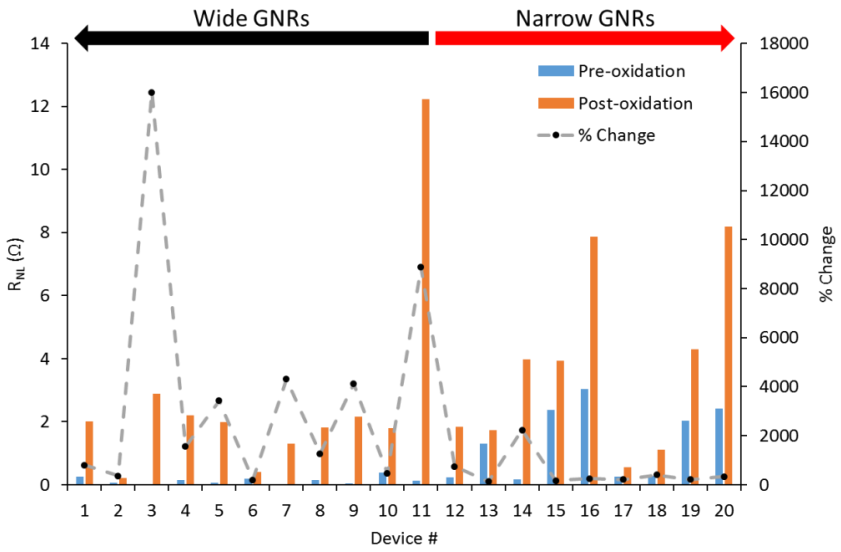

Figure 4.2. R_{NL} vs. device number for pre- and post-ambient exposure of the tunnel barrier contacts. R_{NL} is plotted against the left, vertical axis while the % change is plotted against the right, vertical axis. NLSVs with $W_{ch} \geq 1.0$ µm demonstrated the largest % change in R_{NL}.

In-plane magnetic sweeps of device 11, which demonstrated an 8800% change in ΔR_{NL}, is depicted in Figure 4.3a with both pre- and post-ambient exposure sweeps. In Figure 4.3b, the post-ambient exposure in-plane magnetic sweep is plotted separately to illustrate each component of the sweep. The RMS noise is similar for both measurements, however, the post-ambient exposure measurement has a dramatically increased signal intensity.

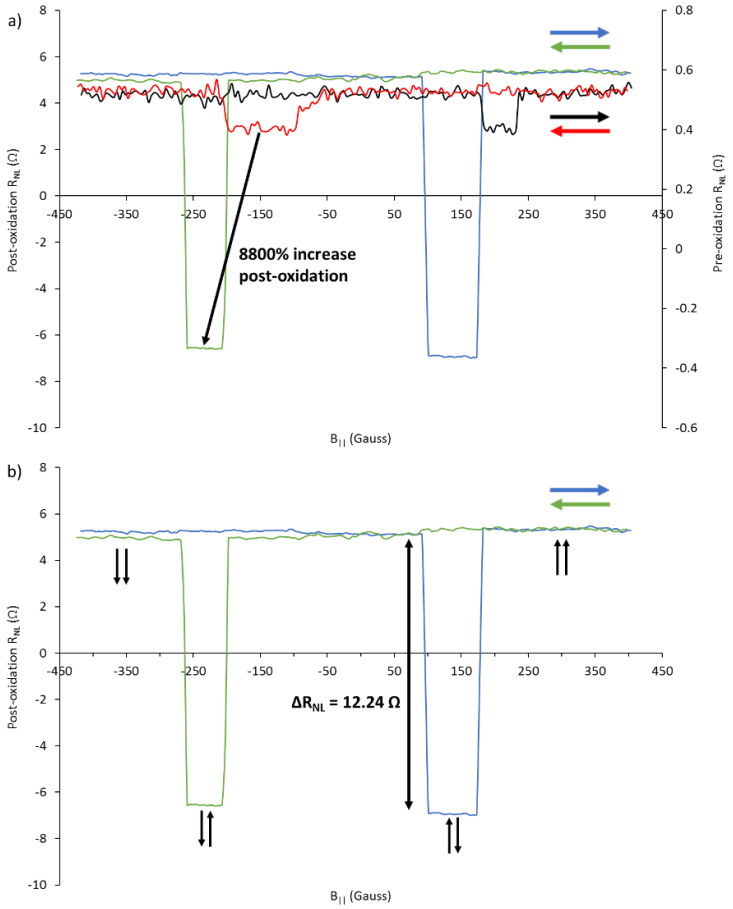

Figure 4.3. In-plane magnetic sweeps depicting before and after additional oxidation of FM/TB contacts. a) In-plane magnetic sweep for a selected device pre- and post-ambient exposure depicting an 8800% increase in ΔR_{NL}. The pre-ambient exposure sweep is in black/red and the post-ambient exposure sweep in green/blue. In addition to the large gain in ΔR_{NL}, the coercive forces of the magnets shifted post-ambient exposure. b) Post-ambient exposure, in-plane magnetic sweep depicting the nano-magnet configurations. In the forward sweep, both the injector and detector magnets are parallel until the magnetic field matches the coercive force of the larger magnet, which will switch first placing the magnets in an anti-parallel configuration. This results in the lowest voltage measurement. Soon afterwards, the magnetic field matches the coercive force of the smaller magnet and it will switch bringing the two magnets into an opposite parallel configuration. The reverse of this process occurs in the backward sweep direction.

In order to accurately determine the transport characteristics of the in-plane magnetic sweep measurements, out-of-plane Hanle precession measurements were

completed at atmospheric pressure through a collaboration at Intel Corp. and data analysis was carried out as part of the work in this dissertation. Using a magnetic prober with both in-plane and out-of-plane magnetic field, the FMs were first placed into either a parallel or antiparallel configuration and then switched into the Hanle, out-of-plane magnetic field sweep mode. The raw data output is pictured in Figure 3.4a with both the parallel and antiparallel plots overlaid. These raw data plots are then summed and placed into Python code generated by Sosenko et al.[88] and the output of the raw, summed data and overlaid best fit is depicted in Figure 4.4b for a NLSV with W_{ch} = 2 µm and L_{ch} = 2 µm so that dimensionality effects were avoided. Spin injection/detection efficiency is ≈ 6.6%, with a spin lifetime of $\tau \approx 135$ ps corresponding well to previous reports of NLSVs having pinhole oxide contacts between monolayer graphene and a FM, which have injection/detection efficiency, P, values of 2%-18%[17]. The spin diffusion length and diffusion constant were calculated to be $\lambda_s \approx 1.51$ µm and $D \approx 0.0169$ m^2/s these are both commensurate with other studies having similar GNR dimensions.

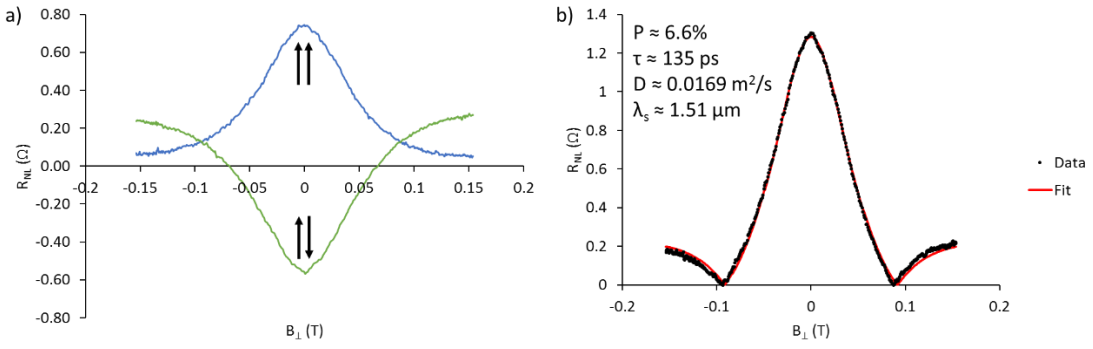

Figure 4.4. Hanle precession out-of-plane magnetic sweeps with data fitting. a) Raw out-of-plane magnetic sweeps for both the parallel and antiparallel state. b) Summed Hanle precession data fit to model for extraction of spin transport parameters using a method developed elsewhere[88]. For data fitting, $\chi^2 = 0.208$.

With the narrow GNRs, both the pre- and post-ambient exposure values were larger than the wide GNR NLSVs and demonstrated the smallest percent change in measured ΔR_{NL} values. With equal channel lengths, the narrow GNR NLSVs show more predictable behavior and overall, larger ΔR_{NL} values, which demonstrates an advantage for integration of graphene spin interconnects as they exhibit improvement in spin signal as the GNR width decreases. For interconnects in proposed, future spintronics technology, the ability to produce both long and narrow channels is desired[123]. Here, we find that narrow GNRs aid in the production of superior NLSVs and demonstrate only ≈36% of the wide GNR post-ambient exposure change. It is likely the oxidation of TBs after exposure to ambient for narrow GNRs was closer to a saturated, oxidized state and the oxidation rate of TBs corresponding to wider GNRs occurred at a lower rate. This also lends advantage towards scaling down graphene spin interconnects as they are less susceptible to environmental oxidation. Post-ambient exposure in-plane magnetic sweeps of narrow GNR NLSVs with W_{ch} = 200, 400 nm, and L_{ch} = 0.5, 1.5 μm are depicted in Figure 4.5.

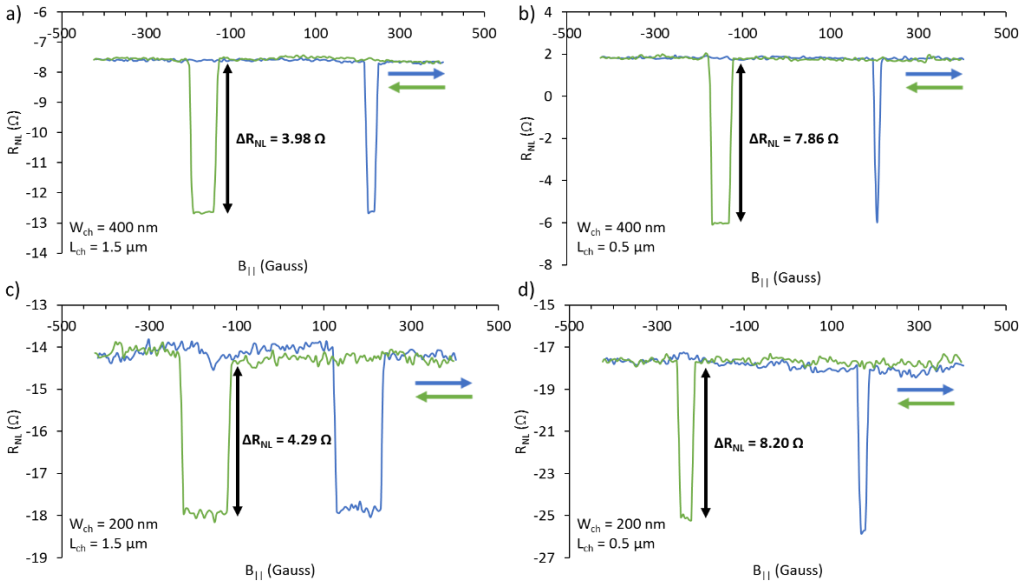

Figure 4.5. In-plane magnetic sweeps for selected narrow GNR NLSVs. For equivalent transport distances, the 200 nm wide GNRs have larger ΔR_{NL} values accompanied by increased noise.

Comparing both the 200 and 400 nm wide GNR NLSVs with L_{ch} = 1.5 µm, it can be seen the ΔR_{NL} value of the 200 nm wide NLSV is ≈7.8% larger, and a similar increase is observed with a ≈4.3% increase in ΔR_{NL} at W_{ch} = 0.5 µm. Bar charts depicting this comparison in ΔR_{NL} are illustrated in Figure 4.6. Further demonstrating the superiority of narrow channel NSLVs, the average percent change of the 200 nm GNRs post-ambient exposure was measured to be only ≈15.8% (290.6% ± 94.4%) of the post-ambient exposure change in ΔR_{NL} measured for 400 nm GNR NLSVs (1840.8% ± 3184.5%) with a correspondingly lower standard deviation. Overall, when compared to the average percent change of both the wide and 400 nm GNRs, the 200 nm GNR NLSVs had only ≈13.0% relative post-ambient exposure change in ΔR_{NL}.

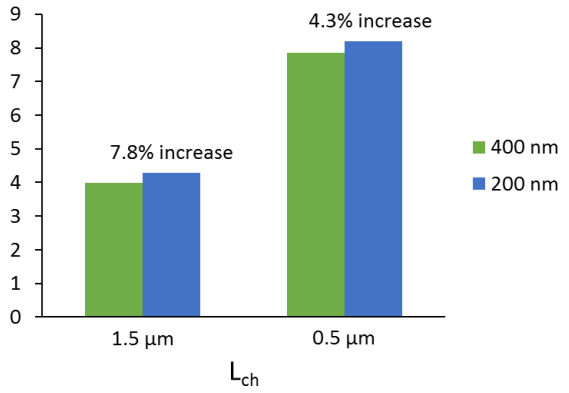

Figure 4.6. Bar chart demonstrating the difference in ΔR_{NL} values for both narrow GNR NLSVs. A larger difference in ΔR_{NL} is observed with increasing spin transport channel distance.

To explore beyond the ambient exposure experiments affecting ΔR_{NL} and DC characteristics, the tunneling-like characteristics of the injector/detector contacts were measured by varying the charge carrier density and measuring the resulting ΔR_{NL} values. Drift-diffusion theory predicts that intermediate contacts, where the contact resistance between the FM and graphene and the graphene resistance are similar, will have a minimum value at the Dirac point and increase nearby the Dirac point, gradually turning over to lesser ΔR_{NL} values[17]. As seen in Figure 4.7a and 4.7b, ΔR_{NL} decreases rapidly while V_{BG} approaches V_{Dirac}. This data matches well with the prediction of pinhole tunneling behavior from the Hanle sweep data, however, as depicted in Figure 4.7c, the NLSV with the shortest transport distance of 0.5 µm demonstrated a maximum ΔR_{NL} at V_{Dirac} suggesting stricter tunneling behavior where ΔR_{NL} varies with $1/\sigma_G$. However, the maximum ΔR_{NL} is not significant as it within 1σ of the population.

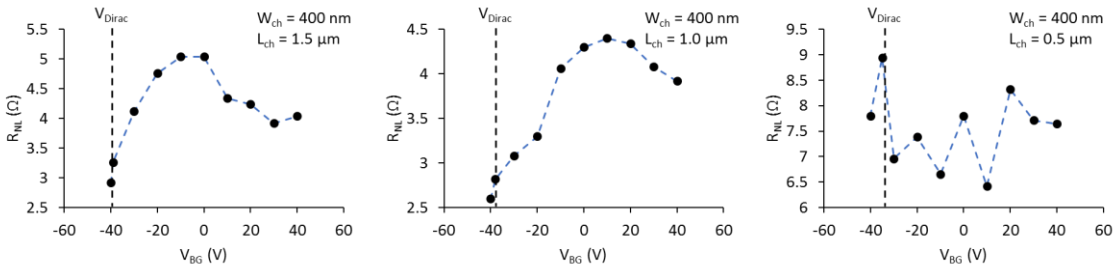

Figure 4.7. Dependence of ΔR_{NL} on backgate voltage, V_{BG}, and spin transport distance. ΔR_{NL} is minimized at V_{Dirac} with a maximum value near V_{BG} = 0 V. The relationship breaks down for the shortest transport distance of 0.5 µm where dimensionality effects may mitigate the effects of a modulated V_{BG}, and hence carrier density. However, drift-diffusion theory predicts a local maximum at V_{Dirac} for tunneling behavior and may suggest variability in the injector/detector contacts.

Interestingly, the devices with intermediate behavior both exhibited local maxima at V_{BG} ≈ 0 V. The asymmetry of these curves is not well-understood and variance in devices leads to issues with correlation to the tunnel barrier contact performance.

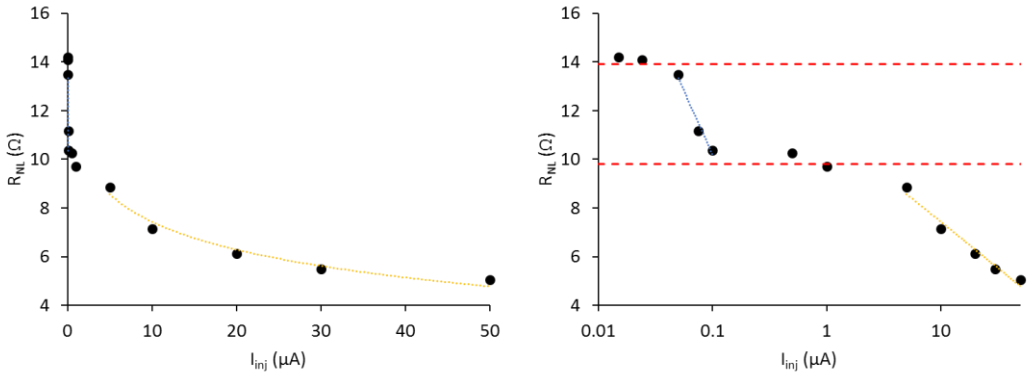

Figure 4.8. Dependence of ΔR_{NL} on injection current magnitude. a) ΔR_{NL} approaches a maximum value as I_{inj} is decreased until the signal is lost in the noise floor. As I_{inj} increases, ΔR_{NL} decreases logarithmically. b) A semi-log plot demonstrating the different current threshold levels which result in an ΔR_{NL} change.

To determine the effect of injection current on ΔR_{NL}, I_{inj} was increased gradually from 15 nA to 50 µA with five in-plane magnetic sweeps occurring at each I_{inj} to

determine the average ΔR_{NL} value. ΔR_{NL} is a maximum value at the minimum I_{inj} (15 nA) with a measureable spin signal and decreases logarithmically as depicted in Figure 4.8a. When the same data is presented on a semi-log plot, as in Figure 4.8b, it becomes apparent there are two regions where ΔR_{NL} is invariant with I_{inj}.

4.3. Conclusions

In conclusion, we have demonstrated enhanced ΔR_{NL} for nano-scale GNR widths down to 200 nm with better stability to environmental conditions that may cause changes to tunnel barrier resistance and spin signal magnitude. These NLSVs have the narrowest graphene channel width yet reported in literature. NLSVs were fabricated with monolayer graphene grown using a scalable t-CVD process, which utilizes Cu thin films for a catalytic growth surface instead of the typical Cu foil-based as-grown based graphene NLSV arrays. In order to assess the effect of tunnel barrier oxidation time the as-fabricated NLSV arrays were first subjected to a controlled *in situ* oxidation then further oxidized in ambient atmosphere. The oxidation effects elucidated the impact of oxidation time with the GNR width by demonstrating the lowest ΔR_{NL} variability pre- and post-ambient exposure for 200 nm wide GNRs. Spin transport parameters such as D_s, τ_s, were extracted and λ_s calculated from Hanle precession measurements and are comparable to intermediate, pinhole tunnel barrier contacts as expected from the method used for tunnel barrier fabrication. This behavior was confirmed by measuring the effect of carrier density on ΔR_{NL} where most devices demonstrated intermediate behavior with few exhibiting purely tunneling curves. This work assists in adding to our fundamental

understanding of spin transport in narrow graphene channels. Next steps in the field of narrow spin interconnects may involve further reducing the width of the GNR to elucidate effect such as quantum confinement and optical response. These applications require more rigorous development for graphene growth and associated lithography processes for achieving sub-10 nm GNR widths for quantum confinement and associated desirable characteristics that allow tuning of spin transport in graphene.

4.4. Experimental Methods

Graphene NLSV Array Fabrication

CVD graphene was grown in-house and then transferred according to methods described by the previous section. A collaborator at Intel Corp. then processed the transferred graphene samples for fabrication of GNR devices with source and drain contacts. Upon electrical measurement pre-screening of as-fabricated arrays, another lithography process was completed by a collaborator at Intel Corp. used to define the FM/TB contacts. After resist development, the patterned array was taken back to Portland State University and placed into a Lesker AXXISS physical vapor deposition (PVD) system for electron beam evaporation (EBE) of TiO_2 TB contacts by a two stage deposition process of 4 Å Ti separated by *in situ* O_2 treatment at 100 mbar. Next, a 35 nm layer of Co was deposited and directly afterwards the sample was removed from vacuum and placed into high purity acetone for liftoff. Then the sample was placed into the magnetic probe station at vacuum after sufficient rinsing and drying, post-liftoff.

Sample Characterization

NLSV arrays were characterized electronically within an in-plane magnetic field cryoprober manufactured by Lakeshore Cryotronics. Current-voltage DC characteristics were extracted using an Agilent B1500A semiconductor parameter analyzer (SPA) and the spin signals were measured using an in-house program developed with LabVIEW, which allowed sweeping of the magnetic field while measuring the non-local voltage using an SRS SR850 DSP lock-in amplifier. Current was supplied to the injector of each NLSV through a 1 MΩ ballast resistor driven by the sine output of the lock-in amplifier.

5. Summary and Outlook

Graphene spintronics cannot be realized without graphene manufacture and there are still major challenges that exist for enabling consistent, high-quality, and wafer-scale graphene. Although graphene was first isolated in 2004, it took 4 more years to realize CVD of monolayer graphene and presently, 8 years later, it still remains a topic for research and development. The superlatives surrounding graphene are primarily representative of single crystal analogs and to-date, no wafer-scale synthesis method of single crystal CVD graphene has been discovered. Therefore, the field of graphene spintronics concerned with large-area graphene spintronics is currently limited to polycrystalline graphene. This type of graphene is difficult to handle as it is only as strong as its weakest bond and easily cracks during transfer. Consequently, in this dissertation, there was a major effort for CVD of graphene using three methods and Cu thin films: 1) t-CVD of graphene on SiO_2/Si wafers, 2) low-temperature ICPCVD of graphene on SiO_2/Si wafers, and 3) t-CVD of graphene on C-plane sapphire wafers. Although challenges remain, this work elucidated the detailed mechanisms of graphene growth and utilization of several transfer techniques.

Regarding graphene growth, future work shall involve two paths; one path for t-CVD and another for remote plasma CVD. T-CVD may grow graphene at relatively high temperatures, however, this is not an issue if the as-grown graphene is to be transferred for utilization at the target substrate. Therefore, an effort should remain to improve t-CVD routes. One promising route that was outlined in this work is catalyst confinement (CC). This method has been pursued by others and generally, a shift in the published

literature indicates this method is being adopted on a larger scale than was previously observed. By using CC, many issues with graphene growth are mitigated including reduction of Cu evaporative losses, lack of Cu deposition within the reactor, decreased graphene nucleation density, and lack of turbulent gas flows due to the restricted volume between the catalyst and the confinement structure. Although the method of confinement may appear to have solved all issues, it has a major drawback yet to be solved which is the gas delivery gradient that evolves due the confinement structure (a quartz plate in this work) having dimensions on the order of the growth wafer. Computer modeling accompanied with experimentation must be employed to improve the uniformity of gas delivery with such a process while maintaining the demonstrated advantages.

The next path for t-CVD is to reduce the graphene nucleation density towards single crystal graphene and controllable bilayer growth processes. A recent study by Xu et al. demonstrated ultrafast single crystal graphene growth and found the largest graphene crystals in the confined space between an oxide substrate carrier and Cu foil[52]. Although this study advances the field of graphene t-CVD, it still relies on foil as a catalyst substrate and the single crystal graphene domains extend up to 0.3 mm. Therefore, a next, logical step would be to employ the knowledge gained from this study and couple it to wafer-scale growth of graphene *via* similar processes. In fact, the vast majority of graphene studies still rely on Cu foil CVD graphene due to its relative maturity compared to metal catalyst thin film CVD graphene. Additionally, typical Cu foil used for CVD graphene is 25 μm thick and is unlikely to be completely evaporated during graphene synthesis whereas metal catalyst thin films can be unstable at high growth temperatures

when using Cu. In order to improve the stability of the Cu catalyst film, a method presented in this dissertation was utilization of a C-plane sapphire support wafer with CC. Cu has dramatically improved adhesion to C-plane sapphire compared to SiO_2/Si wafers and allows for improved robustness of the Cu film at the t-CVD graphene growth temperatures required for high-quality graphene growth in addition to providing a smooth Cu growth substrate with millimeter-scale crystal domains.

Upon successful CVD process development, transferring the as-grown graphene for development of NLSV arrays assumes the aforementioned processes are capable of delivering high-quality graphene, which means the graphene is uniform with a low defect density and large graphene domains. The NLSV is chosen as a development tool for investigation of graphene as a spin transport material for lateral spintronics since the majority of spin parameters can be extracted using just one device configuration while the test setup is varied. Graphene is a promising candidate for development of spintronics largely due to its weak SOC, allowing spin current to theoretically traverse graphene channels practically undisturbed at room temperature. Realistically, the field of graphene spintronics has demonstrated the large spin lifetimes and diffusion lengths predicted for graphene have yet to be realized and an effort to describe the underlying scattering mechanisms is underway. Resonant scattering[70] currently comes closest to the experimental spin transport characteristics measured for graphene and an increasing number of studies continue to be published regarding the poorly understood spin scattering mechanisms.

The work in this dissertation seeks to bridge CVD graphene derived from thin film growth methods into wafer-scale application of spin devices. The results are promising with 83% spin yield and demonstrated spin transport using GNRs that are 200 nm wide. We investigated spin transport across large NLSV arrays and explored the effects of post-ambient exposure. Narrow GNRs were not only more stable post-ambient exposure due to smaller TB-GNR overlap, they also exhibited the largest, measured R_{NL} values. We also explored the differences between electron beam evaporated, Al_2O_3 and TiO_2 metal-seeded TBs grown with *in situ* oxidation with improved performance observed with TiO_2. It was hypothesized the *p-d* surface-induced hybridization between Ti and graphene improve adhesion of the metal seed layer thereby providing a better TB interface.

The next milestone for graphene spintronics is to increase the SOC of graphene and make it magnetic. A recent study utilized the proximity effect to induce ferromagnetism in graphene while improving SOC[124]. A 20 nm thick layer of yttrium iron garnet (YIG) was grown on 0.5 nm gadolinium gallium garnet (GGG) films using pulsed laser deposition. Although this study uses expensive techniques and exotic materials, it was able to demonstrate the power of proximity-induced effects in graphene and the anomalous Hall effect (AHE). It was also hypothesized that in order to observe the quantum AHE (QAHE), it is necessary to enhance the Rashba SOC to a level beyond the disorder energy scale, and enhanced Rashba SOC has been demonstrated by others attributed to broken inversion symmetry[59]. Connecting the two components may yield an observed QAHE. Regarding the application of spintronics, this also opens up many more

possibilities for graphene-based spin logic as tunable magnetic and SOC properties have been demonstrated as feasible options.

References

(1) Lee, C.; Wei, X.; Kysar, J. W.; Hone, J. Measurement of the Elastic Properties and Intrinsic Strength of Monolayer Graphene. *Science* **2008**, *321*, 385–388.

(2) Geim, A. K. Graphene: Status and Prospects. *Science* **2009**, *324*, 1530–1534.

(3) Bolotin, K. I.; Sikes, K. J.; Jiang, Z.; Klima, M.; Fudenberg, G.; Hone, J.; Kim, P.; Stormer, H. L. Ultrahigh Electron Mobility in Suspended Graphene. *Solid State Commun.* **2008**, *146*, 351–355.

(4) Avsar, A.; Tan, J. Y.; Taychatanapat, T.; Balakrishnan, J.; Koon, G. K. W.; Yeo, Y.; Lahiri, J.; Carvalho, A.; Rodin, A. S.; O'Farrell, E. C. T.; *et al.* Spin–orbit Proximity Effect in Graphene. *Nat. Commun.* **2014**, *5*, 4875.

(5) Fu, L.; Kane, C. L. Superconducting Proximity Effect and Majorana Fermions at the Surface of a Topological Insulator. *Phys. Rev. Lett.* **2008**, *100*, 096407.

(6) Qiao, Z.; Ren, W.; Chen, H.; Bellaiche, L.; Zhang, Z.; MacDonald, A. H.; Niu, Q. Quantum Anomalous Hall Effect in Graphene Proximity Coupled to an Antiferromagnetic Insulator. *Phys. Rev. Lett.* **2014**, *112*, 116404.

(7) Shailos, A.; Nativel, W.; Kasumov, A.; Collet, C.; Ferrier, M.; Guéron, S.; Deblock, R.; Bouchiat, H. Proximity Effect and Multiple Andreev Reflections in Few-Layer Graphene. *EPL Europhys. Lett.* **2007**, *79*, 57008.

(8) Huertas-Hernando, D.; Guinea, F.; Brataas, A. Spin-Orbit Coupling in Curved Graphene, Fullerenes, Nanotubes, and Nanotube Caps. *Phys. Rev. B* **2006**, *74*, 155426.

(9) Ertler, C.; Konschuh, S.; Gmitra, M.; Fabian, J. Electron Spin Relaxation in Graphene: The Role of the Substrate. *Phys. Rev. B* **2009**, *80*, 041405.

(10) Maassen, T.; van den Berg, J. J.; IJbema, N.; Fromm, F.; Seyller, T.; Yakimova, R.; van Wees, B. J. Long Spin Relaxation Times in Wafer Scale Epitaxial Graphene on SiC(0001). *Nano Lett.* **2012**, *12*, 1498–1502.

(11) Pedersen, T. G.; Flindt, C.; Pedersen, J.; Mortensen, N. A.; Jauho, A.-P.; Pedersen, K. Graphene Antidot Lattices: Designed Defects and Spin Qubits. *Phys. Rev. Lett.* **2008**, *100*, 136804.

(12) Xia, F.; Wang, H.; Xiao, D.; Dubey, M.; Ramasubramaniam, A. Two-Dimensional Material Nanophotonics. *Nat. Photonics* **2014**, *8*, 899–907.

(13) Gmitra, M.; Fabian, J. Graphene on Transition-Metal Dichalcogenides: A Platform for Proximity Spin-Orbit Physics and Optospintronics. *Phys. Rev. B* **2015**, *92*, 155403.

(14) Myoung, N.; Seo, K.; Lee, S. J.; Ihm, G. Large Current Modulation and Spin-Dependent Tunneling of Vertical Graphene/MoS2 Heterostructures. *ACS Nano* **2013**, *7*, 7021–7027.

(15) Irmer, S.; Frank, T.; Putz, S.; Gmitra, M.; Kochan, D.; Fabian, J. Spin-Orbit Coupling in Fluorinated Graphene. *Phys. Rev. B* **2015**, *91*, 115141.

(16) Tombros, N.; Jozsa, C.; Popinciuc, M.; Jonkman, H. T.; van Wees, B. J. Electronic Spin Transport and Spin Precession in Single Graphene Layers at Room Temperature. *Nature* **2007**, *448*, 571–574.

(17) Han, W.; Pi, K.; McCreary, K. M.; Li, Y.; Wong, J. J. I.; Swartz, A. G.; Kawakami, R. K. Tunneling Spin Injection into Single Layer Graphene. *Phys. Rev. Lett.* **2010**, *105*, 167202.
(18) Chen, J.-R.; Odenthal, P. M.; Swartz, A. G.; Floyd, G. C.; Wen, H.; Luo, K. Y.; Kawakami, R. K. Control of Schottky Barriers in Single Layer MoS2 Transistors with Ferromagnetic Contacts. *Nano Lett.* **2013**, *13*, 3106–3110.
(19) Drögeler, M.; Volmer, F.; Wolter, M.; Terrés, B.; Watanabe, K.; Taniguchi, T.; Güntherodt, G.; Stampfer, C.; Beschoten, B. Nanosecond Spin Lifetimes in Single- and Few-Layer Graphene–hBN Heterostructures at Room Temperature. *Nano Lett.* **2014**, *14*, 6050–6055.
(20) McCreary, K. M.; Pi, K.; Kawakami, R. K. Metallic and Insulating Adsorbates on Graphene. *Appl. Phys. Lett.* **2011**, *98*, 192101.
(21) Zomer, P. J.; Guimarães, M. H. D.; Tombros, N.; van Wees, B. J. Long-Distance Spin Transport in High-Mobility Graphene on Hexagonal Boron Nitride. *Phys. Rev. B* **2012**, *86*, 161416.
(22) Yamaguchi, T.; Masubuchi, S.; Iguchi, K.; Moriya, R.; Machida, T. Tunnel Spin Injection into Graphene Using Al2O3 Barrier Grown by Atomic Layer Deposition on Functionalized Graphene Surface. *J. Magn. Magn. Mater.* **2012**, *324*, 849–852.
(23) Yamaguchi, T.; Inoue, Y.; Masubuchi, S.; Morikawa, S.; Onuki, M.; Watanabe, K.; Taniguchi, T.; Moriya, R.; Machida, T. Electrical Spin Injection into Graphene through Monolayer Hexagonal Boron Nitride. *Appl. Phys. Express* **2013**, *6*, 073001.
(24) Kamalakar, M. V.; Dankert, A.; Kelly, P. J.; Dash, S. P. Inversion of Spin Signal and Spin Filtering in Ferromagnet|Hexagonal Boron Nitride-Graphene van Der Waals Heterostructures. *Sci. Rep.* **2016**, *6*, 21168.
(25) Friedman, A. L.; van 't Erve, O. M. J.; Li, C. H.; Robinson, J. T.; Jonker, B. T. Homoepitaxial Tunnel Barriers with Functionalized Graphene-on-Graphene for Charge and Spin Transport. *Nat. Commun.* **2014**, *5*, 3161.
(26) Friedman, A. L.; Erve, O. M. J. van 't; Robinson, J. T.; Jr, K. E. W.; Jonker, B. T. Homoepitaxial Graphene Tunnel Barriers for Spin Transport. *AIP Adv.* **2016**, *6*, 056301.
(27) Kamalakar, M. V.; Dankert, A.; Bergsten, J.; Ive, T.; Dash, S. P. Enhanced Tunnel Spin Injection into Graphene Using Chemical Vapor Deposited Hexagonal Boron Nitride. *Sci. Rep.* **2014**, *4*, 6146.
(28) Kamalakar, M. V.; Groenveld, C.; Dankert, A.; Dash, S. P. Long Distance Spin Communication in Chemical Vapour Deposited Graphene. *Nat. Commun.* **2015**, *6*, 6766.
(29) Heerema, S. J.; Dekker, C. Graphene Nanodevices for DNA Sequencing. *Nat. Nanotechnol.* **2016**, *11*, 127–136.
(30) Kralj, M. Graphene Spintronics: Intercalated Boosters. *Nat. Phys.* **2015**, *11*, 11–12.
(31) Aghigh, A.; Alizadeh, V.; Wong, H. Y.; Islam, M. S.; Amin, N.; Zaman, M. Recent Advances in Utilization of Graphene for Filtration and Desalination of Water: A Review. *Desalination* **2015**, *365*, 389–397.

(32) Fang, Q.; Shen, Y.; Chen, B. Synthesis, Decoration and Properties of Three-Dimensional Graphene-Based Macrostructures: A Review. *Chem. Eng. J.* **2015**, *264*, 753–771.
(33) Raccichini, R.; Varzi, A.; Passerini, S.; Scrosati, B. The Role of Graphene for Electrochemical Energy Storage. *Nat. Mater.* **2015**, *14*, 271–279.
(34) Novoselov, K. S.; Geim, A. K.; Morozov, S. V.; Jiang, D.; Zhang, Y.; Dubonos, S. V.; Grigorieva, I. V.; Firsov, A. A. Electric Field Effect in Atomically Thin Carbon Films. *Science* **2004**, *306*, 666–669.
(35) Yu, Q.; Lian, J.; Siriponglert, S.; Li, H.; Chen, Y. P.; Pei, S.-S. Graphene Segregated on Ni Surfaces and Transferred to Insulators. *Appl. Phys. Lett.* **2008**, *93*, 113103.
(36) Chu, J. H.; Kwak, J.; Kwon, T.-Y.; Park, S.-D.; Go, H.; Kim, S. Y.; Park, K.; Kang, S.; Kwon, S.-Y. Facile Synthesis of Few-Layer Graphene with a Controllable Thickness Using Rapid Thermal Annealing. *ACS Appl. Mater. Interfaces* **2012**, *4*, 1777–1782.
(37) Li, X.; Cai, W.; An, J.; Kim, S.; Nah, J.; Yang, D.; Piner, R.; Velamakanni, A.; Jung, I.; Tutuc, E.; *et al.* Large-Area Synthesis of High-Quality and Uniform Graphene Films on Copper Foils. *Science* **2009**, *324*, 1312–1314.
(38) Han, G. H.; Güneş, F.; Bae, J. J.; Kim, E. S.; Chae, S. J.; Shin, H.-J.; Choi, J.-Y.; Pribat, D.; Lee, Y. H. Influence of Copper Morphology in Forming Nucleation Seeds for Graphene Growth. *Nano Lett.* **2011**, *11*, 4144–4148.
(39) Wassei, J. K.; Mecklenburg, M.; Torres, J. A.; Fowler, J. D.; Regan, B. C.; Kaner, R. B.; Weiller, B. H. Chemical Vapor Deposition of Graphene on Copper from Methane, Ethane and Propane: Evidence for Bilayer Selectivity. *Small* **2012**, *8*, 1415–1422.
(40) Ito, Y.; Christodoulou, C.; Nardi, M. V.; Koch, N.; Sachdev, H.; Müllen, K. Chemical Vapor Deposition of N-Doped Graphene and Carbon Films: The Role of Precursors and Gas Phase. *ACS Nano* **2014**, *8*, 3337–3346.
(41) Zhang, Y.; Li, Z.; Kim, P.; Zhang, L.; Zhou, C. Anisotropic Hydrogen Etching of Chemical Vapor Deposited Graphene. *ACS Nano* **2012**, *6*, 126–132.
(42) Tao, L.; Lee, J.; Chou, H.; Holt, M.; Ruoff, R. S.; Akinwande, D. Synthesis of High Quality Monolayer Graphene at Reduced Temperature on Hydrogen-Enriched Evaporated Copper (111) Films. *ACS Nano* **2012**, *6*, 2319–2325.
(43) Ago, H.; Ohta, Y.; Hibino, H.; Yoshimura, D.; Takizawa, R.; Uchida, Y.; Tsuji, M.; Okajima, T.; Mitani, H.; Mizuno, S. Growth Dynamics of Single-Layer Graphene on Epitaxial Cu Surfaces. *Chem. Mater.* **2015**, *27*, 5377–5385.
(44) Song, Y.; Pan, D.; Cheng, Y.; Wang, P.; Zhao, P.; Wang, H. Growth of Large Graphene Single Crystal inside a Restricted Chamber by Chemical Vapor Deposition. *Carbon* **2015**, *95*, 1027–1032.
(45) Zhao, L.; Rim, K. T.; Zhou, H.; He, R.; Heinz, T. F.; Pinczuk, A.; Flynn, G. W.; Pasupathy, A. N. Influence of Copper Crystal Surface on the CVD Growth of Large Area Monolayer Graphene. *Solid State Commun.* **2011**, *151*, 509–513.

(46) Tao, L.; Lee, J.; Chou, H.; Holt, M.; Ruoff, R. S.; Akinwande, D. Synthesis of High Quality Monolayer Graphene at Reduced Temperature on Hydrogen-Enriched Evaporated Copper (111) Films. *ACS Nano* **2012**, *6*, 2319–2325.
(47) Tao, L.; Lee, J.; Holt, M.; Chou, H.; McDonnell, S. J.; Ferrer, D. A.; Babenco, M. G.; Wallace, R. M.; Banerjee, S. K.; Ruoff, R. S.; *et al.* Uniform Wafer-Scale Chemical Vapor Deposition of Graphene on Evaporated Cu (111) Film with Quality Comparable to Exfoliated Monolayer. *J. Phys. Chem. C* **2012**, *116*, 24068–24074.
(48) Yu, H. K.; Balasubramanian, K.; Kim, K.; Lee, J.-L.; Maiti, M.; Ropers, C.; Krieg, J.; Kern, K.; Wodtke, A. M. Chemical Vapor Deposition of Graphene on a "Peeled-Off" Epitaxial Cu(111) Foil: A Simple Approach to Improved Properties. *ACS Nano* **2014**, *8*, 8636–8643.
(49) Gao, L.; Guest, J. R.; Guisinger, N. P. Epitaxial Graphene on Cu(111). *Nano Lett.* **2010**, *10*, 3512–3516.
(50) Guimarães, M. H. D.; Veligura, A.; Zomer, P. J.; Maassen, T.; Vera-Marun, I. J.; Tombros, N.; van Wees, B. J. Spin Transport in High-Quality Suspended Graphene Devices. *Nano Lett.* **2012**, *12*, 3512–3517.
(51) Popinciuc, M.; Józsa, C.; Zomer, P. J.; Tombros, N.; Veligura, A.; Jonkman, H. T.; van Wees, B. J. Electronic Spin Transport in Graphene Field-Effect Transistors. *Phys. Rev. B* **2009**, *80*, 214427.
(52) Xu, X.; Zhang, Z.; Qiu, L.; Zhuang, J.; Zhang, L.; Wang, H.; Liao, C.; Song, H.; Qiao, R.; Gao, P.; *et al.* Ultrafast Growth of Single-Crystal Graphene Assisted by a Continuous Oxygen Supply. *Nat. Nanotechnol.* **2016**, *advance online publication*.
(53) Hao, Y.; Wang, L.; Liu, Y.; Chen, H.; Wang, X.; Tan, C.; Nie, S.; Suk, J. W.; Jiang, T.; Liang, T.; *et al.* Oxygen-Activated Growth and Bandgap Tunability of Large Single-Crystal Bilayer Graphene. *Nat. Nanotechnol.* **2016**, *11*, 426–431.
(54) Miseikis, V.; Convertino, D.; Mishra, N.; Gemmi, M.; Mashoff, T.; Heun, S.; Haghighian, N.; Bisio, F.; Canepa, M.; Piazza, V.; *et al.* Rapid CVD Growth of Millimetre-Sized Single Crystal Graphene Using a Cold-Wall Reactor. *2D Mater.* **2015**, *2*, 014006.
(55) Li, J.; Wang, X.-Y.; Liu, X.-R.; Jin, Z.; Wang, D.; Wan, L.-J. Facile Growth of Centimeter-Sized Single-Crystal Graphene on Copper Foil at Atmospheric Pressure. *J Mater Chem C* **2015**, *3*, 3530–3535.
(56) Gurram, M.; Omar, S.; Zihlmann, S.; Makk, P.; Schönenberger, C.; van Wees, B. J. Spin Transport in Fully Hexagonal Boron Nitride Encapsulated Graphene. *Phys. Rev. B* **2016**, *93*, 115441.
(57) Shi, Y.; Hamsen, C.; Jia, X.; Kim, K. K.; Reina, A.; Hofmann, M.; Hsu, A. L.; Zhang, K.; Li, H.; Juang, Z.-Y.; *et al.* Synthesis of Few-Layer Hexagonal Boron Nitride Thin Film by Chemical Vapor Deposition. *Nano Lett.* **2010**, *10*, 4134–4139.
(58) Kim, K. K.; Hsu, A.; Jia, X.; Kim, S. M.; Shi, Y.; Hofmann, M.; Nezich, D.; Rodriguez-Nieva, J. F.; Dresselhaus, M.; Palacios, T.; *et al.* Synthesis of Monolayer Hexagonal Boron Nitride on Cu Foil Using Chemical Vapor Deposition. *Nano Lett.* **2012**, *12*, 161–166.

(59) Balakrishnan, J.; Kok Wai Koon, G.; Jaiswal, M.; Castro Neto, A. H.; Özyilmaz, B. Colossal Enhancement of Spin-Orbit Coupling in Weakly Hydrogenated Graphene. *Nat. Phys.* **2013**, *9*, 284–287.
(60) Gmitra, M.; Kochan, D.; Fabian, J. Spin-Orbit Coupling in Hydrogenated Graphene. *Phys. Rev. Lett.* **2013**, *110*, 246602.
(61) Nair, R. R.; Sepioni, M.; Tsai, I.-L.; Lehtinen, O.; Keinonen, J.; Krasheninnikov, A. V.; Thomson, T.; Geim, A. K.; Grigorieva, I. V. Spin-Half Paramagnetism in Graphene Induced by Point Defects. *Nat. Phys.* **2012**, *8*, 199–202.
(62) Santos, E. J. G.; Ayuela, A.; Sánchez-Portal, D. Universal Magnetic Properties of Sp 3 -Type Defects in Covalently Functionalized Graphene. *New J. Phys.* **2012**, *14*, 043022.
(63) Zollner, K.; Frank, T.; Irmer, S.; Gmitra, M.; Kochan, D.; Fabian, J. Spin-Orbit Coupling in Methyl Functionalized Graphene. *Phys. Rev. B* **2016**, *93*, 045423.
(64) Brey, L. Spin-Orbit Coupling in Graphene Induced by Adatoms with Outer-Shell p Orbitals. *Phys. Rev. B* **2015**, *92*, 235444.
(65) Frank, T.; Gmitra, M.; Fabian, J. Theory of Electronic and Spin-Orbit Proximity Effects in Graphene on Cu(111). *Phys. Rev. B* **2016**, *93*, 155142.
(66) Vaklinova, K.; Hoyer, A.; Burghard, M.; Kern, K. Current-Induced Spin Polarization in Topological Insulator–Graphene Heterostructures. *Nano Lett.* **2016**, *16*, 2595–2602.
(67) Avsar, A.; Yang, T.-Y.; Bae, S.; Balakrishnan, J.; Volmer, F.; Jaiswal, M.; Yi, Z.; Ali, S. R.; Güntherodt, G.; Hong, B. H.; *et al.* Toward Wafer Scale Fabrication of Graphene Based Spin Valve Devices. *Nano Lett.* **2011**, *11*, 2363–2368.
(68) Elliott, R. J. Spin-Orbit Coupling in Band Theory\char22{}Character Tables for Some "Double" Space Groups. *Phys. Rev.* **1954**, *96*, 280–287.
(69) D'Yakonov, M. I.; Perel', V. I. Spin Orientation of Electrons Associated with the Interband Absorption of Light in Semiconductors. *Sov. J. Exp. Theor. Phys.* **1971**, *33*, 1053.
(70) Kochan, D.; Gmitra, M.; Fabian, J. Spin Relaxation Mechanism in Graphene: Resonant Scattering by Magnetic Impurities. *Phys. Rev. Lett.* **2014**, *112*, 116602.
(71) Fabian, J.; Sarma, S. D. Spin Relaxation of Conduction Electrons. *J. Vac. Sci. Technol. B* **1999**, *17*, 1708–1715.
(72) Patibandla, S.; Atkinson, G. M.; Bandyopadhyay, S.; Tepper, G. C. Competing D'yakonov–Perel' and Elliott–Yafet Spin Relaxation in Germanium. *Phys. E Low-Dimens. Syst. Nanostructures* **2010**, *42*, 1721–1726.
(73) Han, W.; Kawakami, R. K.; Gmitra, M.; Fabian, J. Graphene Spintronics. *Nat. Nanotechnol.* **2014**, *9*, 794–807.
(74) Slichter, C. P. *Principles of Magnetic Resonance*; Springer Series in Solid-State Sciences; Springer Berlin Heidelberg: Berlin, Heidelberg, 1990; Vol. 1.
(75) Leyland, W. J. H.; Harley, R. T.; Henini, M.; Shields, A. J.; Farrer, I.; Ritchie, D. A. Oscillatory Dyakonov-Perel Spin Dynamics in Two-Dimensional Electron Gases. *Phys. Rev. B* **2007**, *76*, 195305.

(76) Dietl, T. Semiconductor Spintronics. In *Modern Aspects of Spin Physics*; Pötz, W.; Hohenester, U.; Fabian, J., Eds.; Lecture Notes in Physics; Springer Berlin Heidelberg, 2007; pp. 1–46.
(77) Roche, S.; Åkerman, J.; Beschoten, B.; Charlier, J.-C.; Chshiev, M.; Dash, S. P.; Dlubak, B.; Fabian, J.; Fert, A.; Guimarães, M.; *et al.* Graphene Spintronics: The European Flagship Perspective. *2D Mater.* **2015**, *2*, 030202.
(78) Zhang, L.; Todri-Sanial, A.; Kang, W.; Zhang, Y.; Torres, L.; Cheng, Y.; Zhao, W. Quantitative Evaluation of Reliability and Performance for STT-MRAM. In *2016 IEEE International Symposium on Circuits and Systems (ISCAS)*; 2016; pp. 1150–1153.
(79) Krause, S.; Wiesendanger, R. Spintronics: Skyrmionics Gets Hot. *Nat. Mater.* **2016**, *15*, 493–494.
(80) Wang, Y. Non-Volatile in-Memory Computing. Thesis, 2015.
(81) Zhang, P.; Ma, L.; Fan, F.; Zeng, Z.; Peng, C.; Loya, P. E.; Liu, Z.; Gong, Y.; Zhang, J.; Zhang, X.; *et al.* Fracture Toughness of Graphene. *Nat. Commun.* **2014**, *5*, 3782.
(82) Zhu, M.; Dennis, C. L.; McMichael, R. D. Temperature Dependence of Magnetization Drift Velocity and Current Polarization in ${\text{Ni}}_{80}{\text{Fe}}_{20}$ by Spin-Wave Doppler Measurements. *Phys. Rev. B* **2010**, *81*, 140407.
(83) van Son, P. C.; van Kempen, H.; Wyder, P. Boundary Resistance of the Ferromagnetic-Nonferromagnetic Metal Interface. *Phys. Rev. Lett.* **1987**, *58*, 2271–2273.
(84) Rashba, E. I. Theory of Electrical Spin Injection: Tunnel Contacts as a Solution of the Conductivity Mismatch Problem. *Phys. Rev. B* **2000**, *62*, R16267–R16270.
(85) Volmer, F.; Drögeler, M.; Maynicke, E.; von den Driesch, N.; Boschen, M. L.; Güntherodt, G.; Beschoten, B. Role of MgO Barriers for Spin and Charge Transport in Co/MgO/graphene Nonlocal Spin-Valve Devices. *Phys. Rev. B* **2013**, *88*, 161405.
(86) Johnson, M.; Silsbee, R. H. Interfacial Charge-Spin Coupling: Injection and Detection of Spin Magnetization in Metals. *Phys. Rev. Lett.* **1985**, *55*, 1790–1793.
(87) Hanle, W. Über magnetische Beeinflussung der Polarisation der Resonanzfluoreszenz. *Z. Für Phys. 30*, 93–105.
(88) Sosenko, E.; Wei, H.; Aji, V. Effect of Contacts on Spin Lifetime Measurements in Graphene. *Phys. Rev. B* **2014**, *89*.
(89) Mermin, N. D. Crystalline Order in Two Dimensions. *Phys. Rev.* **1968**, *176*, 250–254.
(90) Novoselov, K. S.; Geim, A. K.; Morozov, S. V.; Jiang, D.; Katsnelson, M. I.; Grigorieva, I. V.; Dubonos, S. V.; Firsov, A. A. Two-Dimensional Gas of Massless Dirac Fermions in Graphene. *Nature* **2005**, *438*, 197–200.
(91) Zhang, Y.; Tan, Y.-W.; Stormer, H. L.; Kim, P. Experimental Observation of the Quantum Hall Effect and Berry's Phase in Graphene. *Nature* **2005**, *438*, 201–204.
(92) Lazzeri, M.; Mauri, F. Nonadiabatic Kohn Anomaly in a Doped Graphene Monolayer. *Phys. Rev. Lett.* **2006**, *97*, 266407.

(93) Katsnelson, M. I.; Novoselov, K. S.; Geim, A. K. Chiral Tunnelling and the Klein Paradox in Graphene. *Nat. Phys.* **2006**, *2*, 620–625.
(94) Ferrari, A. C. Raman Spectroscopy of Graphene and Graphite: Disorder, Electron–phonon Coupling, Doping and Nonadiabatic Effects. *Solid State Commun.* **2007**, *143*, 47–57.
(95) Ferrari, A. C.; Basko, D. M. Raman Spectroscopy as a Versatile Tool for Studying the Properties of Graphene. *Nat. Nanotechnol.* **2013**, *8*, 235–246.
(96) Cançado, L. G.; Jorio, A.; Ferreira, E. H. M.; Stavale, F.; Achete, C. A.; Capaz, R. B.; Moutinho, M. V. O.; Lombardo, A.; Kulmala, T. S.; Ferrari, A. C. Quantifying Defects in Graphene via Raman Spectroscopy at Different Excitation Energies. *Nano Lett.* **2011**, *11*, 3190–3196.
(97) Malard, L. M.; Pimenta, M. A.; Dresselhaus, G.; Dresselhaus, M. S. Raman Spectroscopy in Graphene. *Phys. Rep.* **2009**, *473*, 51–87.
(98) Heller, E. J.; Yang, Y.; Kocia, L.; Chen, W.; Fang, S.; Borunda, M.; Kaxiras, E. Theory of Graphene Raman Spectroscopy. *ArXiv150701647 Cond-Mat* **2015**.
(99) Ravani, F.; Papagelis, K.; Dracopoulos, V.; Parthenios, J.; Dassios, K. G.; Siokou, A.; Galiotis, C. Graphene Production by Dissociation of Camphor Molecules on Nickel Substrate. *Thin Solid Films* **2013**, *527*, 31–37.
(100) Wu, Y. A.; Fan, Y.; Speller, S.; Creeth, G. L.; Sadowski, J. T.; He, K.; Robertson, A. W.; Allen, C. S.; Warner, J. H. Large Single Crystals of Graphene on Melted Copper Using Chemical Vapor Deposition. *ACS Nano* **2012**, *6*, 5010–5017.
(101) Shin, H.-A.-S.; Ryu, J.; Cho, S.-P.; Lee, E.-K.; Cho, S.; Lee, C.; Joo, Y.-C.; Hong, B. H. Highly Uniform Growth of Monolayer Graphene by Chemical Vapor Deposition on Cu–Ag Alloy Catalysts. *Phys. Chem. Chem. Phys.* **2014**, *16*, 3087.
(102) Ago, H.; Tanaka, I.; Orofeo, C. M.; Tsuji, M.; Ikeda, K. Patterned Growth of Graphene over Epitaxial Catalyst. *Small* **2010**, *6*, 1226–1233.
(103) Kidambi, P. R.; Bayer, B. C.; Blume, R.; Wang, Z.-J.; Baehtz, C.; Weatherup, R. S.; Willinger, M.-G.; Schloegl, R.; Hofmann, S. Observing Graphene Grow: Catalyst–Graphene Interactions during Scalable Graphene Growth on Polycrystalline Copper. *Nano Lett.* **2013**, *13*, 4769–4778.
(104) Ago, H.; Ogawa, Y.; Tsuji, M.; Mizuno, S.; Hibino, H. Catalytic Growth of Graphene: Toward Large-Area Single-Crystalline Graphene. *J. Phys. Chem. Lett.* **2012**, *3*, 2228–2236.
(105) Felser, C.; Fecher, G. H.; Balke, B. Spintronics: A Challenge for Materials Science and Solid-State Chemistry. *Angew. Chem. Int. Ed.* **2007**, *46*, 668–699.
(106) Hsu, A. L.; Koch, R. J.; Ong, M. T.; Fang, W.; Hofmann, M.; Kim, K. K.; Seyller, T.; Dresselhaus, M. S.; Reed, E. J.; Kong, J.; *et al.* Surface-Induced Hybridization between Graphene and Titanium. *ACS Nano* **2014**, *8*, 7704–7713.
(107) Duong, D. L.; Han, G. H.; Lee, S. M.; Gunes, F.; Kim, E. S.; Kim, S. T.; Kim, H.; Ta, Q. H.; So, K. P.; Yoon, S. J.; *et al.* Probing Graphene Grain Boundaries with Optical Microscopy. *Nature* **2012**, *490*, 235–239.
(108) Ferrari, A. C.; Robertson, J. Interpretation of Raman Spectra of Disordered and Amorphous Carbon. *Phys. Rev. B* **2000**, *61*, 14095–14107.

(109) Schwan, J.; Ulrich, S.; Batori, V.; Ehrhardt, H.; Silva, S. R. P. Raman Spectroscopy on Amorphous Carbon Films. *J. Appl. Phys.* **1996**, *80*, 440–447.
(110) Steffen, H. J.; Roux, C. D.; Marton, D.; Rabalais, J. W. Auger-Electron-Spectroscopy Analysis of Chemical States in Ion-Beam-Deposited Carbon Layers on Graphite. *Phys. Rev. B* **1991**, *44*, 3981–3990.
(111) Ismach, A.; Druzgalski, C.; Penwell, S.; Schwartzberg, A.; Zheng, M.; Javey, A.; Bokor, J.; Zhang, Y. Direct Chemical Vapor Deposition of Graphene on Dielectric Surfaces. *Nano Lett.* **2010**, *10*, 1542–1548.
(112) Bo, Z.; Yang, Y.; Chen, J.; Yu, K.; Yan, J.; Cen, K. Plasma-Enhanced Chemical Vapor Deposition Synthesis of Vertically Oriented Graphene Nanosheets. *Nanoscale* **2013**, *5*, 5180.
(113) Malesevic, A.; Vitchev, R.; Schouteden, K.; Volodin, A.; Zhang, L.; Tendeloo, G. V.; Vanhulsel, A.; Haesendonck, C. V. Synthesis of Few-Layer Graphene via Microwave Plasma-Enhanced Chemical Vapour Deposition. *Nanotechnology* **2008**, *19*, 305604.
(114) Graphene Growth - Oxford Instruments https://www.oxford-instruments.com/products/etching-deposition-and-growth/processes/growth-processes/graphene-growth (accessed Aug 23, 2016).
(115) Zhang, B.; Lee, W. H.; Piner, R.; Kholmanov, I.; Wu, Y.; Li, H.; Ji, H.; Ruoff, R. S. Low-Temperature Chemical Vapor Deposition Growth of Graphene from Toluene on Electropolished Copper Foils. *ACS Nano* **2012**, *6*, 2471–2476.
(116) You, Y.; Ni, Z.; Yu, T.; Shen, Z. Edge Chirality Determination of Graphene by Raman Spectroscopy. *Appl. Phys. Lett.* **2008**, *93*, 163112.
(117) Vlassiouk, I.; Regmi, M.; Fulvio, P.; Dai, S.; Datskos, P.; Eres, G.; Smirnov, S. Role of Hydrogen in Chemical Vapor Deposition Growth of Large Single-Crystal Graphene. *ACS Nano* **2011**, *5*, 6069–6076.
(118) Brandon, R.; Bradshaw, F. J. *THE MOBILITY OF THE SURFACE ATOMS OF COPPER AND SILVER EVAPORATED DEPOSITS*; 1966.
(119) Samsavar, A.; Hirschorn, E. S.; Miller, T.; Leibsle, F. M.; Eades, J. A.; Chiang, T.-C. High-Resolution Imaging of a Dislocation on Cu(111). *Phys. Rev. Lett.* **1990**, *65*, 1607–1610.
(120) Lee, J.; Kim, Y.; Shin, H.-J.; Lee, C.; Lee, D.; Lee, S.; Moon, C.-Y.; Lee, S. C.; Kim, S. J.; Ji, J. H.; *et al.* Crack-Release Transfer Method of Wafer-Scale Grown Graphene Onto Large-Area Substrates. *ACS Appl. Mater. Interfaces* **2014**, *6*, 12588–12593.
(121) Tao, L.; Lee, J.; Chou, H.; Holt, M.; Ruoff, R. S.; Akinwande, D. Synthesis of High Quality Monolayer Graphene at Reduced Temperature on Hydrogen-Enriched Evaporated Copper (111) Films. *ACS Nano* **2012**, *6*, 2319–2325.
(122) Rosa, C. J. L. de la; Sun, J.; Lindvall, N.; Cole, M. T.; Nam, Y.; Löffler, M.; Olsson, E.; Teo, K. B. K.; Yurgens, A. Frame Assisted H2O Electrolysis Induced H2 Bubbling Transfer of Large Area Graphene Grown by Chemical Vapor Deposition on Cu. *Appl. Phys. Lett.* **2013**, *102*, 022101.

(123) Rakheja, S.; Naeemi, A. Graphene Nanoribbon Spin Interconnects for Nonlocal Spin-Torque Circuits: Comparison of Performance and Energy Per Bit With CMOS Interconnects. *IEEE Trans. Electron Devices* **2012**, *59*, 51–59.
(124) Wang, Z.; Tang, C.; Sachs, R.; Barlas, Y.; Shi, J. Proximity-Induced Ferromagnetism in Graphene Revealed by the Anomalous Hall Effect. *Phys. Rev. Lett.* **2015**, *114*, 016603.
(125) Ingla-Aynés, J.; Meijerink, R.; van Wees, B. Eighty-Eight Percent Directional Guiding of Spin Current with 90 μm Relaxation Length in Bilayer Graphene Using Carrier Drift. *ACS Nano Letters* **2016**, *16*, 4825-4830.